LARGE EDDY SIMULATIONS OF HEMODYNAMICS IN AORTIC STENOSIS MODELS

A THESIS SUBMITTED TO
THE GRADUATE SCHOOL OF NATURAL AND APPLIED SCIENCES
OF
MIDDLE EAST TECHNICAL UNIVERSITY

BY

SINAN SAVAŞKAN

IN PARTIAL FULFILLMENT OF THE REQUIREMENTS
FOR
THE DEGREE OF MASTER OF SCIENCE
IN
MECHANICAL ENGINEERING

JUNE 2023

Approval of the thesis:

LARGE EDDY SIMULATIONS OF HEMODYNAMICS IN AORTIC STENOSIS MODELS

submitted by **SINAN SAVAŞKAN** in partial fulfillment of the requirements for the degree of **Master of Science in Mechanical Engineering Department, Middle East Technical University** by,

Prof. Dr. Halil Kalıpçılar
Dean, Graduate School of **Natural and Applied Sciences** _____

Prof. Dr. M.A. Sahir Arıkan
Head of Department, **Mechanical Engineering** _____

Prof. Dr. Cüneyt Sert
Supervisor, **Mechanical Engineering, METU** _____

Examining Committee Members:

Prof. Dr. Yiğit Yazıcıoğlu
Mechanical Engineering, METU _____

Prof. Dr. Cüneyt Sert
Mechanical Engineering, METU _____

Assist. Prof. Dr. Özgür Uğraş Baran
Mechanical Engineering, METU _____

Assist. Prof. Dr. Ali Karakuş
Mechanical Engineering, METU _____

Assist. Prof. Dr. Hüseyin Enes Salman
Mechanical Engineering, TOBB ETU _____

Date:

I hereby declare that all information in this document has been obtained and presented in accordance with academic rules and ethical conduct. I also declare that, as required by these rules and conduct, I have fully cited and referenced all material and results that are not original to this work.

Name, Surname: Sinan Savaşkan

Signature :

ABSTRACT

LARGE EDDY SIMULATIONS OF HEMODYNAMICS IN AORTIC STENOSIS MODELS

Savaşkan, Sinan
M.S., Department of Mechanical Engineering
Supervisor: Prof. Dr. Cüneyt Sert

June 2023, 124 pages

Aortic stenosis is a heart condition that refers to the incomplete opening of the aortic valve, resulting in decreased flow area and transition to turbulence in the post-stenotic flow field. This turbulent activity induces pressure fluctuations on the vessel walls that generate distinct sound waves, called murmurs. These sound waves are used in determining the severity of the stenosis in auscultation-based diagnosis methods. In this study, large eddy simulations (LES) are employed to investigate these murmurs emitted from the vessel walls and correlate them with the severity of the stenosis. Additionally, post-stenotic flow fields under steady and pulsating conditions using Newtonian and non-Newtonian blood models are investigated in detail and the suitability of large eddy simulations in computational fluid dynamics (CFD) analyses of aortic stenoses is verified by comparing the obtained results with a reference solution. The simulations utilize simplified aorta models with the rigid wall assumption and a mean inlet Reynolds number of 2000. The results indicate that LES is a suitable tool for hemodynamic analyses that can accurately capture the source location of murmurs and break frequencies of the sounds emitted from the stenosed vessels. Additionally, the level of turbulence, the intensity of the murmurs, and break frequency are found

to be positively correlated with stenosis severity.

Keywords: Computational Fluid Dynamics, Large Eddy Simulations, Aortic Stenosis, Hemodynamics, Turbulence induced acoustics

ÖZ

AORT KAPAK DARLIĞI MODELLERİNDE KAN AKIŞI DİNAMİKLERİNİN BÜYÜK GİRDAP SİMÜLASYONLARI İLE İNCELENMESİ

Savaşkan, Sinan
Yüksek Lisans, Makina Mühendisliği Bölümü
Tez Yöneticisi: Prof. Dr. Cüneyt Sert

Haziran 2023 , 124 sayfa

Aort stenozu, aort kapağının tam açılmaması sonucunda, akış alanının daralması ve stenoz sonrası akış alanında türbülansa geçişe yol açan bir kalp hastalığıdır. Oluşan bu türbülanslı akış damar çeperlerinde basınç dalgalanmalarına neden olarak belirgin ses dalgaları üretir. Oluşan bu seslere üfürüm adı verilir. Bu ses dalgaları, oskültasyon (steteskop ile dinleme) temelli teşhis yöntemlerinde daralmanın seviyesinin belirlenmesinde kullanılır. Bu çalışmada, damar çeperlerinden yayılan ses dalgalarını incelemek ve bunları stenozun seviyesi ile ilişkilendirmek için büyük girdap simülasyonları (BGS) kullanılmıştır. Ayrıca, Newtonian ve Newtonian olmayan kan modelleri kullanılarak durgun ve pulsatil (kalp atımlı) koşullarda stenoz sonrası akış alanları detaylı bir şekilde incelenmiş ve büyük girdap simülasyonlarının aort stenozu için yapılan hesaplamalı akışkanlar dinamiği (HAD) analizlerindeki uygunluğu, elde edilen sonuçlar referans bir çözümle karşılaştırılarak doğrulanmıştır. Simülasyonlar, rijit duvar varsayımıyla basitleştirilmiş aort modeli ve ortalama giriş Reynolds sayısı 2000 kullanılarak gerçekleştirilmiştir. Sonuçlar, BGS'nin üfürüm kaynağı konumunu

ve darlıkla ilişkili seslerin kesim frekanslarını doğru bir şekilde yakalayabilen bir araç olduğunu göstermektedir. Ek olarak, türbülans seviyesi, üfürüm yoğunluğu ve kesim frekansının darlık seviyesi ile pozitif bir ilişki içerisinde olduğu gösterilmiştir.

Anahtar Kelimeler: Hesaplamalı Akışkanlar Dinamiği, Büyük Girdap Simülasyonu, Aort stenozu, Kan Akışı Dinamiği, Türbülans kaynaklı akustik

To my family.

ACKNOWLEDGMENTS

I would like to express my deepest gratitude to my thesis advisor, Prof. Dr. Cüneyt Sert, for their invaluable guidance, unwavering support, and mentorship throughout the entire process of this research. I am privileged to have had the opportunity to work under Dr. Sert's guidance. I would also like to extend my appreciation to Prof. Dr. Yiğit Yazıcıoğlu for their support and guidance throughout my research.

Special thanks to The Scientific and Technological Research Council of Türkiye (TÜBITAK) for supporting me with the 2210-A National MSc/MA Scholarship Program throughout my studies. Furthermore, I am also grateful for the TÜBİTAK ULAKBİM High Performance and Grid Computing Center for the TRUBA HPC system. All the simulations I performed during my research would have taken 14 years if I did not have access to the TRUBA HPC system and used my personal computer.

I am grateful to Dr. Burcu Ramazanlı for the invaluable technical and mental support provided throughout my research. Their guidance and assistance have been instrumental in the successful completion of my work. I would also like to thank Atakan Aygün for their friendship and moral support. Additionally, I would specially like to thank Dr. Selene Pirola and Emily Manchester for providing me with significant technical data. I am also grateful to Ahmet Bozkurt, MD, for relentlessly answering my questions on medical topics and providing essential knowledge.

Lastly, I would like to express my sincere gratitude to my parents and my sister. They have provided me with the opportunity to undertake this research journey and it is through their unwavering efforts that I have reached this significant milestone. Despite the physical distance between us, I have always felt their moral support. Words cannot adequately express my appreciation for everything they have done.

TABLE OF CONTENTS

LIST OF TABLES

TABLES

LIST OF FIGURES

FIGURES

LIST OF SYMBOLS

ν	kinematic viscosity
μ	dynamic viscosity
α	Womersley number
Re	Reynolds number
Re_c	critical Reynolds number
St_s	Strouhal number for steady flow
St_p	Strouhal number for pulsatile flow
ρ	density
p	pressure
p_{ref}	reference pressure
$\boldsymbol{u}$	velocity vector
S_{ij}	strain rate tensor
τ_{ij}	subgrid scale stress tensor
ν_{SGS}	subgrid scale eddy viscosity
C_S	Smagorinski coefficient
k_{sgs}	subgrid scale kinetic energy
V_{in}	constant inlet velocity
V_{jet}	velocity at the stenosis
V_{mean}	mean inlet velocity
D	unstenosed diameter
D_{jet}	diameter of the stenosis
y^+	wall unit normalized wall distance
η	Kolmogorov length scale

ε	rate of dissipation of turbulence kinetic energy per unit mass
ω_x	vorticity on the frontal plane
ω_s	streamwise vorticity
p'	pressure fluctuations w.r.t. steady mean flow
p''	pressure fluctuations w.r.t. phase average of pulsating flow
E_p	spectrum of pressure fluctuations
f	frequency
T	period of a flow cycle
u'_{str}	streamwise velocity fluctuations

LIST OF ABBREVIATIONS

AS	Aortic Stenosis
CFD	Computational Fluid Dynamics
FVM	Finite Volume Method
LES	Large Eddy Simulation
WALE	Wall Adapting Local Eddy-viscosity
SGS	Subgrid Scale
DNS	Direct Numerical Simulation
RANS	Reynolds-averaged Navier-Stokes
SIMPLE	Semi-Implicit Method for Pressure-Linked Equations
PISO	Pressure-Implicit with Splitting of Operators
PIMPLE	Combination of PISO and SIMPLE Algorithms
FSI	Fluid-Structure Interaction
TKE	Turbulent Kinetic Energy
WSS	Wall Shear Stress
CFL	Courant-Friedrichs-Lewy
RMS	Root Mean Square
PIV	Particle Imaging Velocimetry
MRI	Magnetic Resonance Imaging
CT	Computerized Tomography
CVD	Cardiovascular Diseases
AVR	Aortic Valve Replacement
CTA	Computerized Tomography Angiography
CoA	Coarctation of the Aorta

CHAPTER 1

INTRODUCTION

1.1 The Human Aorta

In this section, the structure of the aorta and several aortic conditions including aortic stenosis are explained.

1.1.1 The Structure of the Aorta

The aorta is the largest and main arterial vessel in the human body that carries oxygen-rich blood from the heart to all parts of the body. It absorbs the impact of up to 3 billion heartbeats and carries about 200 million liters of blood in an average lifetime [1]. The aorta originates from the top left ventricle of the heart, makes a turn, and extends down to the abdomen as seen in Figure 1.1. At the base of the aorta, a semilunar valve with three leaflets is present, called the aortic valve. During the systole phase of the heartbeat (when the heart contracts), the pressure in the left ventricle increases, and when it exceeds the pressure in the aorta, the aortic valve opens and blood flows out of the left ventricle and is transferred to the rest of the body. After the systole phase, the diastole phase begins: the heart starts to relax, the pressure in the left ventricle decreases and the aortic valve closes to prevent backflow of blood into the left ventricle [2, 3].

Most anatomical sources investigate the aorta by dividing it into segments. The upper portion of the aorta is termed the thoracic aorta (above the diaphragm) and the lower portion is termed the abdominal aorta (below the diaphragm). The thoracic aorta is also divided into sections based on the direction of blood flow. The part where the

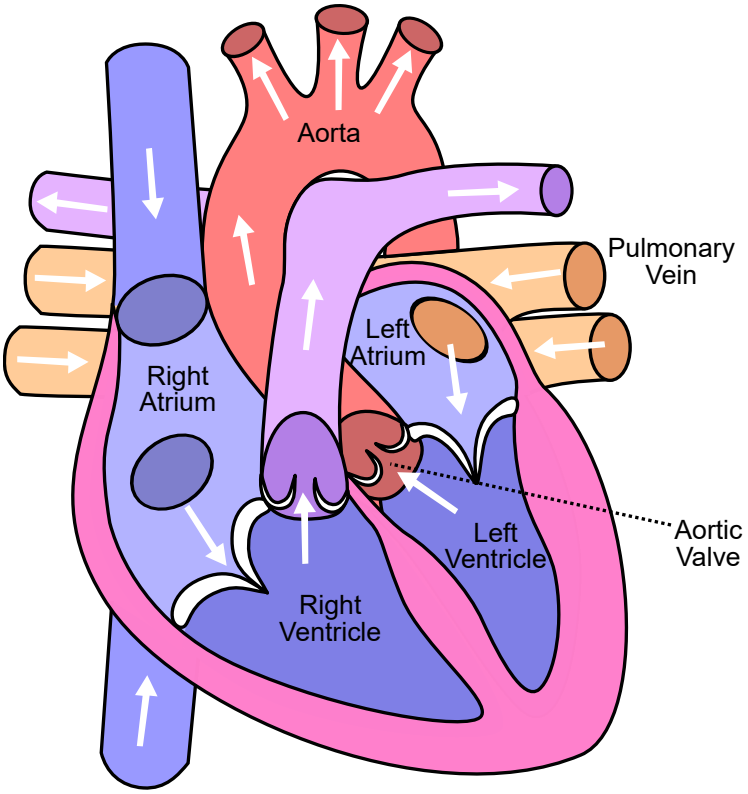

Figure 1.1: The human heart schematic. Adopted from [4].

blood flows superiorly from the heart is the ascending aorta, the turn is the aortic arch, and following the aortic arch where blood flows inferiorly is the descending aorta [5].

Figure 1.2 shows the main arteries and the segments of the thoracic aorta. The ascending aorta is the first fraction of the aorta, its length and diameter are approximately 5 cm and 3 cm, respectively [6]. Size and shape of the aorta vary from person to person, for example by age, sex, and weight [7]. The right and left coronary arteries originate from the base of the ascending aorta as shown in Figure 1.2, slightly above the aortic valve. These two arteries supply blood to the heart itself [8]. This region of the ascending aorta containing the right and left coronary arteries is called the aortic root [1].

The aortic arch is the portion of the aorta between the ascending and descending aorta. Three arteries branch off from the aortic arch: the brachiocephalic artery, the left common carotid artery, and the left subclavian artery. These arteries carry oxygenated

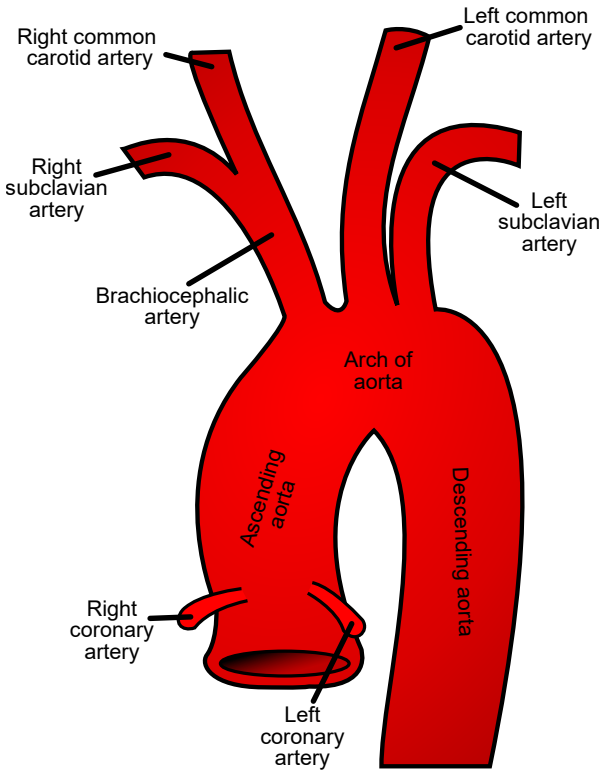

Figure 1.2: The thoracic aorta. Adopted from [9].

blood to the head, neck, shoulders, and upper limbs. The brachiocephalic artery branches to form the right subclavian and right common carotid arteries [2, 3]. The left and right common carotid arteries supply blood to the head and neck, and the left and right subclavian arteries supply blood to the arms.

The descending aorta is the continuation of the aortic arch. It is called the descending thoracic aorta before the diaphragm and the abdominal aorta after the diaphragm. The abdominal aorta supplies upper digestive tract organs, the diaphragm, small and large intestines, adrenal gland, kidneys, ovaries or testes, lower range intestine, posterior and lower abdominal wall, sacrum and coccyx, pelvic organs, and lower limbs through its branches[2, 3, 8].

1.1.2 Aortic Stenosis and Other Aortic Conditions

Patients may suffer from several aortic diseases, some examples are aortic stenosis, coarctation of the aorta, atherosclerosis, aortic aneurysm, aortic dissection, and aortic

regurgitation.

Aortic stenosis (AS) is the condition of narrowing of the exit of the left ventricle, resulting in decreased blood flow pumped from the heart so that the heart needs to work harder to pump enough blood to the body. A comparison of healthy and stenosed aortic valves is shown in Figure 1.3. It can be seen that the stenosed valve does not fully open as in the healthy case. Although the narrowing is mostly caused by the stenotic valve, it may also occur above or below the valve, called supravalvular stenosis and discrete subvalvular aortic stenosis, respectively [1, 10]. There are different types of valvular AS as shown in Figure 1.4. AS can be caused by a congenital bicuspid valve (a valve with two leaflets), calcification of a normal trileaflet valve, or rheumatic disease. The congenital valve abnormalities may be detected in early childhood where calcium buildup and rheumatic disease are usually apparent in midlife [1, 11].

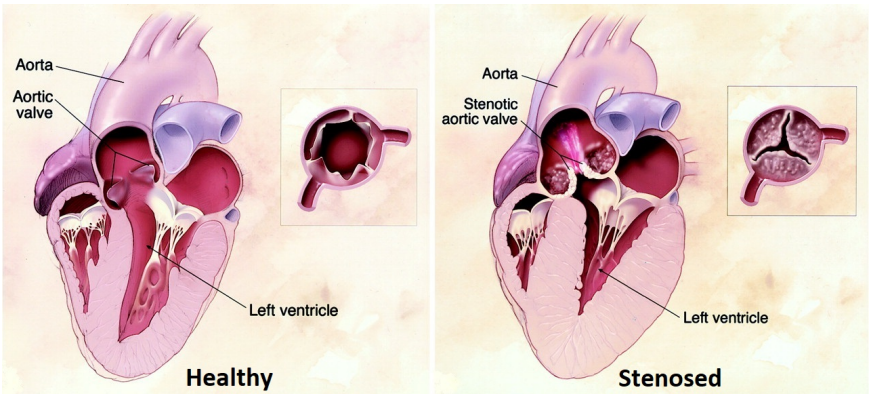

Figure 1.3: Aortic valve stenosis. Adopted from [11].

The degree of stenosis is classified as mild, moderate, or severe depending on the flow area. Severe stenosis corresponds to a vessel area reduced to 25% of its normal size [12]. The severity of the stenosis increases gradually over time. Most patients do not show symptoms until the stenosis becomes severe, but a significant stenosis can lead to shortness of breath (dyspnea), chest pain (angina), dizziness (near-syncope), and even sudden death [1, 11]. AS can also lead to secondary diseases such as ascending aorta dilatation, aneurysm, atherosclerosis, and left ventricular hypertrophy if not treated [13, 14].

There are several methods used for the diagnosis of aortic stenosis, such as auscultation, electrocardiography, echocardiography, angiography, chest x-ray, and cardiac

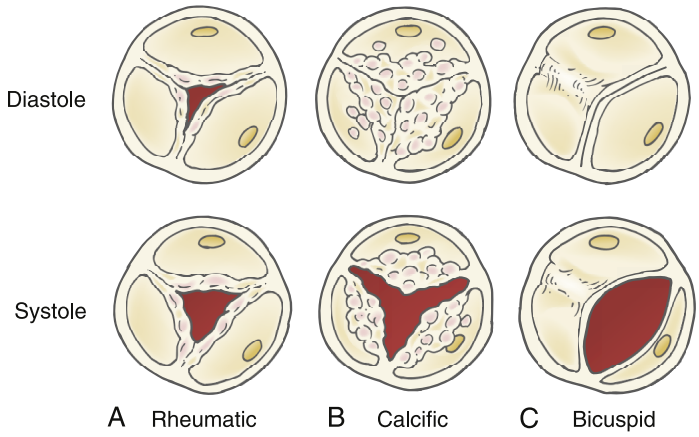

Figure 1.4: Types of aortic valve stenosis. Adopted from [15].

catheterization. Auscultation is simply listening to the internal sounds of the body by means of a stethoscope. Since abnormal flow patterns occurring in post-stenotic regions of arteries generate sounds called murmurs [16], auscultation can be useful for early diagnosis. Another method is electrocardiography, in which electrodes are placed on the skin and electrical activity of the heart is measured [17]. Electrocardiography is not a direct diagnosis method for AS since it is primarily used for left ventricular hypertrophy (thickening in the walls of the left ventricle), which is observed in approximately 85% of severe AS patients. Therefore, not all AS patients can be diagnosed with electrocardiography, but it is still an important tool for the diagnosis of AS [1]. Another approach is echocardiography, in which a medical image of the heart is obtained by using standard or Doppler ultrasound. It is one of the most effective ways to evaluate aortic valve anatomy and function non-invasively [18, 19]. Another medical imaging technique used for the diagnosis of AS is angiography, which involves a special dye (contrast agent) inserted into the blood. However, angiography is not advisable for patients with critical obstruction levels since injecting contrast agents into a high-pressure left ventricle is dangerous [1]. A chest x-ray can also be used for the examination of AS since it can show the degree of calcification of the aortic valve and left ventricle enlargement [20]. Among the diagnosis methods mentioned above, the most commonly preferred one is echocardiography since it is non-invasive. But if the evidence of the non-invasive methods is not enough or there is a discrepancy among them, the cardiac catheterization method is used. In cardiac catheterization,

pressure on both sides of the aortic valve is measured by inserting catheters inside the heart and/or the aorta, which makes it an invasive diagnosis method. The degree of stenosis is decided based on the pressure difference across the valve [20, 21].

When the aortic stenosis is not severe and patients do not show symptoms, the treatment is usually not necessary and regular check-ups are enough. However, patients with severe stenosis require treatment [20]. The treatment options can be aortic valve repair, aortic valve replacement, transcatheter aortic valve replacement, and balloon valvuloplasty. Aortic valve repair comprises all repairing operations performed on a diseased aortic valve and it is most commonly used for aortic regurgitation (leakage of blood through the aortic valve). This method is not very common for aortic stenosis [22]. The most common treatment for AS is aortic valve replacement by open-heart surgery. Two general types of artificial aortic valves are present: mechanical and tissue valves. Mechanical valves are made of metal and they last longer but they increase the risk of blood clot formation on the artificial valve surface [11]. Tissue valves are made of animal tissue (heterografts) and they can last up to 20 years [23]. The disadvantage of tissue valves is that they deteriorate more quickly in younger patients [24]. Surgical valve replacement operations can be too risky for some patients, such as people over 75 years old. For these patients, another valve replacement method, called the transcatheter aortic valve replacement (TAVR) is preferred [25, 26]. In TAVR, the replacement of the aortic valve is performed through the blood vessels, not by open-heart surgery. Another treatment option is balloon valvuloplasty. A balloon is attached to the dysfunctioning valve by means of a catheter, and it is inflated to open the stenotic valve. While this method is a good alternative for children and adolescents, it is not very effective for adults [1].

Narrowing of the aorta does not only occur at the aortic root as in AS. Localized contractions might be seen in any part of the aorta, and they are called the Coarctation of the Aorta (CoA). The word ‘coarctation’ means narrowing, contracted, or compressed. Coarctations are usually encountered in the aortic arch, and mostly near the region where ductus arteriosus (a blood vessel present in a fetus) attaches. Similar to aortic stenosis, CoA also blocks the normal flow to the body and causes increased afterload on the left ventricle, upper body hypertension, turbulent flow in the thoracic aorta, and decreased blood flow to the lower body [27]. CoA is also known to

generate heart murmurs that can be heard with auscultation.

Aortic stenosis and coarctation of the aorta are two conditions in which the aorta gets narrower and blood flow is restricted. Similar to these, another aortic narrowing mechanism is the thickening and hardening of the arterial walls, called arteriosclerosis. The most common and significant type of arteriosclerosis is atherosclerosis, which can be defined as the accumulation of fibrofatty plaques in the inner layer of the arteries as shown in Figure 1.5. These plaques may rupture and cause local thrombosis which then leads to occlusion of the artery [28]. The narrowing caused by the fibrofatty plaques produces audible murmurs as in AS.

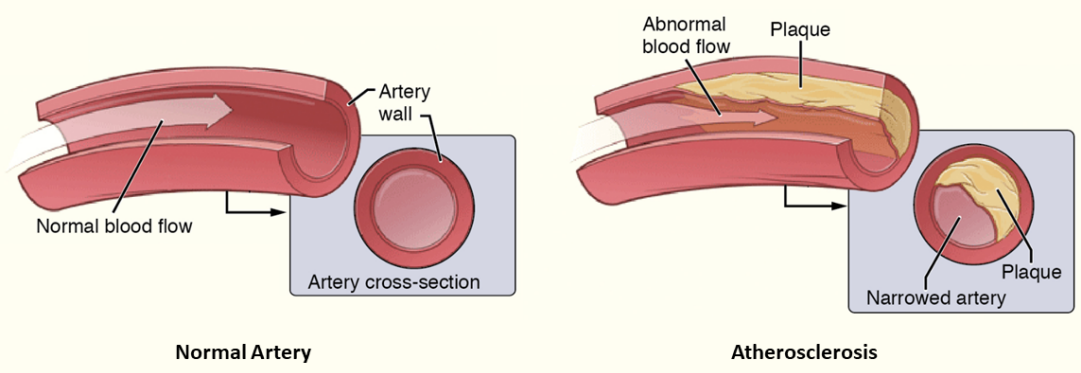

Figure 1.5: Atherosclerosis. Adopted from [29].

1.2 Computational Fluid Dynamics and Its Applications in the Healthcare Industry

Computational fluid dynamics (CFD) is a numerical tool to analyze the behavior of fluids, such as the airflow over the wings of an aircraft, wind over buildings, water flow in pipes, cooling fluids flowing over microchips, fuel injected to an engine, etc. by means of computer simulations. The extensive use of CFD allows it to be a significant tool in the healthcare industry as well, the working fluid being the blood flowing in our veins.

The process of CFD involves numerically solving the fundamental governing equations of fluid dynamics, which are the Navier - Stokes equations. In order to solve these equations, the time and space need to be discretized by dividing the problem

domain into finite sub-domains. There are several discretization methods such as the finite volume method (FVM), finite element method (FEM), finite difference method (FDM), spectral element method (SEM), and lattice Boltzmann method (LBM). The most popular discretization method among CFD solvers is the FVM, in which the problem domain is divided into finitely many control volumes, or usually called cells.

Fluid flows can usually be classified as laminar or turbulent flows. Laminar flow is when the fluid flows smoothly in layers and streamlines are mostly parallel. Turbulent flow is exactly the opposite, the flow is chaotic and streamlines are irregular. From a CFD point of view, turbulent flows are harder to analyze since a very wide range of time and length scales needs to be resolved. This is not always achievable due to the limits of computational resources, hence a method called turbulence modeling is used. In turbulence modeling, a mathematical model is constructed and additional equations are solved to predict the effects of turbulence. The most commonly used method in turbulence modeling is the Reynolds-averaged Navier–Stokes (RANS) equations. This method is based on the Reynolds decomposition [30], where an instantaneous flow quantity is separated into its time-averaged and fluctuating quantities, and simplified to give approximate solutions to the Navier-Stokes equations. The required computational resource for RANS is acceptable, hence it is widely used in the industry. However, the solutions are only approximations of the exact solution and have limitations due to modeling assumptions. Another approach is large eddy simulation (LES), where large scales of the flow are resolved and the small scales are modeled. This way, LES provides more accurate results compared to RANS but has greater computational cost. Combining RANS and LES is also possible, and is called detached eddy simulation (DES). DES is a modified RANS model which switches to LES in the regions where the computational grid is fine enough. Finally, the most elite option is to solve the Navier-Stokes equations numerically without using any turbulence model with a very fine mesh. This method is called direct numerical simulation (DNS), and it is the state-of-the-art CFD. All ranges of spatial and temporal scales of turbulence are resolved in DNS and the solution is closest to the exact solution. The downside of DNS is its high computational cost, which makes it almost impossible to be used in engineering applications. Indeed, DNS is mostly used in academia and research, and mostly for problems with low Reynolds numbers.

CFD applications in the healthcare industry are limited compared to other industries since the human anatomy and fluid behavior inside the body are extraordinarily complex. However, CFD has a major advantage in healthcare applications, which is its ability to provide information that cannot be directly measured by means of clinical visualization methods such as magnetic resonance imaging (MRI) or computerized tomography (CT). An example is wall shear stress (WSS), a critical parameter for understanding the progression of atherosclerosis (Morris 2016). Moreover, the information provided by CFD simulations is in great detail due to their high spatial resolution that cannot be achieved by conventional clinical methods like cardiac catheterization or MRI [31]. CFD is also used in patient specific virtual treatment planning: several simulations of operation alternatives are helping surgeons choose the best treatment method [32, 33, 34, 35].

The simulation results obtained by CFD provide information about flow patterns, pressure values, energy loss of the blood flow, normal and shear stress values on the vessel walls, oscillatory shear index, etc. [31]. Using these results, CFD is applied in cardiovascular medicine for several purposes: design and optimization of valve prostheses, non-invasive computation of trans-valvular pressure drop, providing hemodynamic data for virtual therapy predictions of aortic aneurysm and aortic dissection diseases, stent design, non-invasive diagnosis and controlling of response to treatment in pulmonary hypertension cases, design and optimization of medical pumps, hemodynamic analyses of congenital heart diseases, etc [36].

1.3 Literature Review

In this section, relevant studies from the literature are outlined.

1.3.1 Experimental Studies

The earlier work in the area of hemodynamics of the thoracic aorta date back to the 1970s and they are mostly experimental studies performed on in vitro models. Nerem et al. [37] studied the blood flow in a cast model of the thoracic aorta of a dog and Falsetti et al. [38] worked on dog aortas by collecting in vivo velocity data. Both

studies concluded that the velocity profiles are skew in the aortic arch and blunt in the descending aorta. Yearwood et al. [39] performed experiments using an in vitro aortic stenosis model and showed the effects of the stenosed valve on the flow field in the aortic arch.

Several experiments were performed on curved tubes to understand the flow physics in the thoracic aorta. Agrawal et al. [40] investigated the development of flow and Dean vortices in semicircular pipes and figured that the viscous region is confined in the vicinity of the walls and an inviscid region is present in the core region of the tube. Choi et al. [41] measured the local wall shear rates in the entrance region of a curved pipe and observed pairs of vortices in the entrance region, indicating Dean vortices. Chandran and Yearwood [42] used physiological pulsatile flow in their curved tube experiments and detected reverse flow during the diastole phase.

More recently, the development of particle imaging velocimetry (PIV) technology led to more realistic experiments. Saikrishnan et al. [43] performed experiments on bicuspid aortic valve models by using PIV and investigated the hemodynamics of the post-stenotic flow field. They found that the bicuspid aortic valve condition causes more stress in the walls of the aorta compared to calcific stenosis. Keshavarz et al. [44] used PIV to study the flow field in an aorta model with coarctation (CoA) and concluded that the presence of the coarctation introduces high turbulent kinetic energy compared to a healthy model. Barakat et al. [45] conducted experiments using in vitro aorta models with different transcatheter aortic valves. They investigated the transvalvular pressure gradients of different valves to test their performance for clinical use.

1.3.2 Numerical Studies on Healthy Aorta Models

There are several numerical studies in the literature that worked on healthy aorta models. Some of the main purposes of these studies are to investigate the blood flow dynamics numerically, validate numerical methods for clinical use, compare CFD methods, and investigate blood characteristics.

Tse et al. [46] investigated the effects of geometric changes due to aging on hemo-

dynamics in the thoracic aorta. 6 aged subjects are included in the study and they underwent computed tomography (CT). The reconstructed aorta models are then used in the patient-specific CFD analyses with realistic boundary conditions and laminar flow assumption. The results suggested that hemodynamics in the thoracic aorta is greatly affected by geometrical features. Another study on the model effects is [47], where Morris et al. compared the CT scan of a thoracic aorta model with its modified version by means of CFD. In the modified model, all cross-sections are assumed to be circular. Simulations were performed with a laminar model and the results showed variations in the flow field in the aortic arch for the whole cardiac cycle and in the descending aorta during systole, but the models produced similar results during systole in the descending aorta.

Several studies focused on validating CFD methods with medical measurements or experimental data. Yu and Liu [48] investigated the aortic hemodynamics of 25 subjects using computed tomography angiography (CTA) and CFD. They aimed to develop CFD-based noninvasive diagnosis methods and in doing so, compared medical measurements and CFD results. The simulations demonstrated the capability of CFD to be used in the diagnosis of congenital heart diseases. Casacuberta et al. [49] performed laminar CFD analyses using OpenFOAM and compared the results with 4D phase-contrast magnetic resonance imaging (PCMRI) measurements. Small differences were observed but the main flow patterns were similar for CFD and PCMRI. The wall shear stress (WSS) was also considered and higher values are observed in the simulations, but it should be noted that the spatial discretization in PCMRI is not as fine as in CFD, therefore the measured WSS values are not very reliable. Morbiducci et al. [50] used an experimental approach to validate CFD results by using 3D particle tracking velocimetry (PTV). The simulations showed perfect agreement with the experiment during systole and weaker agreement during diastole. It is concluded that CFD is a reliable method to study hemodynamics in the thoracic aorta.

Understanding blood flow dynamics by means of CFD plays an important role in computational hemodynamics. With this purpose, Lain et al. [51] analyzed a realistic thoracic aorta model to investigate flow patterns, pressure contours, and WSS distributions using transient conditions and laminar model. They reported detailed information on the hemodynamics of human thoracic aorta including the upper branches.

Zakaria et al. [52] also tried to understand the flow field inside the thoracic aorta and performed a CFD study on the CT scan of a 71-year-old subject. They used LES with k-equation eddy viscosity model in OpenFOAM. The results showed skew axial velocity profiles and helical flow throughout the thoracic aorta with less rotational flow in the descending aorta.

The shear-thinning nature of blood raises the question of whether the non-Newtonian effects should be included in the CFD studies. To seek an answer to this question, Vinoth et al. [53] analyzed the CT scan of a 36-year-old healthy subject's aorta with both Newtonian and non-Newtonian models. The two models produced similar flow fields overall, but the non-Newtonian model resulted in slightly higher WSS values. Jalali et al. [54] also studied the effects of different rheological models on a patient-specific thoracic aorta model. Nine non-Newtonian models are used in the analyses and compared with the Newtonian model. Similar to the work of Vinoth and co-workers [53], a relation between WSS and non-Newtonian models is observed. Among all models, the Carreau model produced the lowest WSS values. The Cross model clearly showed difference among all the non-Newtonian models and produced the closest results to the Newtonian model. The rheological effects were most evident in the brachiocephalic and carotid branches. Indeed, blood has non-Newtonian characteristics in smaller arteries since the shear stress on blood elements varies non-linearly with shear rate [55].

1.3.3 Numerical Studies on Aortic Stenosis

CFD studies on aortic stenosis models mainly aim to understand the flow dynamics in the presence of related aortic diseases and improve surgical treatments.

Manchester et al. [56] performed large eddy simulations to investigate the flow field and turbulence effects in the presence of an aortic valve stenosis using a patient-specific thoracic aorta model. They reported comprehensive results on kinetic energy, turbulence-induced wall shear stress, and energy loss due to turbulence. The results of the numerical study are compared and validated against 4D flow MRI. With a similar purpose, Youssefi et al. [57] performed CFD analyses on patient-specific thoracic aorta models of 45 subjects. Some of the subjects were volunteers with healthy aor-

tas, and others had aortic regurgitation, aortic stenosis, or bicuspid aortic valve. The study aimed to explore the valve morphology effect on flow characteristics, especially helicity, wall shear stress (WSS), and oscillatory shear index (OSI). They observed that the presence of aortic stenosis resulted in a high velocity jet and high WSS, the bicuspid aortic valve caused highly helical flow, and aortic regurgitation patients showed the closest results to the volunteer group. Dabagh et al. [58] studied another type of stenosis in the thoracic aorta, atherosclerosis. They investigated the effects of atherosclerotic plaque location and stenosis severity by introducing artificial occlusions to a healthy patient-specific thoracic aorta model. After performing laminar CFD simulations, they found that the stenosis at the left common carotid artery and the brachiocephalic artery causes the highest WSS values. Hellmeier and co-workers [33] had a more practical purpose in investigating flow fields in thoracic aorta models. They compared the hemodynamic outcomes of using biological and mechanical aortic valve prostheses by using CFD simulations. The results indicated that mechanical valves perform better in terms of flow straightening, reduced secondary flows, and less wall shear stress. It is also observed that the selection of the valve prosthesis type is highly patient dependent.

The work of Hellmeier et al. [33] showed the importance of patient-specific treatment planning, which is an emerging field in computational biomechanics. This personalized therapy approach is suitable for the aortic valve replacement (AVR) procedure since it is known that abnormal flow patterns can be observed in patients who had undergone AVR [59]. To show that CFD can be used to improve the post-AVR flow patterns, Kelm et al. [34] investigated ten patients who had undergone AVR operation. Using patients' pre-treatment MRI images, they performed the AVR process virtually and compared the CFD results with actual post-treatment MRI data. The results showed great agreement, thus it is concluded that CFD is a highly effective tool to predict hemodynamic outcomes and to decide on treatment alternatives. Following Kelm and co-workers' study [34], Nordmeyer et al. [32] worked on post-AVR models of thirty-four patients. They performed virtual optimizations on these models by changing the size and orientation of the valve prosthesis, together with ascending aorta diameters. Then, they performed CFD simulations on these optimized models and compared the results with the actual post-AVR data. The optimized models

showed less complex flow profiles, indicating that simulation-based treatment planning is a promising approach to offer patients the best possible treatment outcome. CFD-based treatment planning is not limited to AVR operations, this approach can also be useful for cardiovascular surgeries where statistical evidence is insufficient to predict post-operative hemodynamic conditions. An example is the study of Itatani et al. [35], where a patient with ascending aorta stenosis, bilateral coronary arterial aneurysm, and thickened left ventricular wall is investigated. Root placement with in situ Carrel patch coronary reconstruction and coronary artery graft bypass methods are compared and the former is selected based on pressure distribution and supplied blood flow rate. The surgery is performed as planned by CFD and no complications are observed. Similarly, Hu et al. [60] compared treatment alternatives of a patient with supravalvular aortic stenosis (SVAS). Virtual McGoon, Doty, and Brom repairs were compared by using velocity profiles, wall shear stresses, and energy loss obtained from the simulations. The Brom repair is selected to be the most suitable one.

Not all articles focus on the medical aspect of CFD simulations, some studies investigate the methodologies and theory using simplified models. Mittal et al. [16] performed direct numerical simulations (DNS) on a U-tube with constrictions of different severity near the inlet, representing aortic stenosis. The purpose of the study was to explore the effect of stenosis on heart murmurs and analyze the hemodynamics in the thoracic aorta. The source of the murmurs is found to be located near 60° along the U-turn of the tube. The details of this study are provided in Section 3. Jhun et al. [61] also studied the effect of stenosis severity on U-tube models by using large eddy simulations and compared the results with particle image velocimetry (PIV) experiments. Another study using a simplified model is the work of Mittal et al. [62], where they worked on acoustics in the thoracic aorta using a realistic aortic valve model and employed DNS and fluid-structure interaction (FSI) solutions together.

There is also a great focus on the coarctation of the aorta (CoA) in the literature. Numerical studies are performed on CoA to improve clinical treatment and diagnosis methods. Goubergrits et al. [63] tried to understand whether CFD could improve blood flow dynamics in the aorta in CoA patients. 13 subjects are examined before and after treatment, and MRI data is compared with CFD data obtained from virtual therapy simulations. The virtually treated models produced significantly lower pres-

sure drop and WSS values. Thus, they proved that CFD can also have potential in the treatment of CoA patients. Melka et al. [64] also performed a virtual therapy on the patient-specific model of a CoA patient, and compared the blood flow characteristics of the original model and the modified model. The pressure drop and maximum velocity are decreased, and flow rate in the descending aorta is increased in the modified case. Motamed et al. [65] worked on non-invasive methods for diagnosis of CoA and developed a framework that performs CFD analyses on clinical data. This framework is used for improving clinical outcomes and personalized therapy planning for CoA patients. Similarly, Lu et al. [66] also worked on non-invasive diagnosis of CoA and validated a CFD-based method that only requires multi-detector computed tomography angiography (MDCTA) images. The tests showed that this method provided an accuracy level greater than the accepted standards. Another novel method is introduced by Aslan et al. [67] in which the peak systolic pressure difference (PSPD) across the coarctation is determined by CFD using cardiac magnetic resonance (CMR) data and cuff pressure measured from the arm of the patient. The proposed method is tested on 5 patients and the results are compared with the traditional invasive methods. It is seen that the PSPD is accurately predicted by the CFD-based method.

1.3.4 Aortic Transition to Turbulence

Transition to turbulence in the thoracic aorta is an important issue for both medical concerns and numerical studies. One of the earliest studies on this topic dates back to 1972, when Nerem et al. [37] tried to obtain a critical Reynolds number experimentally using a dog aorta cast. They discovered that the Reynolds number is not solely enough to explain the disturbed waveforms, and suggested that the Womersley number could be used to describe flow disturbances. Their repeated experiments showed that a critical Reynolds number for unsteady flows in the thoracic aorta can be expressed as:

$$Re_c = C \cdot \alpha \tag{1.1}$$

where C is a constant ranging from 250 to 1000 depending on the approximate duration of systole, and α is the Womersley number. Lutz et al. [68] reformed the results

of Nerem and co-workers [37] by presenting a systematic analysis on the critical Reynolds number and showed that the Strouhal number is also needed. They derived an improved correlation for the critical Reynolds number as:

$$Re_c = 169 \cdot \alpha^{0.83} \cdot St^{-0.27} \tag{1.2}$$

where St is the Strouhal number. Using this correlation (Equation 1.2), Stalder et al. [69] performed an experiment involving phase-contrast MRI data of thirty healthy volunteers, and examined the flow instabilities in the thoracic aortas of the subjects. They observed that the Reynolds numbers exceeded the critical value in some of the volunteers depending on their sex, body weight, and cardiac output. The outcome of this study is that transition to turbulence can be observed in the thoracic aorta even for healthy people. Similarly, Casacuberta et al. [49] also reported transition to turbulence in healthy subjects.

Although transition to turbulence can be observed in healthy people, many numerical studies [46, 47, 49, 54, 58] use the laminar flow assumption since it is suggested by Equations 1.1 and 1.2 that the critical Reynolds number is higher for pulsating flows compared to steady flows. However, when an anomaly is present, it is not safe to use the laminar flow assumption since turbulence is reported in the thoracic aorta by several studies that involve aortic diseases, such as [32, 33, 56, 57, 70]. Transition to turbulence is not very easy to capture numerically, but LES methodology has been proven to generate accurate predictions in biological flows where transition occurs [71, 72, 73, 74].

1.3.5 Aortic Boundary Conditions for Numerical Studies

Boundary conditions play a key role in numerical studies for providing accurate results. The physiological nature of human vessels and blood flow are difficult to implement in the simulation environment fully realistically, therefore reasonable assumptions are made to simplify the models. In this section, boundary conditions and simplifications used in the literature are summarized for inlet, outlets, and vessel walls of thoracic aorta models.

For the inlet condition, either medically measured or simplified velocity profiles are implemented in the CFD models. Several articles use flat velocity profiles [47, 51, 58, 75, 76] since the use of plug velocity profiles is supported by various in vivo measurements [38, 77, 78]. Although simplified velocity profiles are useful, recent studies showed that clinically measured patient-specific velocity profiles provide higher accuracy. Morbiducci et al. [79] analyzed the differences in using idealized and measured velocity profiles on a healthy patient-specific thoracic aorta model. They figured that plug velocity profiles can create misleading results and it is required to use patient-specific velocity profiles if such data is available. Another outcome of this study was that using only the axial component of the measured velocity data is enough to capture flow characteristics with sufficient accuracy. This outcome is supported by the fact that healthy subjects tend to have symmetric valvular velocity profiles and axial components dominate the flow. Goubergrits et al. [80] also compared plug vs MRI-based velocity profiles using the thoracic aorta models of three CoA patients. They found that using a plug velocity profile cannot generate proper peak systolic pressure gradient and wall shear stresses (WSS) results. Similarly, Pirola et al. [81] studied the effect of using flat, MRI-derived through plane (1D), and MRI-derived 3D velocity profiles using a model with severe aortic valve stenosis. They concluded that the best practice is to use the 3D velocity profiles and flat velocity profile does not provide accurate results. Youssefi et al. [82] performed a comprehensive study and investigated 2 subjects: a healthy volunteer and a patient with bicuspid aortic valve and dilated ascending aorta. They used plug, parabolic, and patient-specific inlet velocity profiles for both subjects and compared the results. It is concluded that using a parabolic velocity profile leads to more accurate results compared to the plug profile, and parabolic profiles can be useful in the absence of patient-specific data.

There are several alternatives to be used for outlet boundary conditions. A simple constant pressure condition can be specified, flow rates at the outlets can be imposed, the clinically measured data can be prescribed if available, or models such as lumped parameter Model (LPM) or the Windkessel model [83] can be used. These models represent the downstream domain analytically by using resistance, impedance, and compliance concepts. The Windkessel model is widely used in the literature [56, 64, 67, 84] when patient-specific data is available since the model requires clinically

obtained data of patients. Using LPM is a very similar method to the Windkessel model and is also used in patient-specific analyses [48, 65, 66]. It is also possible to impose the clinically measured pressure waveforms [46, 57, 85] or the flowrates [32, 33, 34] at the outlets. When patient data is not available, the most commonly used boundary conditions are applying constant pressure or zero-gradient pressure to the outlet patches. Constant pressure outlet boundary condition is reported to produce less accurate results compared to patient-specific conditions or the LPM [86, 87, 88], but this condition is used in several studies [61, 70, 89] and proved to be useful. The most commonly used outlet boundary condition in the absence of patient-specific data is the zero-gradient pressure condition [50, 54, 58, 60, 63]. A stress-free condition is applied at the outlet and the flow is assumed to be fully developed.

Human blood vessels are elastic up to a certain degree naturally. Whether this deflection can be ignored is a widely discussed issue. Most of the studies in the area of computational biofluid dynamics use a rigid wall assumption due to various reasons: Firstly, a fluid-structure interaction (FSI) study needs to be performed to take the deformations into account and this is a quite challenging task. Secondly, the main focus of the study is not affected by the rigid wall assumption. Lastly, the characteristics of wall elasticity are not well defined and highly subject-dependent, therefore more assumptions are added to the problem physics [47].

The elasticity of vessel walls was a question of interest even in the 1970s. Lighthill [90] reported that typical diameter changes in arteries are only about 2%. Singh et al. [91] performed experiments and found around 10% change in the diameter of an aorta during a cardiac cycle. Similarly, Rieu et al. [92] carried out an experiment using an elastic model of the human arterial tree and the obtained velocity profiles were comparable with rigid models. More recently, Giddens et al. [93] performed CFD studies on a healthy patient-specific thoracic aorta model including the wall compliance effects and compared the results with MRI measurements. They reported an interesting conclusion that the rigid models are in agreement with the elastic models, however, both of these simulations deviated from the MRI measurements and it was found that the flow is also affected by the movement of the aorta during the cardiac cycle. It should be noted that this movement effect is highly patient-dependent. Lantz et al. [94] also worked on healthy elastic models and reported that FSI analyses are

needed to investigate instantaneous wall shear stresses. On the contrary, Brown et al. [84] performed CFD analyses with deformable walls and showed that rigid models can capture important flow features in clinical applications.

An important fact to notice is the vascular stiffening with age and cardiovascular diseases including aortic stenosis [95, 96]. This hardening phenomenon of the aorta makes the rigid wall assumption more reasonable. Considering all the factors described above, simplifying the models with rigid walls is a commonly accepted assumption in computational hemodynamics [97].

1.3.6 Acoustical Studies

The concept of acoustics comes into play in stenosed vessels due to the sounds induced by turbulent blood flow. It is of great interest to relate these sound waves with the stenosis characteristics and improve non-invasive diagnosis methods by acoustic detection of coronary turbulence. An early experimental study on turbulence-induced acoustics in stenosed blood vessels is performed by Miller et al. [98]. They applied blunt stenoses to 10 dog aortas and obtained a linear relationship between flow through the stenosis and break frequency of the bruit. More recently, Mittal et al. [99] studied the generation and propagation of murmurs in the thoracic aorta using a simplified thorax model, with a coupled hemoacoustic simulation. They found that the source location does not depend on the severity of the stenosis. In a further study, Mittal et al. [62] investigated the acoustics in the thoracic aorta with the presence of valve abnormalities using direct numerical simulations (DNS) and fluid-structure interaction (FSI). To focus on the valve, they used the computational domain as a vertical straight tube representing the ascending aorta. The aortic valve model is used to represent both healthy and stenotic cases by changing the stiffness of the leaflets. The results of the study are used to correlate hemodynamic behavior and acoustic response so that "acoustic signatures" of healthy and stenotic valves are obtained. These acoustic signatures are then used to train machine learning algorithms for auscultation-based diagnosis methods.

Not all acoustic studies involve the aorta, many of them focus on other coronary arteries. Lees and Dewey [100] worked on non-invasive diagnosis of stenosis and de-

veloped the phonoangiography method. They also defined an analytical relation between the stenosis severity and the sound produced. The phonoangiography method is clinically tested by Kistler et al. [101]. The study involved 27 carotid bruits of 25 patients. The severities of the stenoses are correctly predicted in 92% of the cases by the phonoangiography method. Jones and Fronek [102] conducted experiments to improve the phonoangiography method and they obtained an empirical relationship between Strouhal number, Reynolds number and stenosis severity.

In addition to the clinical studies, several experiments are made for research purposes. Borisyuk [103, 104, 105] investigated the wall pressure fluctuations and the sound emerged from the stenosed artery. They found that the shape of the spectrum of wall pressure fluctuations is independent of stenosis severity and Reynolds number, whereas the level of the spectrum is dependent on stenosis severity and Reynolds number. Yazıcıoğlu et al. [106] also conducted experiments with stenosed tubes to investigate the wall elasticity effects on acoustic pressure intensities. They found very similar results with the rigid and compliant tubes.

Several numerical studies on stenosed coronary arteries are performed recently. Seo and Mittal [107] studied the effects of stenosis severity on acoustic radiation using 2D vessel models and observed that acoustic pressure fluctuation amplitude rises dramatically for stenosis severity of 75% and above. Özden et al. [108, 109, 110] performed LES in stenosed tubes of different severity and eccentricity. They showed that wall pressure fluctuations and resulting sound emission increase with stenosis eccentricity.

1.3.7 Recent Technologies on Medical Auscultation Devices

The research on acoustic detection of coronary turbulence led to some technological developments in the non-invasive diagnosis of stenosed arteries in recent years. Devices using microphone sensors are developed since the turbulence-induced acoustic pressure in stenosed coronary arteries can be difficult to hear by conventional auscultation methods. Makaryus et al. [111] tested the accuracy of one of these diagnosis devices, the cardiac sonospectrographic analyzer (CSA). They found the sensitivity of CSA to be 89.5% for stenosis severity of larger than 50%. The accuracy drops rapidly for less severe stenoses.

Two commercial products are the CADence and CADScore systems. These devices use acoustic detection principles to predict the level of stenosis in coronary arteries and involve a microphone sensor, ambient noise management, and data filtering systems. The CADence system is tested by Azimpour et al. [112] with a study involving 123 subjects with 52% having severe stenosis. The results showed that 70% of the subjects were diagnosed correctly. The other similar product, CADScore, is tested by Winther et al. [113] with a study involving 255 subjects with 63 patients having obstructive coronary artery diseases. 72% of the subjects were diagnosed correctly using the CADScore device.

1.4 Motivation and Outline

Millions of people suffer from cardiovascular diseases (CVD) such as coronary heart disease, cerebrovascular disease, peripheral arterial disease, heart attack, and stroke. The mortality of these conditions is so high that the deaths caused by these diseases are expected to be around 23.6 million by the year 2030 [114]. One major cause of CVD is aortic stenosis, which can lead to death if not treated [10]. Early diagnosis is crucial to prevent possible deaths, but traditional invasive diagnosis methods are costly, require open surgery, and are sometimes not applicable to all patients as mentioned in Section 1.1.2. Acoustic-based non-invasive diagnosis methods, however, do not have the risks of open surgery and can easily be applied to most patients. These acoustic technologies are promising but they lack clinical efficacy data, therefore they need further studies to correlate sound waves with the characteristics of the stenosis. This study firstly aims to investigate turbulence-induced acoustic emissions due to aortic stenosis and help develop acoustic-based non-invasive diagnosis devices by supplying training data. Another motivation is to analyze the flow field downstream of an aortic stenosis by means of LES and explain the results elaborately.

This thesis consists of 5 chapters. The first chapter includes an introduction to aortic stenosis and literature review in the field of aortic hemodynamics. In Chapter 2, the CFD methodology used in the solutions and data presentation methods are explained. Chapter 3 represents a verification study where a previously solved problem is solved again and the results are compared with a reference solution. After the methodology

is verified, the effects of stenosis severity are investigated under pulsatile flow conditions in Chapter 4. Finally, in Chapter 5, the results of the study are summarized, limitations are discussed and future work is suggested.

CHAPTER 2

NUMERICAL METHODS

2.1 Governing Equations

The process of CFD involves numerically solving the fundamental governing equations of fluid dynamics, which are the Navier - Stokes equations, or the conservation of mass and momentum equations. These equations for incompressible and isothermal flow of a Newtonian fluid are expressed as:

$$\nabla \cdot \boldsymbol{u} = 0 \tag{2.1}$$

$$\rho \frac{\partial \boldsymbol{u}}{\partial t} + \rho(\boldsymbol{u} \cdot \nabla)\boldsymbol{u} = -\nabla p + \mu \nabla^2 \boldsymbol{u} \tag{2.2}$$

Equation 2.1, the conservation of mass equation, is also called the continuity equation, and it accounts for the mass balance. The momentum equation (Equation 2.2) is actually Newton's 2nd law applied on a moving fluid particle, defining the force balance. Equations 2.1 and 2.2 construct a system with 4 scalar unknowns: p and the three components of the velocity vector $\boldsymbol{u}$, and 4 scalar equations: continuity equation and the three components of the momentum equation.

2.2 Modeling of Blood Flow in the Thoracic Aorta

The human thoracic aorta is a complex geometry: featuring curvatures in all three dimensions (out-of-plane curvatures), three vessels branch off from the aortic arch as shown in Figure 1.2, and it tapers towards the descending aorta with a decrease in

cross-sectional area of about 35% [115]. The aortic arch introduces curvature effects as in the flow in a curved tube and secondary flow effects are observed. Moreover, the blood enters the thoracic aorta through the aortic valve with certain whirling [81], increasing the secondary flow effects. The pulsating nature of blood flow and elastic vessel walls also add complexities to the problem physics.

Blood is a complex biological fluid that has a non-Newtonian nature, meaning that its viscosity varies with shear rate. More specifically, the viscosity of blood decreases under shear strain, which is called a shear-thinning behavior. The prevailing rheological property of blood in large arterial vessels (diameter > 1 cm) is its shear-rate-dependent viscosity [116]. To account for the non-Newtonian effects, additional models such as Casson [117], K-L [118], Carreau [119], Carreau-Yasuda [120], Cross [121], and Power-law [118] models are used. These models use shear-thinning physics and are the most popular non-Newtonian models for blood flow simulations [54]. In Chapter 4, the Carreau model is used, which models the blood viscosity as [119]:

$$\mu(\dot{\gamma}) = \mu_\infty + (\mu_0 - \mu_\infty)\left[1 + (\lambda\dot{\gamma})^2\right]^{(n-1)/2} \tag{2.3}$$

where μ is the actual dynamic viscosity of blood and μ_∞ is the Newtonian blood viscosity. $\dot{\gamma}$ is the strain rate given in s^{-1}, and $\mu_0 = 0.056$ Pa s, $\lambda = 3.313005$, $n = 0.3568$ are constants.

Human blood is composed of several components, mostly containing red blood cells, white blood cells, platelets, and the plasma. The ratio of the volume of the blood cells to the whole blood volume is termed as hematocrit [122], which is known to be 40% for normal human blood [123]. The effects of the particle structure of blood is neglected in the simulations in this study and hematocrit value is taken to be 0%.

Transition to turbulence is another issue in simulating the blood flow inside human aorta. This phenomenon is highly subject-specific, some people might have laminar flow in their aorta and others have instabilities and transition to turbulence. Gender, age, weight, cardiac output, etc. highly influence the flow characteristics in the thoracic aorta [69]. In the case of aortic diseases, most patients have turbulent flow due to disturbed vessel geometry, especially the patients with aortic stenosis, atheroscle-

rosis, and coarctation of the aorta.

2.3 Large Eddy Simulation

Large eddy simulation is a CFD technique where large scale motions of turbulence are directly solved and small scale motions are modeled with a subgrid scale model. LES was first proposed in 1963 by Smagorinski [124] to simulate atmospheric flows. Until the mid 1980s, it had simple applications such as homogeneous turbulence or plane channel flows. In the 1990s, LES usage significantly increased due to the developments in computing power and it became a promising technique for simulating turbulent flows. Currently, for low Reynolds number applications, LES is the most feasible CFD method to capture realistic turbulent and transitional flow behaviour since it is far more accurate than RANS and is computationally affordable for complex flows unlike DNS [125].

The governing equations of LES are the Navier-Stokes equations. A low-pass spatial filter is applied to the instantaneous Navier - Stokes equations to distinguish the large (resolved) and small (sub-grid scale) eddies. The filtering operation results in the unsteady governing equations for large scale motions. This method is called explicit filtering [125].

Let $f(x_i, t)$ be a generic function, and $\bar{f}(x_i, t)$ be its filtered (resolvable) component, also called the convolution of $f(x_i, t)$. $f(x_i, t)$ and $\bar{f}(x_i, t)$ are related to each other with a filter function G as [126]:

$$\bar{f}(x_i, t) = \int f(x_i', t)\, G\left(x_i - x_i',\ \Delta(x_i)\right)\, dx_i' \tag{2.4}$$

The above integration is over the flow volume. The filter function G can be of different types, the most common ones are the top-hat (box), Gaussian, and sharp spectral filters. $\Delta(x_i)$ is the filter width, which defines how large the resolved eddies are. The filter width can be selected as a multiple of the grid size [127]. In practice, it is usually taken as:

$$\Delta(x_i) = \sqrt[3]{\Delta x\, \Delta y\, \Delta z} \tag{2.5}$$

Figure 2.1 shows an illustration of the filtering process. The red curve denotes the unsteady flow field $(f(x_i, t))$. The filtering operation performed to this red curve results in the filter scale (fs), or the resolved scale $(\bar{f}(x_i, t))$, shown by the blue curve. The green curve shows the difference between the total and filtered fields, i.e. the subfilter-scale (sfs), or the sub-grid scale (SGS) components. In LES, the filtered field (blue curve) is directly solved and the SGS field (green curve) is modeled to approximate the actual flow field (red curve). It should be noted that the magnitude of the modeled SGS component is oscillating around zero, therefore it has smaller magnitude and higher frequency compared to the filtered component [128].

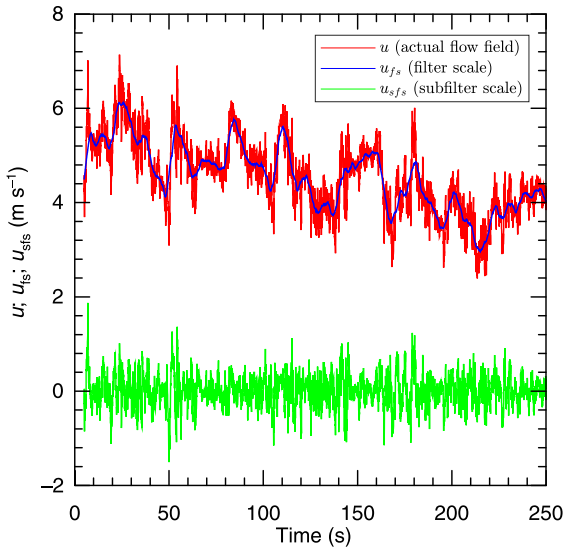

Figure 2.1: LES filtering decomposition procedure. Adopted from [128].

When LES is used together with the finite volume method, governing equations are integrated over control volumes, which is equivalent to the top-hat filter, therefore there is no need to filter the governing equations explicitly. This method is called implicit filtering [125]. The filtered Navier - Stokes equations for a Newtonian incompressible flow can be written as:

$$\partial_i \bar{u}_i = 0 \tag{2.6}$$

$$\partial_t(\rho \bar{u}_i) + \partial_j(\rho \bar{u}_i \bar{u}_j) = -\partial_i \bar{p} + 2\partial_j(\mu \bar{S}_{ij}) - \partial_j(\tau_{ij}) \tag{2.7}$$

$$\overline{S}_{ij} = \frac{1}{2}(\partial_i \overline{u}_j + \partial_j \overline{u}_i) \tag{2.8}$$

$$\tau_{ij} = \rho(\overline{u_i u_j} - \bar{u}_i \bar{u}_j) \tag{2.9}$$

where ρ is the constant density, $\bar{u}_i$ is the filtered velocity, $\bar{p}$ is filtered pressure, μ is the dynamic viscosity, $\bar{S}_{ij}$ is the filtered strain rate tensor, and τ_{ij} is the unknown SGS stress tensor.

The SGS stress tensor represents the effects of the unresolved small scale motions and it is unknown, therefore it needs to be modelled so that the governing equations can be solved. The modelling is performed by means of an SGS model. There are many different SGS models, but the fundamental one is the Smagorinsky model [124], which is also referred to as the Smagorinsky–Lilly model. The model makes use of the eddy-viscosity assumption, or the Bousinesq's hypothesis, which relates the unknown SGS stress tensor τ_{ij} to the strain rate tensor $\bar{S}_{ij}$ as [129, 130]:

$$\tau_{ij} - \frac{1}{3}\delta_{ij}\tau_{kk} = -2\nu_{sgs}\bar{S}_{ij} \tag{2.10}$$

where δ_{ij} is the Kronecker-Delta function and ν_{sgs} is called the SGS eddy viscosity, which is calculated as:

$$\nu_{sgs} = (C_s\Delta)^2|\bar{S}| \tag{2.11}$$

where C_s is the flow dependent Smagorinski coefficient. A C_s value of 0.18 is reasonable for isotropic turbulence and it needs to be reduced to 0.1 near the wall boundaries [125]. The need for C_s to change throughout the domain makes it impractical. The model is also known to be too dissipative and produces errors, especially for transitional flows. To improve this model, Germano et al [131] proposed a dynamic SGS model, where C_s is computed locally during the simulation, as a function of time and space. Further information about different SGS models can be found in [132, 133, 134].

A promising SGS model is the Wall Adapting Local Eddy-viscosity (WALE) model.

The model is developed for LES in complex geometries and both the strain and the rotation rate of the smallest resolved turbulent fluctuations are taken into account. Therefore, all turbulent motion relevant to the dissipation of kinetic energy is captured. A dynamic near-wall scaling or damping is also not required for wall bounded flows since the eddy-viscosity naturally goes to zero near solid boundaries. Furthermore, the WALE model produces zero eddy viscosity for pure shear and it is able to handle transition to turbulence [135].

In the WALE model, the SGS stress tensor is defined as:

$$\tau_{ij} = \frac{2}{3} k_{sgs} \delta_{ij} - 2\nu_{sgs} \bar{S}_{ij} \tag{2.12}$$

where k_{sgs} is the subgrid scale kinetic energy and is defined as:

$$k_{sgs} = \frac{1}{2}(\overline{u_k u_k} - \bar{u}_k \bar{u}_k) \tag{2.13}$$

Finally, the SGS eddy viscosity is calculated as:

$$\nu_{sgs} = (C_w \Delta)^2 \frac{(S_{ij}^d S_{ij}^d)^{3/2}}{(\overline{S_{ij}}\ \overline{S_{ij}})^{5/2} + (S_{ij}^d S_{ij}^d)^{5/4}} \tag{2.14}$$

where S_{ij}^d is the traceless symmetric part of the square of the velocity gradient tensor and C_w is a model coefficient depending on the Smagorinski model constant (C_k) and S_{ij}^d [135].

The WALE model is widely used for hemodynamic simulations [56, 74, 136, 137, 138] and is also preferred in this study due to its advantages.

2.4 OpenFOAM and pimpleFoam Solver

OpenFOAM (Open-source Field Operation and Manipulation) is a C++ library used to develop numerical solvers, mostly CFD solvers. OpenFOAM is being released as a free open-source software with many built-in CFD solvers that use finite volume method (FVM). It has three pressure-velocity coupling algorithms to solve the gov-

erning partial differential equations. These solvers are PISO (Pressure-Implicit with Splitting of Operators), SIMPLE (Semi-Implicit Method for Pressure-Linked Equations) and PIMPLE (combined PISO & SIMPLE).

The solver of the PIMPLE algorithm is called "pimpleFoam" in OpenFOAM. The working schematic of the pimpleFoam algorithm is given in Figure 2.2. In this algorithm, a new time step starts by increasing the current simulation time by the time step defined by the user or calculated based on a specified Courant number. Then the pressure-velocity coupling loop runs, inside which a momentum predictor step is performed by solving the momentum equation, followed the corrector loop. The corrector loop involves pressure and momentum corrector steps. Inside the pressure corrector step, the Poisson equation for pressure (obtained by combining the divergence of the momentum equation and the continuity equation) is solved. Then, inside the momentum corrector step, the velocity field is updated based on the corrected pressure. If the pressure-velocity coupling loop is executed only once, then the algorithm behaves like the PISO algorithm, and if the corrector loop is also executed only once, then the algorithm behaves like the SIMPLE algorithm.

In this study, the pimpleFoam algorithm is used with 2 pressure-velocity coupling loops and 3 corrector loops.

2.5 Data Presentation

In all of the simulations, there are several monitor points on the domain that record data in time. These data are usually presented in average, fluctuating, or root mean square (RMS) form.

For a general flow variable f, the mean over the averaging time T is calculated as:

$$\bar{f}(x,y,z) = \frac{1}{T}\int_{t_0}^{t_0+T} f(x,y,z,t)\,dt \tag{2.15}$$

where t_0 denotes the instant that the averaging starts. The fluctuating component of f is defined as:

$$f'(x,y,z,t) = f(x,y,z,t) - \bar{f}(x,y,z) \tag{2.16}$$

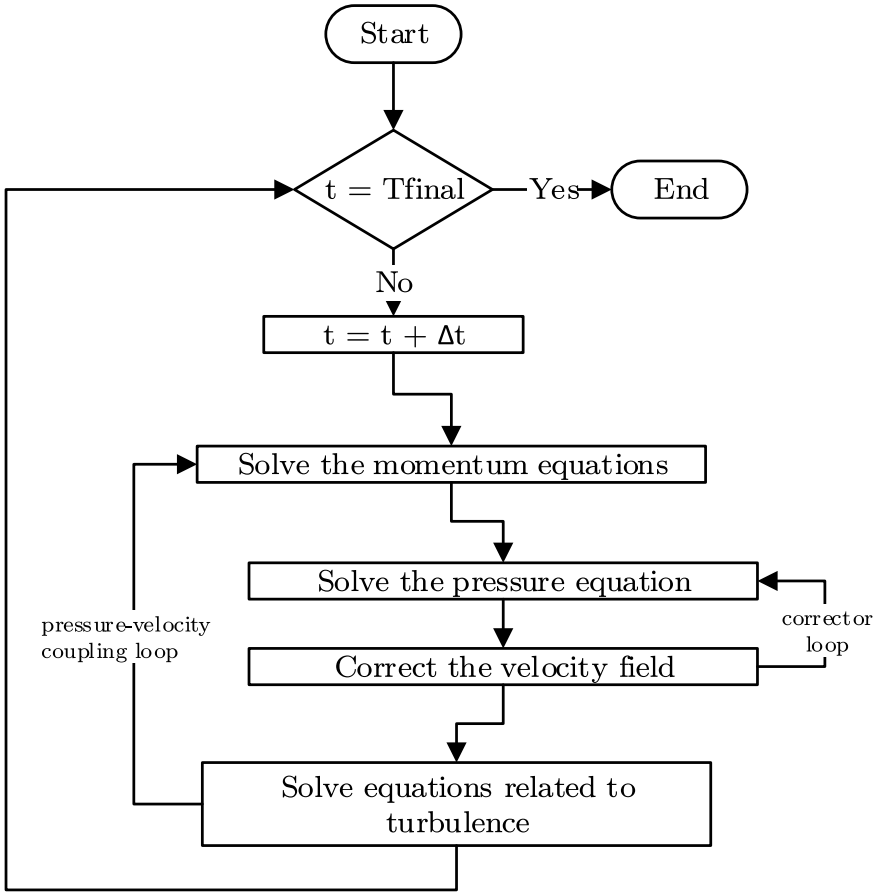

Figure 2.2: PIMPLE Algorithm. Adopted from [139].

The root mean square (RMS) of f is calculated as:

$$f_{rms}(x,y,z) = \sqrt{\frac{1}{T}\int_{t_0}^{t_0+T} [f'(x,y,z,t)]^2\, dt} \tag{2.17}$$

The averaging operation in Equation 2.15 is typically used to analyze steady flows [140]. For pulsating flows, it is more convenient to use the ensemble-averaging operator that depicts the time-varying coherent response to the pulsatility [141], defined as:

$$\langle f \rangle(x,y,z,t) = \frac{1}{N}\sum_{n=0}^{N-1} f(x,y,z,t+nT) \tag{2.18}$$

where N is the number of cycles used in the averaging operation and T is the period

of the pulsating cycle.

In order to differentiate between the scales associated with the pulsation of the flow and the scales associated with random turbulent fluctuations, the fluctuation with respect to phase average is used by using a double prime notation, defined as:

$$f''(x,y,z,t) = f(x,y,z,t) - \langle f \rangle(x,y,z,t) \tag{2.19}$$

The root mean square using the fluctuations with respect to phase average is calculated as:

$$f''_{rms} = \sqrt{\langle f''^2 \rangle} \tag{2.20}$$

It is important to understand the difference between prime and double prime notations, as the prime notation denotes the fluctuations with respect to a steady mean flow, and the double prime notation designates the fluctuations with respect to a phase average of a pulsating flow. It is also implied in Equation 2.19 that the phase average ($\langle f \rangle$) represents the time-dependent coherent, or deterministic, part of the flow and involves the time scales associated with pulsation. Substituting the phase average from the actual flow field results in the deviation from the phase average (f''), which represents the non-deterministic part and is therefore associated with turbulence.

In this study, steady flow conditions are investigated in Chapter 3, and the prime notation is used as in Equations 2.15 - 2.17. In Chapter 4, a pulsating flow is considered, thus, the double prime notation is employed as in Equations 2.18 - 2.20 in order to identify the turbulent fluctuations rather than those associated with pulsation.

CHAPTER 3

VALIDATION OF THE METHODOLOGY

This chapter presents a validation study for the use of large eddy simulation (LES) together with the WALE subgrid scale model in a simplified aortic stenosis geometry. The direct numerical simulation (DNS) study of Mittal et al. [16] is selected due to the high reliability of DNS. The same problem of the reference study is solved by LES and the results are compared.

3.1 Summary of the Reference DNS Study

The study investigates hemodynamics in a simplified aortic stenosis model with acoustic considerations relating heart murmurs and cardiac auscultation. The computational domain consists of an axisymmetrically constricted U-tube as shown in Figure 3.1. The constricted region represents a stenosed aortic valve and the level of constriction is termed as stenosis severity, defined as the percent reduction in flow area. Three different stenosis severity of 50%, 62.5% and 75% are investigated. The flow studied in the article lies in the transitional regime since the inlet flow is laminar and there is an obstruction (the stenosis) that results in turbulence. To capture the transition to turbulence, direct numerical simulation (DNS) method is used to resolve the flow field. A steady uniform inflow corresponding to a Reynolds number of 2000 is imposed at the inlet for all simulations and vessel walls are assumed to be rigid. Blood is treated as a Newtonian fluid. A sharp-interface immersed boundary method [142] is used to discretize the flow field with a mesh of approximately 18 million points. The CFL number is kept below 0.82 in all solutions. The simulations were carried out for 3.5 flow-through times, where a flow-through time is defined as the time it takes a

fluid particle to travel along the geometric centerline with the constant inlet velocity. In the post-processing part, only the last 2.5 flow-through times are used to calculate average flow statistics to exclude the effects of initial transients. The results of the study are often non-dimensionalized using the inlet velocity (V_{in}), the velocity at the throat (V_{jet}), and the diameter of the stenosis (D_{jet}). Several results are presented on the anterior surface (shown in Figure 3.1), since this surface is the closest part of the domain to human chest and used for auscultation in clinical practice.

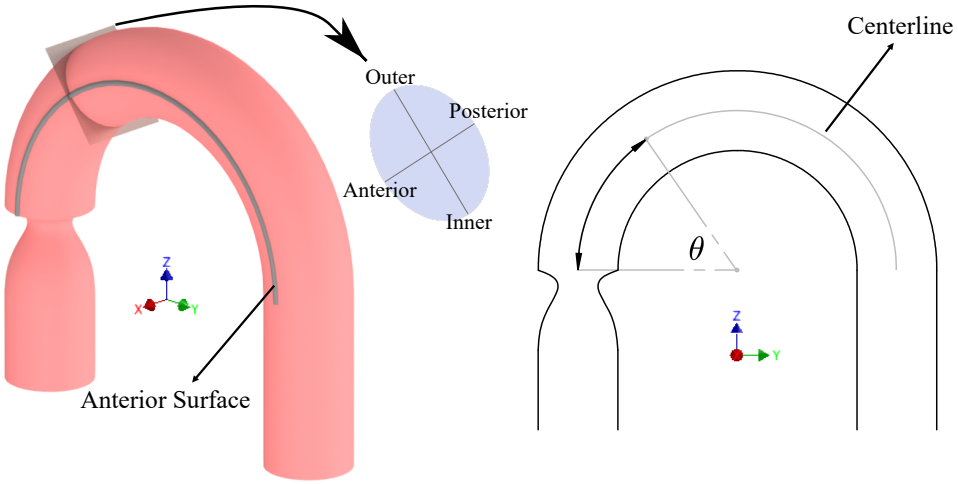

Figure 3.1: Computational domain with the terminology used for positioning (left) and definition of the θ angle on the frontal (YZ) plane (right).

The resulting flow fields showed highly turbulent flow at the post stenotic region caused by the jet originated due to the presence of the stenosis and the secondary flows induced by the curvature. In all three cases, the jet formed at the stenosis is laminar until the outer part hits the vessel wall and starts the turbulent activity in the aortic arch. The inner part of the jet further propagates downstream and starts to shed vortices with a Strouhal number of around 0.93, which is higher than the shedding frequency of a jet in a stenosed straight pipe. Among the solutions, the turbulent kinetic energy observed in the 50% stenosis case is significantly lower than the other two cases throughout the domain. An important purpose of the study was to locate the source of the murmurs, which is found by investigating the location with maximum wall pressure fluctuations. This location is found to be around $\theta = 55^{\circ}$ for the 75% stenosed case.

3.2 Large Eddy Simulation Setup

The 75% stenosed case is solved using LES since it is the most critical one among the cases analyzed in the reference study. The problem domain, inlet Reynolds number, total simulation time and data collection interval are kept the same as the reference study.

The problem geometry is recreated with a non-stenosed vessel diameter of 0.032 m, which is reported as the average human aorta diameter [143]. The blood is treated to be a Newtonian fluid with a kinematic viscosity value of 3.2×10^{-6} m^2/s. The inlet velocity is then selected to be 0.2 m/s to obtain a Reynolds number of 2000 at the inlet. The open source finite volume solver OpenFOAM is used for all calculations. WALE model is used as the SGS model and the incompressible 'pimpleFoam' solver is used as the solver. Second order implicit backward scheme is used for time discretization and second order Gaussian integration scheme is used as the gradient, laplacian and divergence schemes. Adaptive time steps corresponding to a maximum CFL number of 1 is used.

4 different structured computational grids are created using ANSYS ICEM CFD software to perform a grid refinement study. This study is not called a "grid independence study" intentionally since a grid independent LES is eventually DNS by definition. The total number of cells and the y^+ values of the grids are shown on Table 3.1. Figure 3.2 shows the coarsest grid (Grid 1) for easy visualizing, and other grids share the same configuration with increased number of cells. In this figure, a refinement region can be seen between the start of the stenosis and the $\theta = 90^\circ$ plane. All four grids are refined in this area since most of the turbulent activity and transition to turbulence occur in this region. The cells in the refinement region are 8 times smaller in volume compared to the cells outside of this region.

Table 3.1: Grid parameters.

	Number of Cells	**Max. y$^+$**
Grid 1	489405	2
Grid 2	1450416	1
Grid 3	3300780	0.75
Grid 4	7479576	0.5

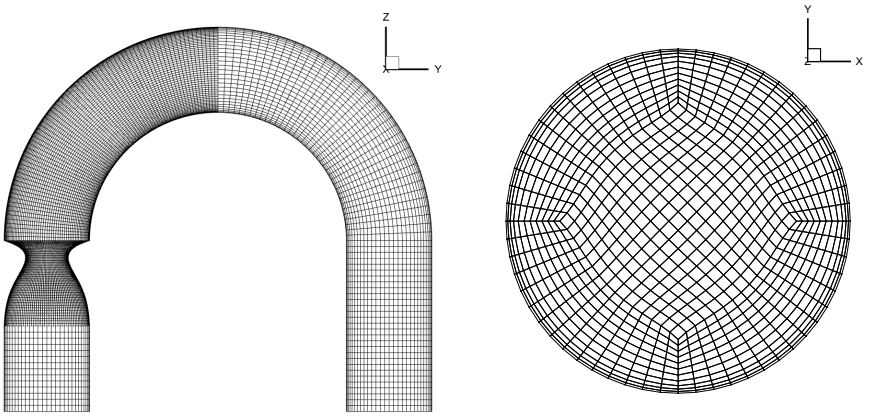

(a) (b)

Figure 3.2: Grid 1 (a) side view (b) cross-sectional view (outside the refinement region).

The simulations are run on TRUBA HPC system of TÜBİTAK ULAKBİM High Performance and Grid Computing Center using 112 cores with Xeon 6258R 2.70GHz CPUs. Solutions for Grids 1, 2, 3 and 4 took 15, 43, 109, and 233 wall clock hours, respectively.

The solutions are compared using turbulent kinetic energy (TKE), wall shear stress (WSS), pressure, and velocity results. Figure 3.3 shows the cross-sectional average of non-dimensional TKE along the aortic arch. Grid 1 produced the most distinct result among the four grids, underestimating the peak near $\theta = 65^\circ$ and generating a sharp peak near $\theta = 20^\circ$. However, it accurately predicted the location the two peaks and fitted the overall trend. There is a slight change in the slope at $\theta = 90^\circ$ in all four solutions due to the mesh boundary where the refinement region ends. The general trend of the figure shows that the coarsest grid (Grid 1) underestimates the TKE, explaining the sharp drop at $\theta = 90^\circ$, since the mesh gets coarser after $\theta = 90^\circ$ at all grids. The highest difference among Grids 2, 3, and 4 is observed between $\theta = 20^\circ$ and $\theta = 40^\circ$. This behaviour was expected since transition to turbulence occurs in this region and a fine grid is required to resolve small eddies. Grid 3 is significantly closer to Grid 4 compared to Grid 2 in this region. Other than the transition region, Grids 2, 3, and 4 produced comparable results where regular turbulent activity is present. The grids get finer from Grid 1 to Grid 4, however, not a usual monotonic convergence

trend is observed since Grids 2 and 3 overshoot near $\theta = 60°$ and Grid 2 undershoots near $\theta = 35°$. Despite these differences, Grid 2 produced an acceptable result and Grid 3 produced similar results compared to the finest grid, Grid 4.

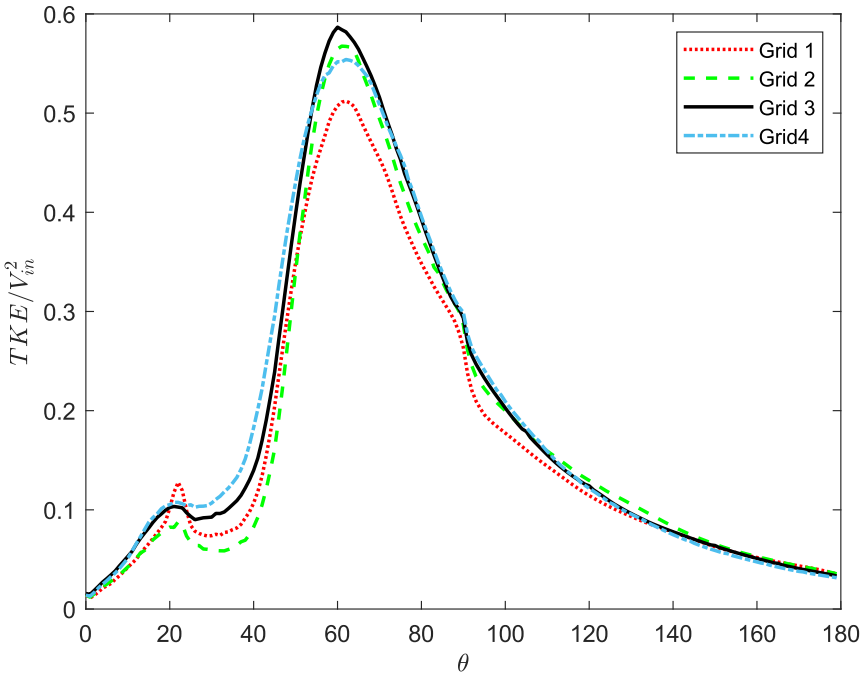

Figure 3.3: Non-dimensionalized mean TKE averaged over the cross-sectional area.

The root mean square (RMS) of WSS along the anterior surface of the arch region are plotted in Figure 3.4. The overall trends are similar and all grids predicted the location of the maximum WSS fluctuation near $\theta = 50°$. At this location, Grids 1, 2, and 3 overestimated the peak value compared to Grid 4. At the region where transition occurs, roughly between $\theta = 25°$ and the peak, all four grids produced the same slope, but Grid 4 results are higher at any given θ. Grid 3 is the closest one to Grid 4 in this transitional area. Between $\theta = 50°$ and $\theta = 180°$, Grid 2, 3, and 4 produced close results while Grid 1 deviated from the rest by generating lower values.

Figure 3.5 shows the non-dimensional velocity profiles averaged in time on the frontal plane at $\theta = 30°$. The r/R parameter defines the distance from the centerline on the frontal plane, $r/R = 1$ corresponds to the inner surface and $r/R = -1$ corresponds to the outer surface (see Figure 3.1). The first thing to notice is the nonphysical oscillations of Grid 1 between the centerline and the outer surface. This region corresponds

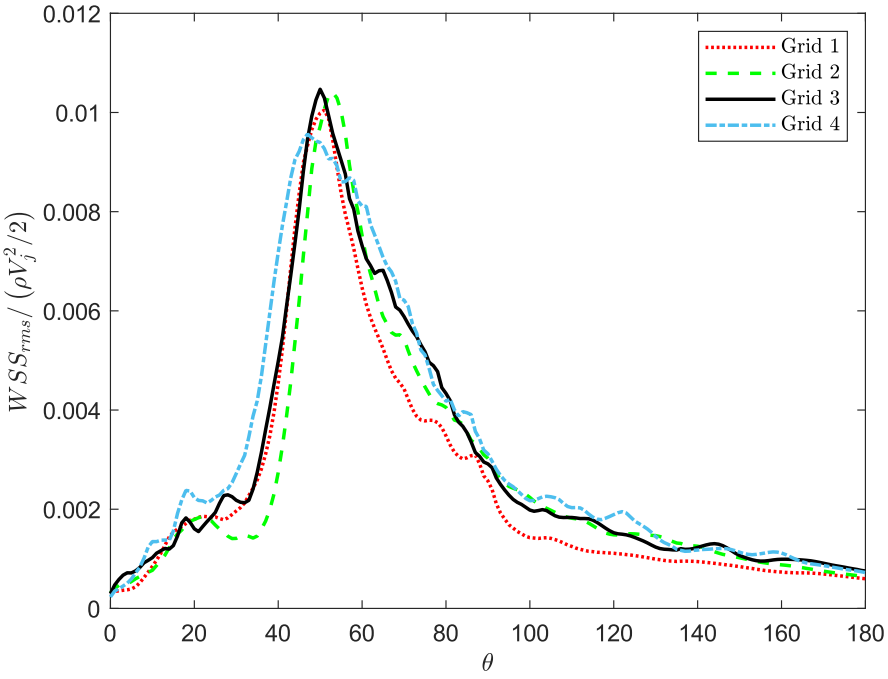

Figure 3.4: Non-dimensionalized RMS of WSS along the anterior surface

to the free jet occurring due to the stenosis and the coarse grid fails to produce meaningful results here. Small oscillations are also observed in Grid 2, but as the mesh gets finer, oscillations start to disappear in Grids 3 and 4. Small oscillations are present in Grid 3 and they tend to effect the flow field inside the free jet (will be discussed later), but the magnitude of these oscillations are much lower than the ones in Grid 2. Outside the free jet, all grids do a decent job and produce matching results.

Another parameter investigated for grid comparison is the non-dimensional pressure profiles on the frontal plane at $\theta = 60°$, shown in Figure 3.6. This figure uses the same r/R parameter as in Figure 3.5. The pressure values show that Grid 1 is separated from other grids where Grids 2, 3, and 4 produced comparable results. The lowest pressure is observed at $r/R = -0.5$ in Grid 4 solution and both Grids 2 and 3 predicted this location correctly. The lowest pressure value decreased as the grid gets finer from Grid 1 to Grid 4. Grid 2 did a decent job, but Grid 3 produced the closest results to the finest grid.

A grid assessment metric for large eddy simulations proposed by Çelik et al. [144], namely LES_IQ_ν, is also utilized to see the suitability of the grids. The LES_IQ_ν

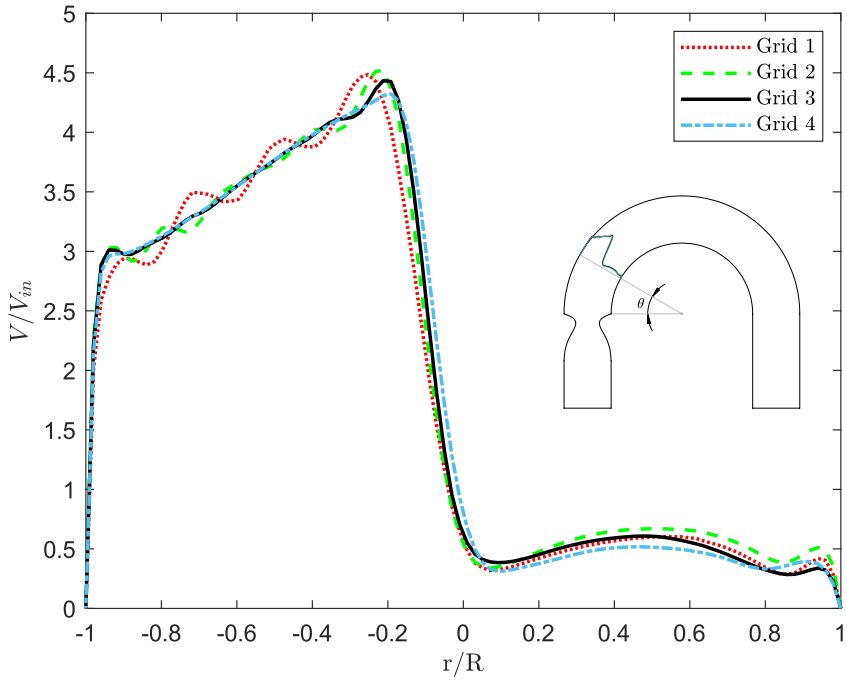

Figure 3.5: Non-dimensionalized mean velocity profiles on the frontal plane at $\theta = 30$

metric is defined as:

$$LES\_IQ_{\nu} = \frac{1}{1 + \alpha_{\nu} \left(\frac{\nu_{eff}}{\nu}\right)^{n}} \tag{3.1}$$

where ν_{eff} is the effective kinematic viscosity, or relative subgrid viscosity with respect to molecular viscosity, and $\alpha_{\nu} = 0.05$ & $n = 0.53$ are constants [127]. An LES_IQ value greater than 0.8 indicates a good LES solution, and $LES\_IQ > 0.95$ is considered as DNS [144]. Grids 1, 2, 3, and 4 resulted in LES_IQ_{ν} values of 0.84, 0.87, 0.89, and 0.90, respectively. The results indicate that all four grids are suitable for an LES solution, and Grid 3 is much closer to Grid 4 compared to Grid 2.

Finally, the Kolmogorov length scale (η) is calculated for all grids, defined as:

$$\eta = \left(\frac{\nu^3}{\varepsilon}\right)^{1/4} \tag{3.2}$$

where ε is the average rate of dissipation of turbulence kinetic energy per unit mass

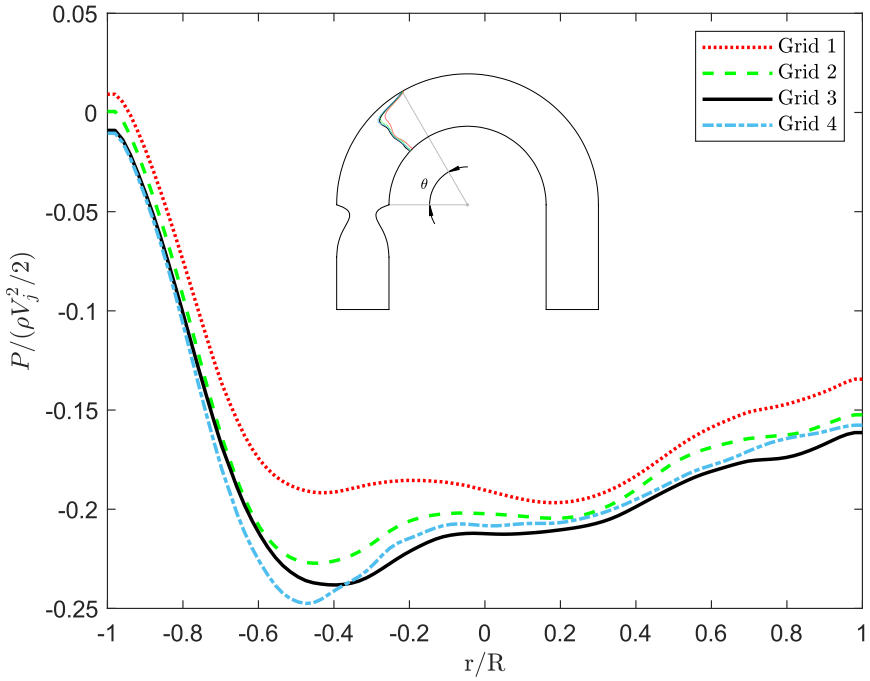

Figure 3.6: Non-dimensionalized mean pressure profiles on the frontal plane at $\theta = 60$

and ν is the kinematic viscosity of the fluid. The suitability of the grids is checked by calculating the ratio of the cell size to the Kolmogorov length scale. Çelik et al. [127] stated that this ratio for a coarse grid is around 40 and it is around 20 for a fine grid for LES studies. The ratio of the cell size to the Kolmogorov length scale is calculated as 36, 24, 20, and 15 for Grids 1, 2, 3, and 4, respectively. Therefore, both Grids 3 and 4 are considered as fine grids and can be used for LES applications.

Considering Figures 3.3 to 3.6 and the ratios of the cell size to the Kolmogorov length scale, Grids 2, 3, and 4 can be useful for the problem being solved. The computational resource required for Grid 4 is beyond the feasible limits. Grid 2 performed efficiently considering the low number of cells it has and can be used when the resources are limited. Grid 3 produced the closest results to Grid 4 with acceptable computational resources and it is selected to be the most appropriate grid. Therefore, Grid 3 is used for the remainder of the study.

3.3 Results and Discussion

In this section, LES results obtained with Grid 3 are compared with the results of the reference DNS solution [16].

3.3.1 Vortex Dynamics

Figure 3.7 shows the x-component of the instantaneous vorticity contours on the frontal plane. The time instant that the contour is taken from the DNS solution is unknown. The results of LES and DNS are not expected to be identical since the contours are instantaneous, but they share great resemblance. The DNS result shows that a jet occurs right after the stenosis. The outer part of the jet attaches to the outer wall and creates a thin boundary layer. The inner part of the jet starts to shed vortices, shown by arrow C. Two recirculation zones are observed due to the jet: one small region at the back of the outer part of the jet, shown by arrow A, and a larger one in the aortic arch, shown by arrow B. The free jet at the post stenotic region, two recirculation zones shown by arrows A and B, and vortex shedding shown by arrow C are also present in the LES solution. The location at which vortex shedding occurs is similar for the two solutions. The large recirculation zone shown by arrow B is also observed in the LES result, magnitude and size of the vortices are close to each other in this region. It can be observed in the DNS solution that there is an intense turbulent activity until $\theta \approx 110^\circ$, and less turbulent activity is present (more white contours) at $\theta > 110^\circ$. A similar phenomenon is observed in the LES solution, however, the turbulent activity is reduced at $\theta = 90^\circ$. This drop of turbulent activity can also be observed in Figure 3.3 at $\theta = 90^\circ$ and is due to the mesh boundary at this location, where the grid gets coarser. Between $\theta = 90^\circ$ and $\theta = 110^\circ$, the LES grid is not fine enough to resolve small eddies, therefore the TKE is slightly underestimated. However, it is well known from the DNS solution that the most critical region is from $\theta = 25^\circ$ to $\theta = 75^\circ$, therefore the mesh refinement area extends until $\theta = 90^\circ$ and not any further. The refinement region is also kept restricted due to limited computational resource. In the descending aorta, turbulent activity is mostly died out in both solutions: small eddies are not observed and more white contours are present, indicating that the effects of the stenosis and the aortic arch are damped.

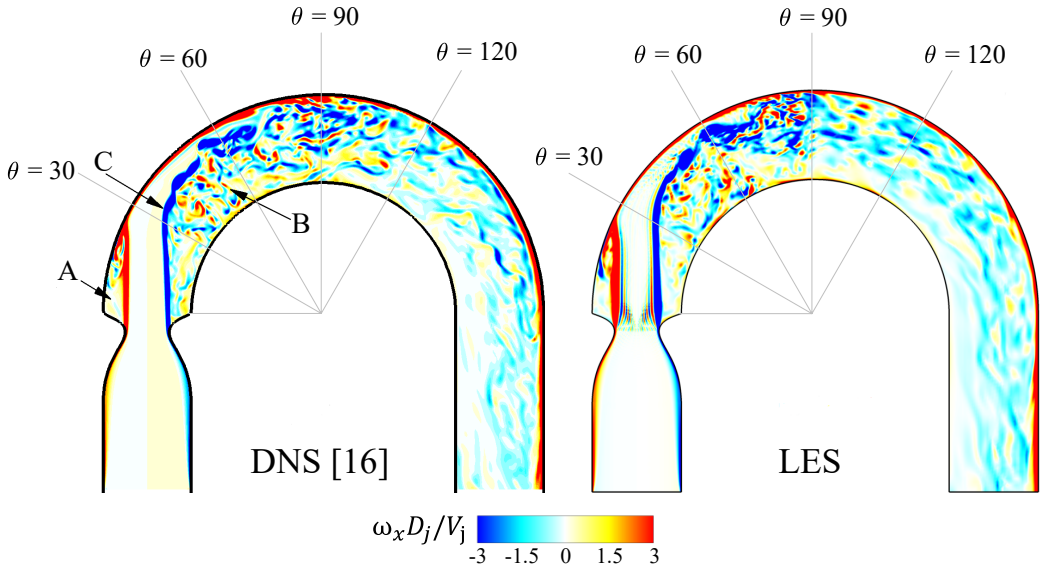

Figure 3.7: Non-dimensional instantaneous vorticity distribution on the frontal plane.

There is a significant difference between the solutions inside the free jet. The amount of rotation is almost zero inside the jet in the DNS solution, but the LES contour shows a nonphysical pattern of red and blue colors (high vorticity) right after the stenosis. This phenomenon is related to the oscillations that are present inside the jet (see Figure 3.5) but they tend to decrease as the grid gets finer. The LES solution acts poorly in this area due to mesh resolution, but it is not found necessary to further refine the mesh at the throat since the region is not of high interest and mesh metrics of y^+ and the ratio of cell size to Kolmogorov length scale are satisfactory as mentioned in Section 3.2.

Figure 3.8, adopted from [16], explains the terminology used in the analysis of vortex dynamics. The primary vortex region consists of the Dean vortices occurring due to the curvature of the vessel. The vorticity deficit region at the top shows the core of the jet and the secondary vortical region is related with the shear layer around the jet.

Figure 3.9 compares the variations in streamwise vorticity in the aortic arch for LES and DNS solutions. The contours are plotted at cross-sectional planes at selected θ angles. At $\theta = 35°$, primary and secondary vortical regions are clearly observed in both solutions. The clockwise (negative valued) primary vortex region is weaker than the counter-clockwise vortex region in the DNS solution, but the difference between

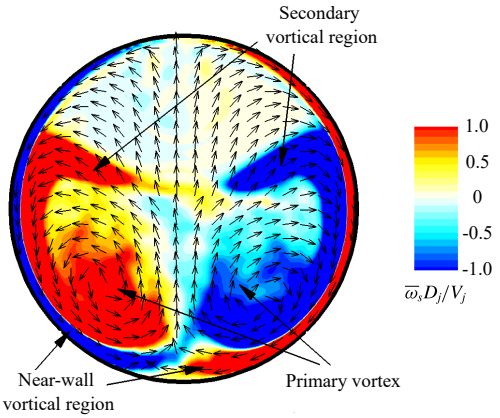

Figure 3.8: DNS results of mean streamwise vorticity at $\theta = 45°$ for 62.5% stenosis severity. Adopted from [16].

the two primary vortices is more subtle in the LES result, especially at $\theta = 45°$. Inside the jet, the nonphysical pattern is observed again as discussed for Figure 3.7. The low vorticity region due to the jet gets smaller as the angle θ increases since the jet hits the wall and vortical structures dominate the flow. When Figures 3.7 and 3.9 are examined together, an agreement is seen, the jet area decreases from $\theta = 35°$ to $\theta = 45°$ and the vortex free region almost disappears at $\theta = 55°$. The secondary vortical regions totally disappear at $\theta = 55°$ in the DNS solution, but they are not completely dissipated in the LES result, meaning that the effects of the core of the jet is present further downstream in LES solution. From $\theta = 35°$ to $\theta = 65°$, it can be observed in the DNS contours that the primary vortical regions dissolve into small vortices, but they tend to preserve the bulk motion in the LES solution. This is mainly due to the difference in cell size between the two solutions. The smaller cells in DNS can resolve the dissipation of small vortices into energy whereas this behavior is modelled in LES. At $\theta = 95°$, the bilateral symmetry of clockwise and counter-clockwise rotating flow disappears in the DNS solution, however, there is still a subtle symmetry in the LES result, meaning that the effects of secondary flows due to the curvature of the vessel are still present in the LES solution. At $\theta = 135°$, the similarity between LES and DNS increases as large vortex structures die out and turn into weaker vortices and the effects of stenosis and vessel curvature are diminished. In summary, the variations between the solutions are acceptable and LES can be used to analyse the post-stenotic vortex dynamics.

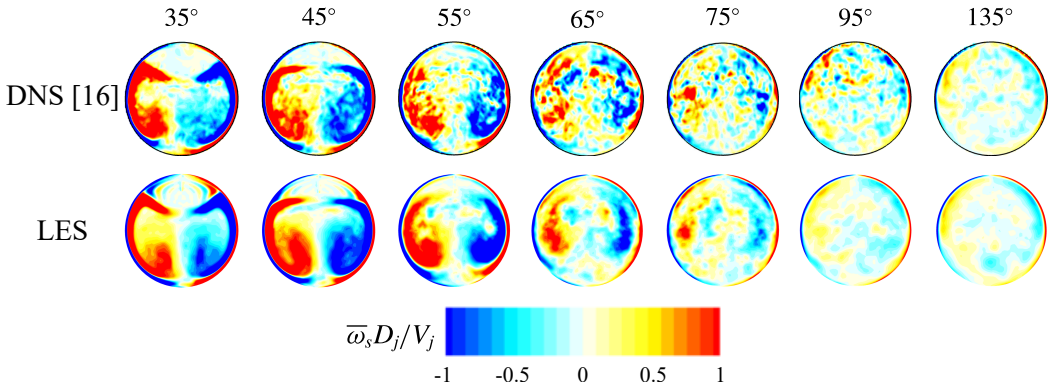

Figure 3.9: The non-dimensionalized mean streamwise vorticity plotted at selected θ.

3.3.2 Transition to Turbulence

The flow studied in this problem involves transition to turbulence due to the presence of the stenosis, therefore it is crucial to investigate the turbulent kinetic energy and compare the transition process with the reference DNS solution. Figure 3.10 shows the cross-sectional average of turbulent kinetic energy along the aortic arch for both DNS and LES solutions. The first thing to notice is the underestimation of TKE at $\theta = 20°$. From Figure 3.7, it can be seen that the $\theta = 20°$ plane coincides with the free jet and the small recirculation zone denoted by arrow A. Inside the free jet is mostly laminar flow, therefore LES predicts the TKE higher than DNS in the small recirculation zone. From $\theta = 40°$ to $\theta = 60°$, the turbulent kinetic energy is well predicted by LES, considering this region also includes transition to turbulence. The maximum point of LES at $\theta = 60°$ is slightly higher than the DNS solution, but the location of the maximum TKE is correctly determined. From $\theta = 70°$ to $\theta = 120°$, the turbulent kinetic energy drops in both solutions, however, the slope of this drop is sharper in LES. The TKE is underestimated by LES in this region, and a sharp change in slope is observed due to mesh boundary as discussed for Figures 3.3 and 3.7. Despite the differences, LES predicted the overall trend correctly by matching the DNS results mostly and correctly showing the location of the two peaks.

Figure 3.11 shows the change in turbulent kinetic energy in the aortic arch at several cross-sectional planes for selected θ values. The contours agree with the vorticity distribution on the frontal plane shown in Figure 3.7. The flow is predominantly

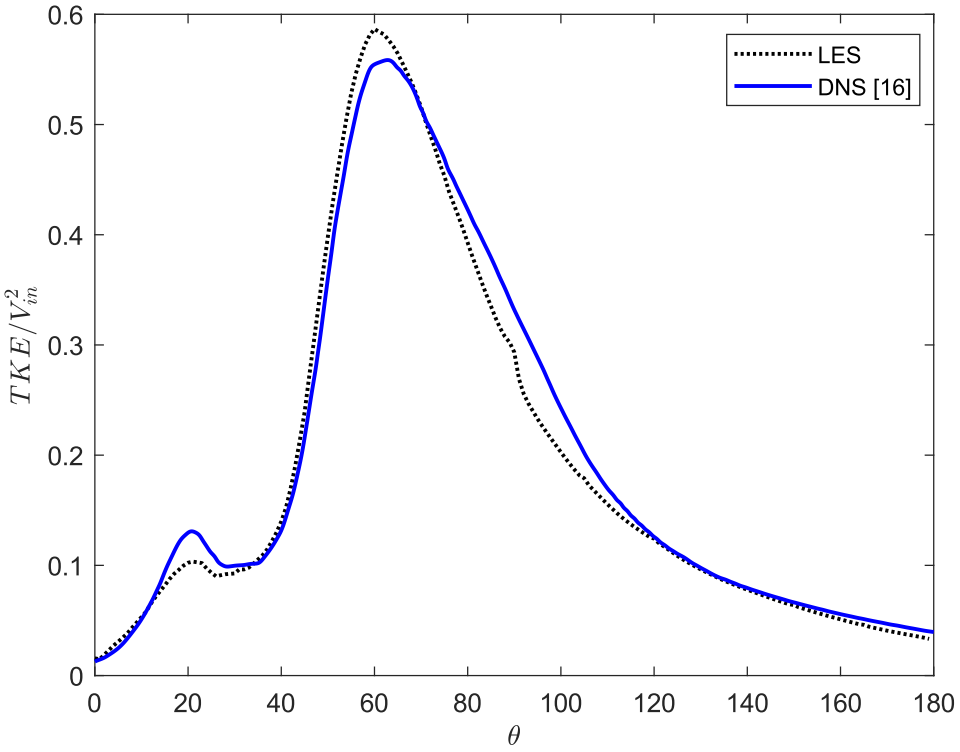

Figure 3.10: Non-dimensionalized mean TKE averaged over the cross-sectional area.

laminar at the initial stage of the jet downstream of the $\theta = 35°$ plane, and the level of turbulence increases with increasing θ values as the vortex shedding starts. The TKE deficit region is seen in white contours in both solutions at $\theta = 35°$, coinciding with the laminar jet. Similarly, a high TKE region with yellow and red colors is observed just below the free jet, corresponding to the shear layer around the jet. At $\theta = 45°$, there is a small high-TKE region in both solutions due to the vortex shedding that can be seen in Figure 3.7. One difference between the solutions at $\theta = 45°$ is that the white region corresponding to the jet almost disappeared in the DNS result but there is still a small zero vorticity region in LES, meaning that the effects of the free jet is observed further downstream in the LES solution. The same effect was observed in Figure 3.9, where secondary vortices were still slightly present at $\theta = 55°$ but they dissolved in the DNS solution. This phenomenon will later be proved in Section 3.3.4 by showing that the vortex shedding starts slightly later in the LES solution compared to the DNS study. Figure 3.11 further shows that highly turbulent flow is observed from $\theta = 55°$ to $\theta = 75°$ in both solutions. The magnitude and shape of

the contours agree well with each other in this interval. When Figures 3.9 and 3.11 are examined together, the effects of both primary and secondary vortical regions can be observed. The high turbulent kinetic energy region forms a bridge-like shape that partially overlaps with Dean vortices and the secondary vortical region, indicating that both the curved vessel geometry and the vortex shedding of the jet contribute to the stochasticity of the flow. TKE starts to decrease after $\theta = 75°$ since large vortices disintegrate into smaller ones and less turbulent activity is observed at $\theta = 95°$ and $\theta = 135°$ planes.

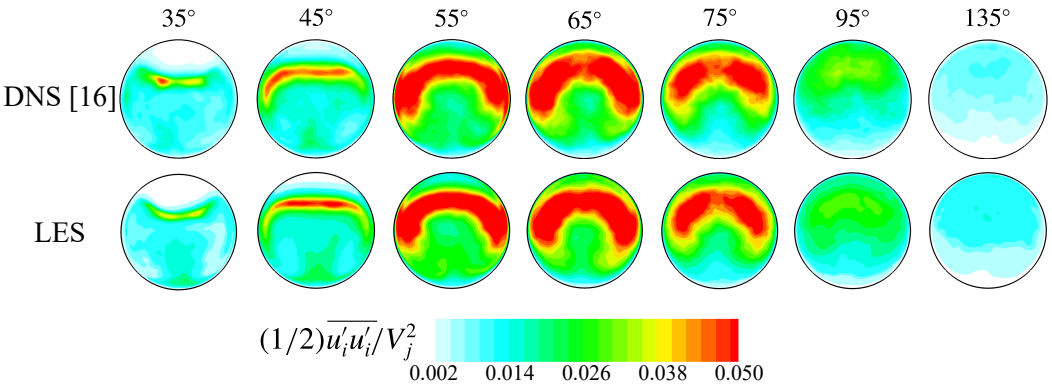

Figure 3.11: The non-dimensionalized mean TKE plotted at different theta planes.

One of the main differences between the solutions observed in Figure 3.10 was the higher TKE value in the LES result at $\theta = 60°$. When this difference is investigated in more detail in Figure 3.11 at $\theta = 65°$, the closest angle to $\theta = 60°$, it can be seen that there is not a critical difference between the solutions and LES performs accurate enough in predicting both magnitude and the pattern of TKE. The underestimation of TKE in LES at $\theta = 95°$ observed in Figure 3.10 can also be seen in Figure 3.11, but the contours show no significant difference. The difference observed at $\theta = 20°$ in Figure 3.10 cannot be discussed by Figure 3.11 since the contour is not provided in the DNS study, but the comparison for $\theta = 65°$ and $\theta = 95°$ indicates that the difference might not be as significant as it seems in Figure 3.10.

Examination of Figures 3.10 and 3.11 shows that LES is capable of capturing the TKE correctly in both the transitional and the post-stenotic regions.

3.3.3 Surface Force Analysis

One of the most important aims of the reference DNS study was to investigate the generation of murmurs that are caused by wall pressure fluctuations. Hence, the RMS of pressure contours of LES and DNS solutions are compared, as shown in Figure 3.12. It is observed in both solutions that the region right after the stenosis and the location where the jet impinges on the wall are regions of low pressure fluctuations. The regions of high pressure fluctuations coincide with the two recirculation zones shown by arrows A and B in Figure 3.7 since highly turbulent flow is observed in these areas. The two results show that the fluctuation patterns and their magnitudes are in agreement. The main difference is the sizes of the highly fluctuating regions (roughly between $\theta = 40°$ and $\theta = 70°$). This region in DNS is larger compared to the LES result, in which the high magnitude fluctuations are more condensed. The correlation between TKE and the wall pressure fluctuations can further be observed when Figures 3.12 and 3.11 are examined together. The highest turbulent activity is observed at $\theta = 55°$ and $\theta = 65°$ in Figure 3.11, corresponding to the highest pressure fluctuations in Figure 3.12.

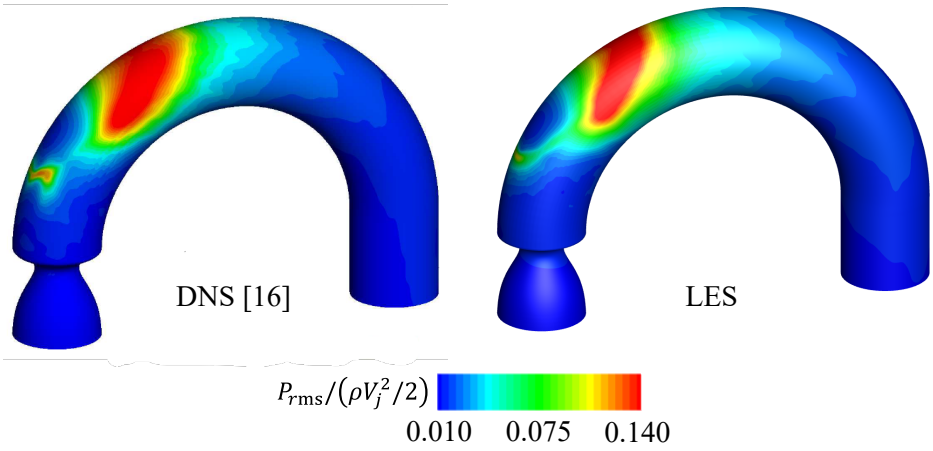

Figure 3.12: The non-dimensionalized RMS of surface pressure distribution.

Wall pressure fluctuations are further investigated on the anterior surface since it is the closest surface to human chest where the murmurs are detected. Figure 3.13 shows the comparison of non-dimensional magnitude of wall pressure fluctuations along the aortic arch on the anterior surface for the two solutions. It is firstly noticed that the maximum magnitude of the pressure fluctuations is overestimated by 6% in the LES

solution. Not only the magnitude, but also its location is important since this location is associated with the source of the murmurs. The DNS study found this location as $\theta = 55°$, and LES predicted it to be at $\theta = 50°$. It is also observed in the figure that the difference between LES and DNS solutions is mainly in the region between $\theta = 35°$ and $\theta = 55°$ planes, where transition occurs and it is the hardest to capture flow characteristics. The results agree very well with each other outside of the transition region. Examination of Figures 3.12 and 3.13 shows that LES can closely predict the source location of murmurs and the amplitude of wall pressure fluctuations compared to DNS results.

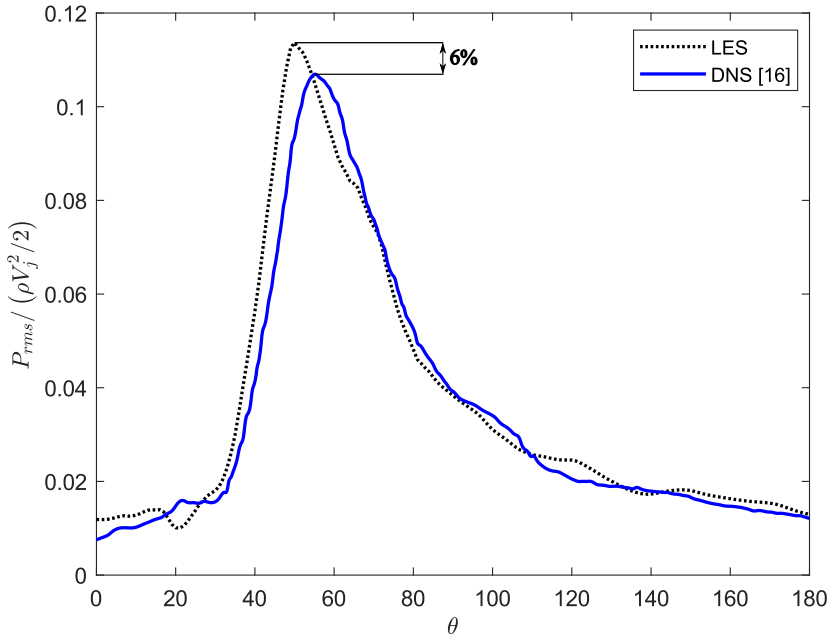

Figure 3.13: The non-dimensionalized RMS of pressure plotted along the anterior surface.

Wall shear stress fluctuations also affect the generation of murmurs in addition to wall pressure fluctuations. Therefore, RMS of WSS is shown along the aortic arch in Figure 3.14 and along the anterior surface in Figure 3.15. A significantly higher magnitude is observed in both figures for the LES solution. The maximum WSS fluctuation occurred at $\theta = 55°$ in both solutions as can be seen in Figure 3.15. Although there is a clear difference between the LES and DNS solutions, it should be noted that the magnitude of WSS fluctuations are only about 5% of the magnitude of wall pressure fluctuations, indicating that the role of WSS fluctuations is not as

significant as the wall pressure fluctuations in the generation of murmurs.

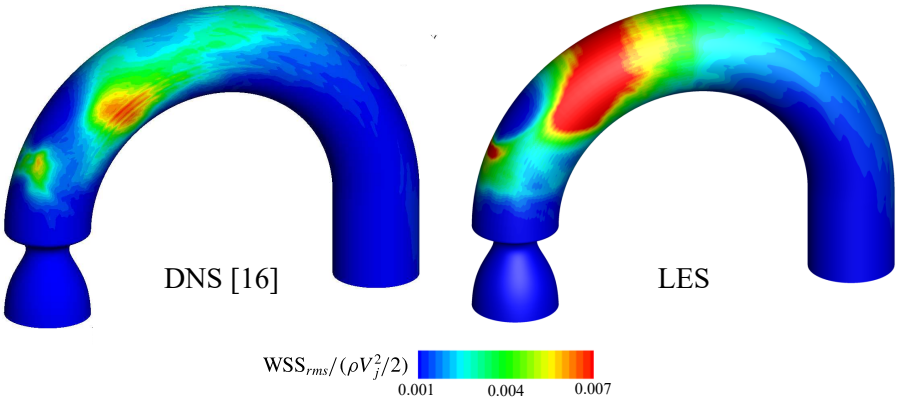

Figure 3.14: The non-dimensionalized RMS of WSS distribution.

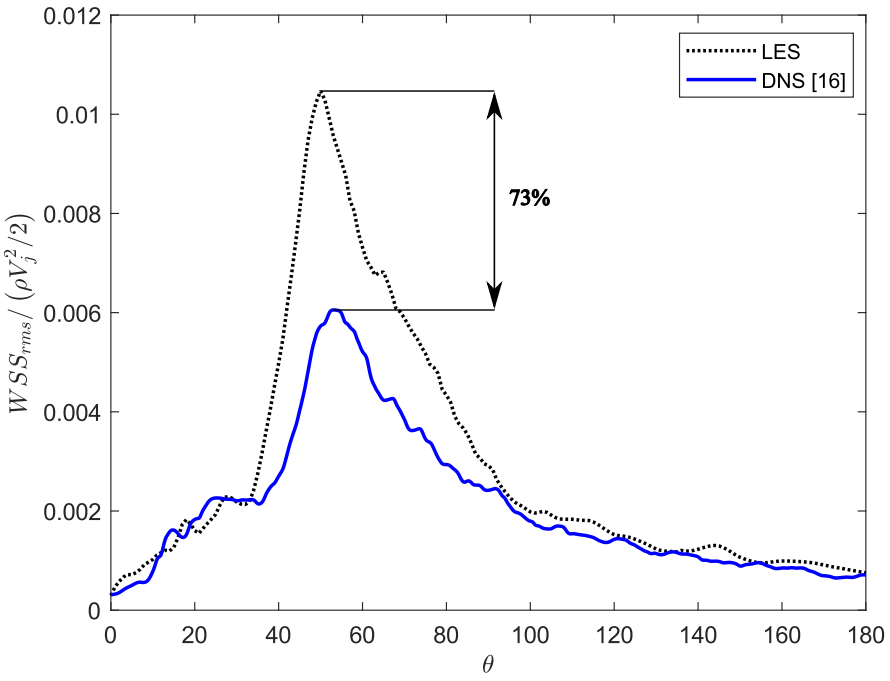

Figure 3.15: The non-dimensionalized RMS of WSS plotted along the anterior surface.

The difference between LES and DNS solutions is the highest in WSS values as seen in Figures 3.14 and 3.15, with a 73% difference in the maximum WSS value. Due to this high difference, the finest grid (Grid 4) is also checked out of curiosity. A comparison of RMS of WSS among different LES solutions was shown in Figure 3.4, in which it can be seen that Grid 4 has the lowest value at the maximum point.

When compared with the reference DNS solution, the error of Grid 4 is found to be 58%, which is lower than the error of Grid 3 but still a high value. The error difference between Grids 3 and 4 is not as significant as the difference in the required computational power of the two grids, therefore using Grid 3 was the better option.

3.3.4 Spectral Analysis

Wall pressure fluctuations are the most dominant cause of murmur generation as discussed in Section 3.3.3. In this section, these lumenal pressure fluctuations are further investigated. Figure 3.16 shows the temporal history of pressure fluctuations at $\theta = 35°$ on the centerline and the anterior surface. It is first noticed that the initial transients of the LES solution has much higher amplitude compared to DNS, but these fluctuations are not included in the results since the averaging process starts at $tV_j/D_j = 100$. The magnitude of pressure fluctuations is lower on the centerline compared to the anterior surface in both solutions. The plots are not expected to match for LES and DNS since they show instantaneous data at a single point, but it can be seen that the magnitude and frequency of the fluctuations are well predicted by the LES solution.

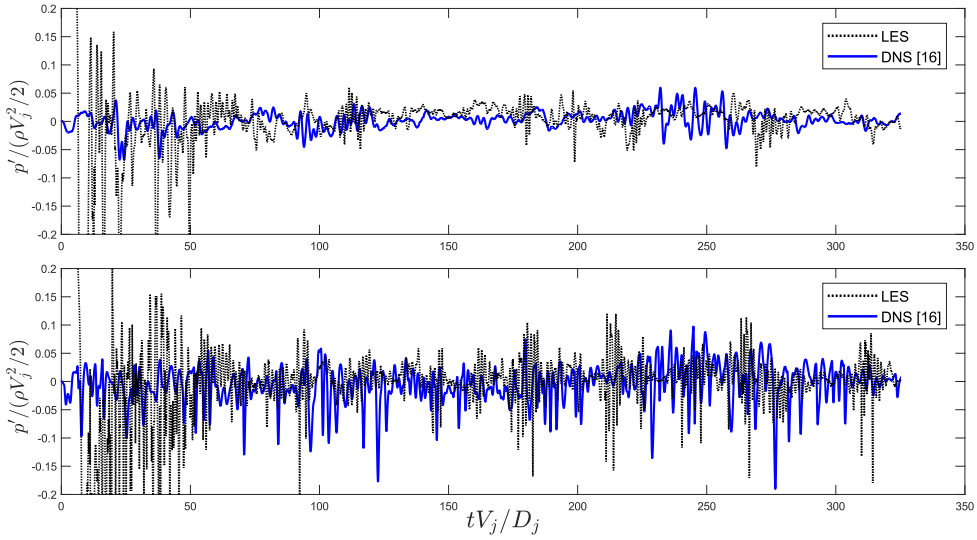

Figure 3.16: The temporal variation of non-dimensionalized pressure fluctuations at $\theta = 35°$ on the centerline (top) and on the anterior surface (bottom).

Figures 3.17 and 3.18 show the changes of pressure spectra along the centerline for

DNS and LES solutions, respectively. In these figures, spectrum of pressure fluctuations (E_p) is defined as $\langle p' \rangle / (\rho V_j^2)/2$ and the Strouhal number for steady flow (St_s) is defined as fD_j/V_j, where the $\langle\ \rangle$ symbol means ensemble averaging and Figure 3.18 is prepared by averaging 17 time intervals with each having a duration of 0.5 seconds ($25D_{jet}/V_{jet}$), using the polyphase anti-aliasing filter of MATLAB. The number of averaging intervals and duration are decided upon a series of trials by increasing the number of averaging intervals until the results do not change. The averaging and filtering details of the DNS solution are unknown.

The comparison of Figures 3.17 and 3.18 shows a difference in the magnitude of the pressure fluctuations between the two solutions. The lowest pressure fluctuation values observed for $\theta = 20^\circ,\ 40^\circ,\ 75^\circ$ are around 10^{-6} in the DNS solution, but they are around 10^{-5} in the LES solution. This means that the LES solution was not able to capture small fluctuations due to the coarser grid used. Both solutions show the lowest pressure fluctuations at $\theta = 0^\circ$, but the $\theta = 0^\circ$ line is well separated from the rest in the DNS solution, meaning that the flow is predominantly laminar at this location. As the angle increases, the pressure fluctuations start to increase as the flow transitions into turbulence. In the LES solution, however, the $\theta = 0^\circ$ line is considerably close to the $\theta = 20^\circ$ line, meaning that the fluctuation intensity is overestimated at $\theta = 0^\circ$. One reason for this difference is the nonphysical oscillations observed near $\theta = 0^\circ$ in Figure 3.7, introducing artificial fluctuations and corrupting the result at $\theta = 0^\circ$. As the angle θ increases, higher pressure fluctuations are observed and the trend is similar with the reference DNS solution.

One of the motivations of the spectral analysis is to identify the 'break frequency', also called the 'corner frequency'. Break frequency corresponds to the frequency that the slope changes significantly in the pressure spectra figures. It is important to evaluate the break frequency since it is used for determining the degree of the stenosis in auscultation based clinical practices [145]. It is seen in Figure 3.17 that a sharp change in slope is present at $St_s = 0.93$ (denoted with the vertical black line) for the spectrum at $\theta = 20^\circ$. This sharp change shows the discrete-frequency vortex shedding of the shear layer surrounding the jet where the flow starts to transition into turbulence. The peak at $St = 0.93$ also shows that the flow is dominated by the vortex shedding and the corresponding frequency is identified as the break frequency. The

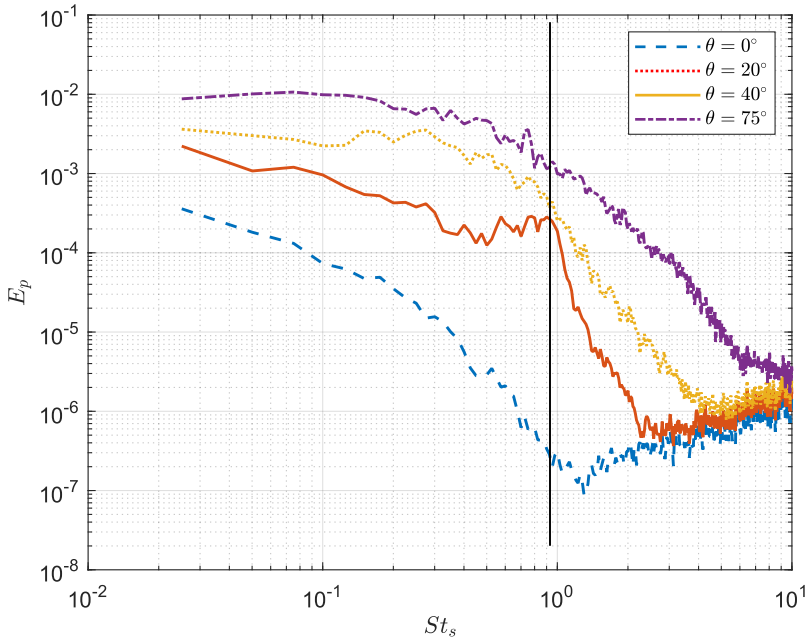

Figure 3.17: Spectra of pressure fluctuation plotted at selected θ along the centerline (DNS). Adopted from [16].

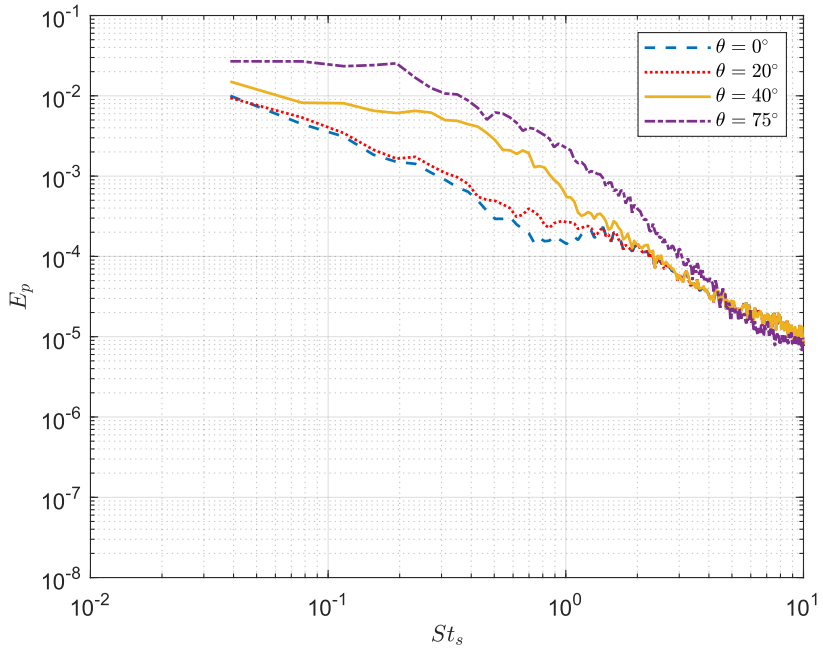

Figure 3.18: Spectra of pressure fluctuation plotted at selected θ along the centerline (LES).

LES solution does not provide a clear peak at $\theta = 20°$ as can be seen in Figure 3.18. In order to find the break frequency, several locations near $\theta = 20°$ are investigated

in the LES solution and a peak is observed at $\theta = 25°$ as shown in Figure 3.19. The dashed vertical line is the break frequency identified in the DNS solution ($St = 0.93$) and the full line is the break frequency determined by LES ($St = 0.99$). It is safe to say that the two break frequencies are close to each other since the value predicted by LES lies within 6% of the DNS result. The occurrence of the peak at $\theta = 25°$ shows that the periodic vortex shedding starts slightly later in the LES solution compared to DNS. This can also be seen in Figure 3.3, where DNS has higher TKE at $\theta = 20°$, where the vortex shedding has not yet started in the LES solution.

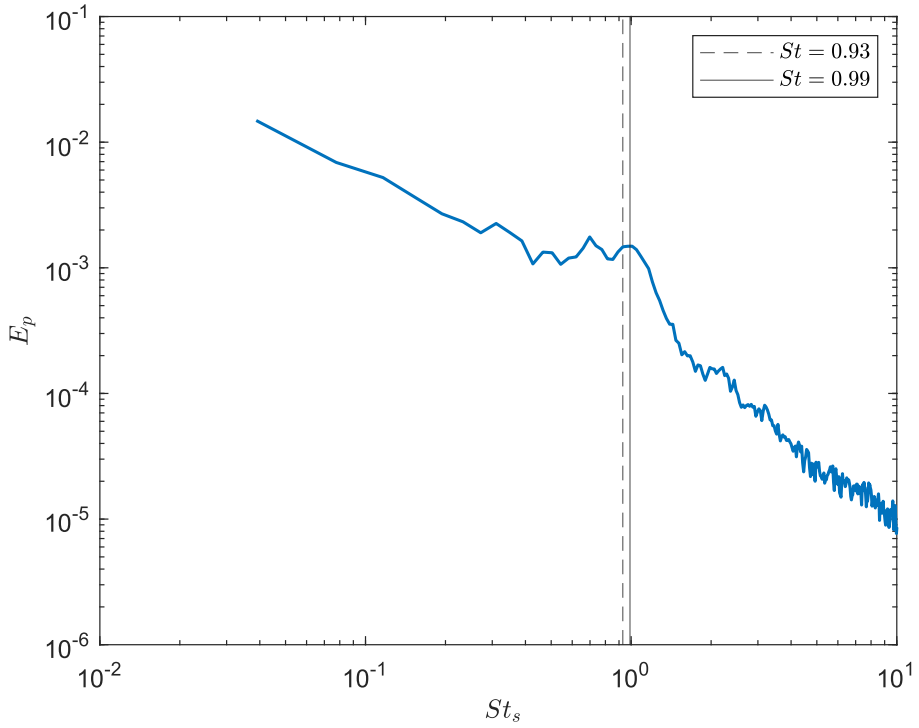

Figure 3.19: Spectra of pressure fluctuation plotted at $\theta = 25$ at the centerline (LES).

3.4 Conclusion

The validation study is performed to test the ability of large eddy simulations with the WALE model in an application that resembles an aortic stenosis geometry that involves secondary flows and transition to turbulence.

The comparison of results demonstrated that despite some differences in the results,

especially in WSS, the main findings of the reference DNS study are well predicted by LES. Firstly, the transition to turbulence is resolved with acceptable errors. The periodic vortex shedding is captured and TKE along the arch is found sufficiently close to DNS results. Secondly, the location of the maximum wall pressure fluctuations, which are known to be the primary source of murmurs, was found to be at $\theta = 55^{\circ}$ in the DNS solution and it is found at $\theta = 50^{\circ}$ in the LES solution. The intensity of the pressure fluctuations is calculated within 6% of error. Lastly, the break frequency was observed at $St = 0.93$ in the DNS solution and it found at $St = 0.99$ in the LES solution.

In comparing LES and DNS results, it is important to notice that identical results are not expected since LES involves modeling whereas DNS directly resolves the flow field. Moreover, performing a DNS study requires much more computational resource compared to an LES study. Indeed, the reference DNS study required 62976 core-hours [16] and the LES study required 12208 core-hours, additionally, the cores used for the DNS study have higher performance. This means that the DNS solution requires more than 5 times the computational resource used for the LES solution.

By being aware of its shortfalls, LES with the WALE subgrid scale model is accepted to be appropriate for CFD analyses of aortic stenosis cases.

CHAPTER 4

EFFECTS OF STENOSIS SEVERITY ON AORTIC HEMODYNAMICS UNDER PULSATILE FLOW CONDITIONS

The severity of stenosis, namely the reduction in flow area, is a significant parameter in clinical practice for both diagnosis and treatment of aortic stenosis conditions. Auscultation-based diagnosis methods are highly dependent on the severity of stenosis, as the intensity of the generated noise is influenced by the degree of stenosis [110]. Therefore, this chapter aims to investigate the effects of stenosis severity on aortic hemodynamics and aortic murmurs. The problem solved in Chapter 3 is modified to have pulsating inflow conditions to represent the physiological nature of aortic blood flow, and the domain is edited to have stenosis severities of 0% (unstenosed), 50% (mild), and 75% (severe) as shown in Figure 4.1. Large eddy simulations with the WALE subgrid-scale model are conducted in the open-source finite volume solver OpenFOAM.

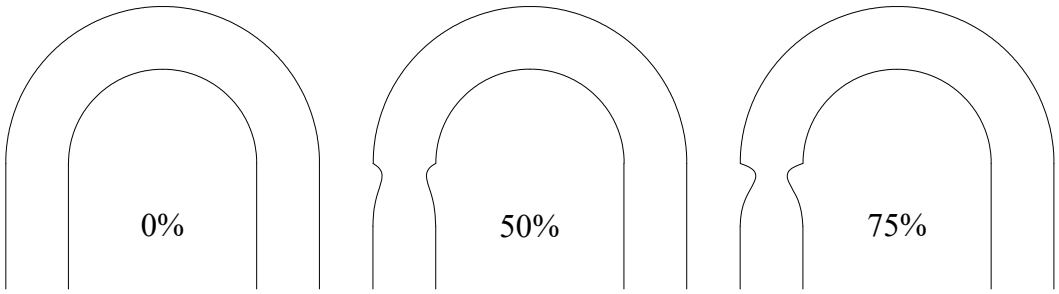

Figure 4.1: Problem cases.

4.1 Computational Setup

The stenosis severity of the geometric model used in Chapter 3 is changed according to the following equations [16]:

$$r(z) = \frac{D}{2}\left\{1 - \frac{D - D_j}{D}\frac{exp(-a(z - z_0))\ sin\left[\pi(z - z_0)/0.8D\right]}{exp(-aD)\ sin(0.8\pi)}\right\} \tag{4.1}$$

$$a = \frac{\pi}{D\ tan(0.8\pi)} \tag{4.2}$$

where r is the radius of the stenosis varying with z, D_j is the minimum diameter of the stenosis and z_0 is the starting point of the stenosis in the z-direction as shown in Figure 4.2.

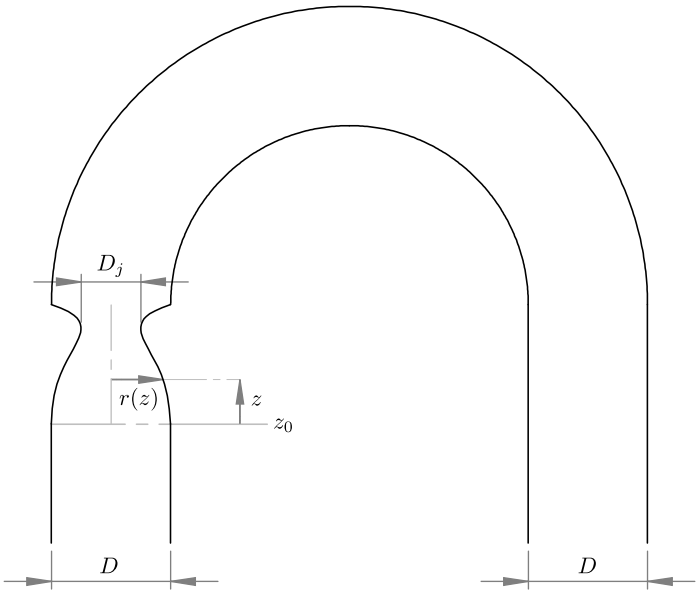

Figure 4.2: Parameters defining the stenosis geometry.

A physiologically pulsating velocity waveform shown in Figure 4.3 is imposed at the inlet. This velocity waveform is taken from the work of Morris et al. [47], where the profile is obtained by a Fourier trigonometric fit using 10 harmonics based on clinical flow rates. The same velocity waveform is also used in other studies [54, 58]. The mean of the velocity waveform (V_{mean}) is set to the inlet velocity used in Chapter 3 and therefore corresponds to a mean Reynolds number of 2000. The maximum

Reynolds number of the flow cycle is 4800, which represents a realistic value since the average peak aortic Reynolds number of 30 volunteers is found to be 4500 by Stalder et al. [69]. The key instants are marked in Figure 4.3 as T1-T6 and are commonly used in the remainder of the chapter. Finally, the flow waveform is mapped into a parabolic velocity profile as shown in Figure 4.4, since parabolic velocity profiles generate realistic results as discussed in Section 1.3.5. The MATLAB code for generating a time dependent parabolic velocity profile for OpenFOAM simulations is provided in Appendix B.1.

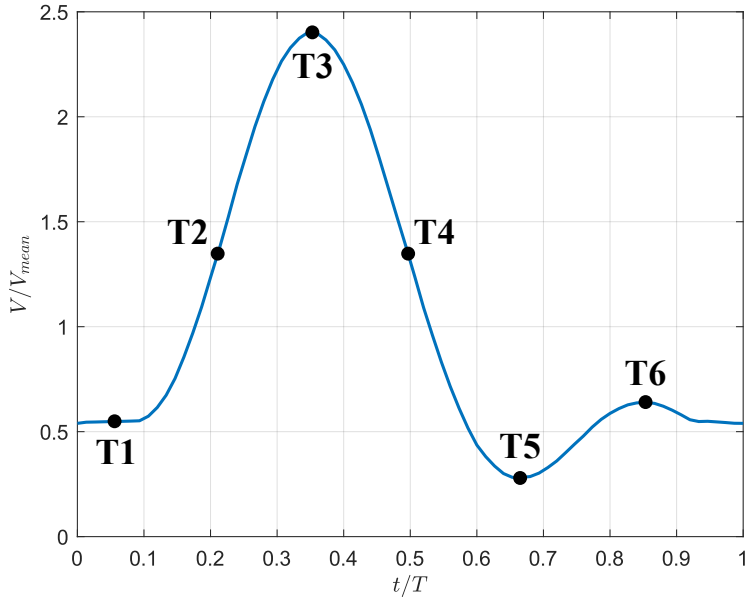

Figure 4.3: Inlet flow waveform.

The most commonly used outlet boundary condition for aortic flows is the outflow boundary condition as discussed in Section 1.3.5. This boundary condition imposes a zero-gradient pressure at the outlet and is usually utilized together with a built-in overall mass balance correction algorithm [54, 58, 63]. However, such an algorithm is not integrated into OpenFOAM, as a result, the outlet of the domain is extended by 5 diameters to obtain the desired zero gradient pressure at the original outlet location, and a zero pressure condition is applied to the extended outlet. The optimal level of outlet extension has been determined through a series of simulations, and an extension of 5 diameters is found to provide a fully developed pressure profile at the original outlet location. Notably, the extension of the outlet is not included in the

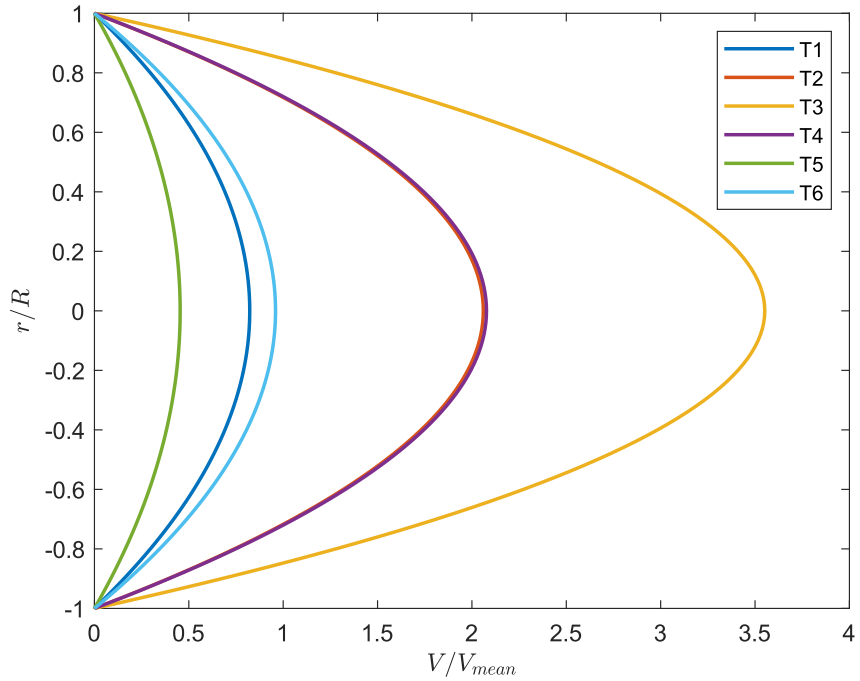

Figure 4.4: Parabolic velocity profiles at key time instants.

post-processing of data for the sake of simplicity.

In Chapter 3, four different grids were tested, and Grid 3 was deemed adequate for solving the problem at hand. For the present chapter, Grid 3 is used once again, since the only difference is the pulsatile inlet velocity for the 75% stenosis case. To ensure the suitability of the grid at the maximum flow instant ($t/T = 0.25$), two grid assessment parameters, LES_IQ and the ratio of the cell size to the Kolmogorov length scale (see Section 3.2), are employed in the 75% stenosis model since this model is expected to contain the highest turbulent activity. The minimum LES_IQ value is found to be 0.84 at peak systolic flow conditions (at the T3 instant) and the average LES_IQ value throughout the cycle is found to be 0.89. Thus, the grid is considered to be suitable for LES even under peak flow conditions. Additionally, the ratio of the cell size to the Kolmogorov length scale is evaluated and found to be 26, indicating that the used grid can produce reliable results. Finally, y^+ values are checked and they are found to be below one at all times.

OpenFOAM is utilized for the large eddy simulations together with WALE SGS model. Similar to Chapter 3, the pimpleFoam solver is used with the second-order im-

plicit backward scheme for time discretization and second-order Gaussian integration scheme as the gradient, laplacian and divergence schemes. A series of simulations are run to ensure time step independence, and an adaptive time step corresponding to a maximum CFL number of 1 is found sufficient. The non-Newtonian behavior of blood is modeled with the Carreau model as explained in Section 2.2. The resources of TRUBA HPC system of TÜBITAK ULAKBIM High Performance and Grid Computing Center are used for the solutions using 112 cores with Xeon 6258R 2.70GHz CPUs. The 0%, 50%, and 75% stenosis solutions for 12 flow cycles took 154, 170, and 178 wall clock hours, respectively.

The simulations are conducted over a total of twelve cycles, and the first two cycles are treated as initial transients and hence disregarded in the post-processing of data. As shown in Figure 4.5, the attainment of steady periodic flow conditions is established by monitoring the pressure and streamwise velocity fluctuations at $\theta = 35^{\circ}$ on the centerline, in proximity to the von Karman vortices. Reaching steady periodic conditions is checked for the 75% stenosis model since it is the most severe case. It is seen from the figures that the initial transients do not have high magnitudes and they disappear after the first two cycles. From this point on, only turbulent fluctuations are observed and the flow is considered to reach periodic conditions. The available computational resources and the large amount of data generated at each cycle impose a limitation on the total number of cycles that the simulation is run. By eliminating the initial two cycles, ten cycles remain for processing data and evaluating results, which is deemed sufficient, given that similar studies in the literature employed 8 [146] and 10 [147] cycles for post-processing purposes.

4.2 Results and Discussion

The data used for the results presented in this section are collected after the flow reaches steady periodic conditions for all solutions. Since the flow is pulsatile and periodic, ensemble averaging is mostly utilized as explained in Section 2.5. The results are non-dimensionalized using the mean inlet velocity $V_{mean} = 0.2$ m/s and inlet vessel diameter $D = 0.032$ m.

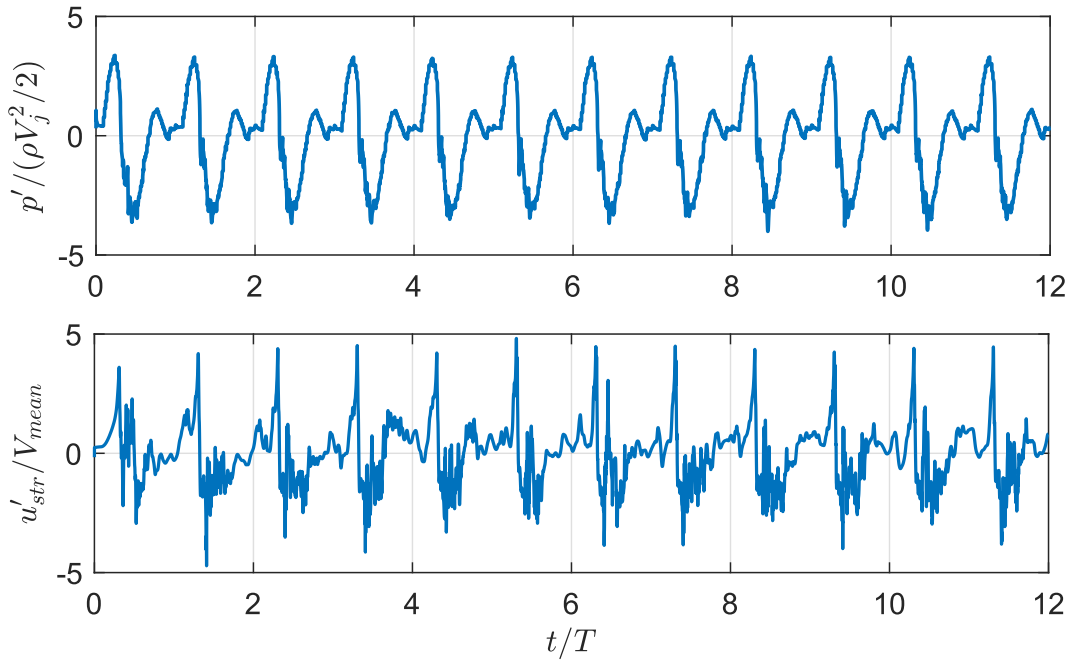

Figure 4.5: Temporal history of pressure (top) and streamwise velocity (bottom) fluctuations at $\theta = 35^\circ$ on the centerline for the 75% case.

4.2.1 Vortex Dynamics

Figure 4.6 shows snapshots of non-dimensionalized instantaneous vorticity on the frontal plane for all solutions at key time instants, after the simulations have reached steady-periodic conditions. It is apparent that the presence of a stenosis highly affects the flow field due to the jet formed at the beginning of the aortic arch. The 0% case shows weaker vortical activity at all time instants compared to the other two cases. The absence of strong vortices was expected for the 0% case since the only source of vortical activity are the secondary flow and pulsatility effects, which are less effective on the flow field compared to the effects of a stenosis. Unlike the mild (50%) and severe (75%) stenosis cases, the Dean vortices are more apparent at T1 and T2 instants in the unstenosed (0%) case and they die out at the T4 instant. The temporal behaviour of the 50 and 75% cases are similar in terms of flow structures. Weak vortices are observed at the T1 and T2 instants, the jet is formed and vortex shedding starts at the T3 instant, high vortical activity is seen at the T4 and T5 instants, and the vortices start to die out at the T6 instant. The intensity of the vorticity, however, is markedly different. For the 75% case, the flow jet can be observed even at the T1 and T2

instants where no apparent jet is yet formed at the 50% stenosis model. At the T4 and T5 instants, it is seen in the 75% case that the aortic arch region is mostly dominated by vortical structures, up to around $\theta = 100°$. On the other hand, the vortex structures in the mild stenosis case do not propagate downstream as much as they do in the severe stenosis case, only affecting the flow field up to around $\theta = 50°$. It can also be inferred from Figure 4.6 that the severity of the stenosis affects the location where vortex shedding starts to occur. This location has significance in terms of acoustics since the break frequencies were found to be evident close to vortex shedding regions in Chapter 3. For the 50% case, it is seen that the vortices appear near $\theta = 20°$, but they are more apparent near $\theta = 30°$ at the 75% case.

Figures 3.7 and 4.6 can be investigated together for the 75% case to compare the results of steady and pulsatile flow simulations. The T4 instant is the instant that has the most resemblance to the steady flow results, which is expected since the T4 instant is also the closest instant to the mean flow conditions and the steady flow simulation utilized the mean flow parameters. It can be concluded by the comparison of two figures that examining only the mean flow condition can produce useful results in terms of vorticity since the highest vortical activity is observed at the T4 instant, not at the peak systolic instant (T3). It will later be shown in Section 4.2.3 that the highest pressure fluctuations also occur close to the T4 instant, further supporting the suitability of steady flow analysis if the temporal effects have minor importance.

4.2.2 Turbulent Kinetic Energy

As stated in Chapter 3, the flow investigated in this study lies in the transitional region, therefore, turbulent characteristics of the flow are examined in this section. Figure 4.7 shows the ensemble-averaged non-dimensionalized turbulent kinetic energy (TKE) on the frontal plane, and additionally, on the cross-sectional planes of $\theta = 35°$, $55°$, $75°$, $90°$. It is possible to associate Figure 4.7 with Figure 4.6 since high TKE regions coincide with the strong vortical activity regions. As in Figure 4.6, the unstenosed case does not show any considerable turbulent activity throughout the cycle and the flow is mostly laminar. Only low TKE regions are observed around $\theta = 55°$ at the T1 instant due to Dean vortices, and downstream of $\theta = 90°$ at the other time

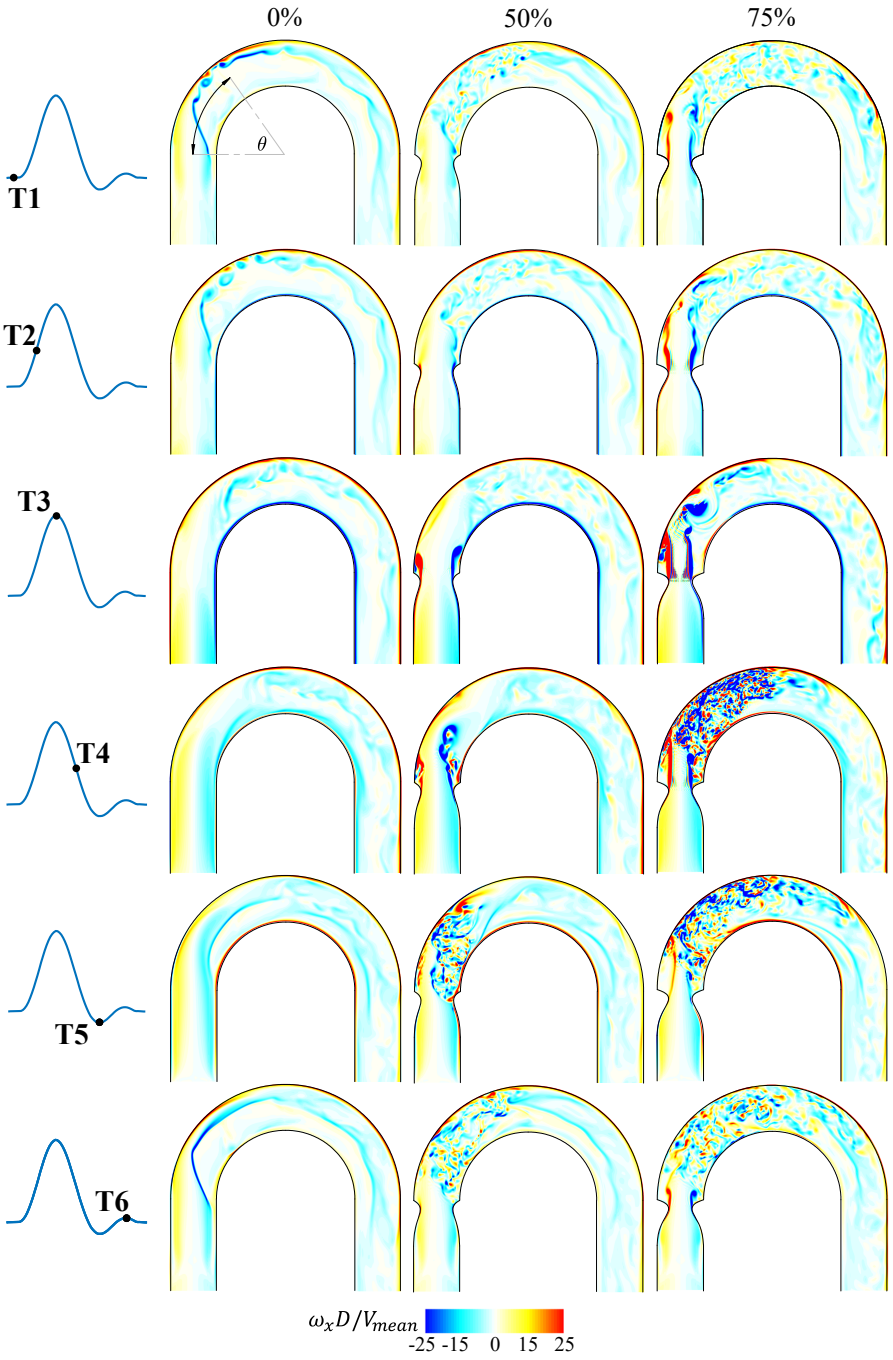

Figure 4.6: Non-dimensional vorticity distribution on the frontal plane at key time instants.

instants due to the effects of secondary flow. When the mild and severe stenosis cases are compared, it can be seen that the TKE is significantly less intense in the 50% case. The flow is mostly laminar after $\theta = 90°$ at all time instants for the mild stenosis, whereas turbulent activity is observed throughout the aortic arch even at

T1 in the severe stenosis case. The vortex shedding regions observed in Figure 4.6 are associated with transition to turbulence, which can also be observed in Figure 4.7 at the T3 instant for 75% case and at the T4 instant for 50% case. Additionally, transition to turbulence is delayed in the 50% case, occuring after the T4 instant. In the 75% case, the transition starts at the peak systolic instant (T3) and the flow is highly turbulent in the aortic arch until around T5, then the turbulent structures finally die out towards the T1 instant.

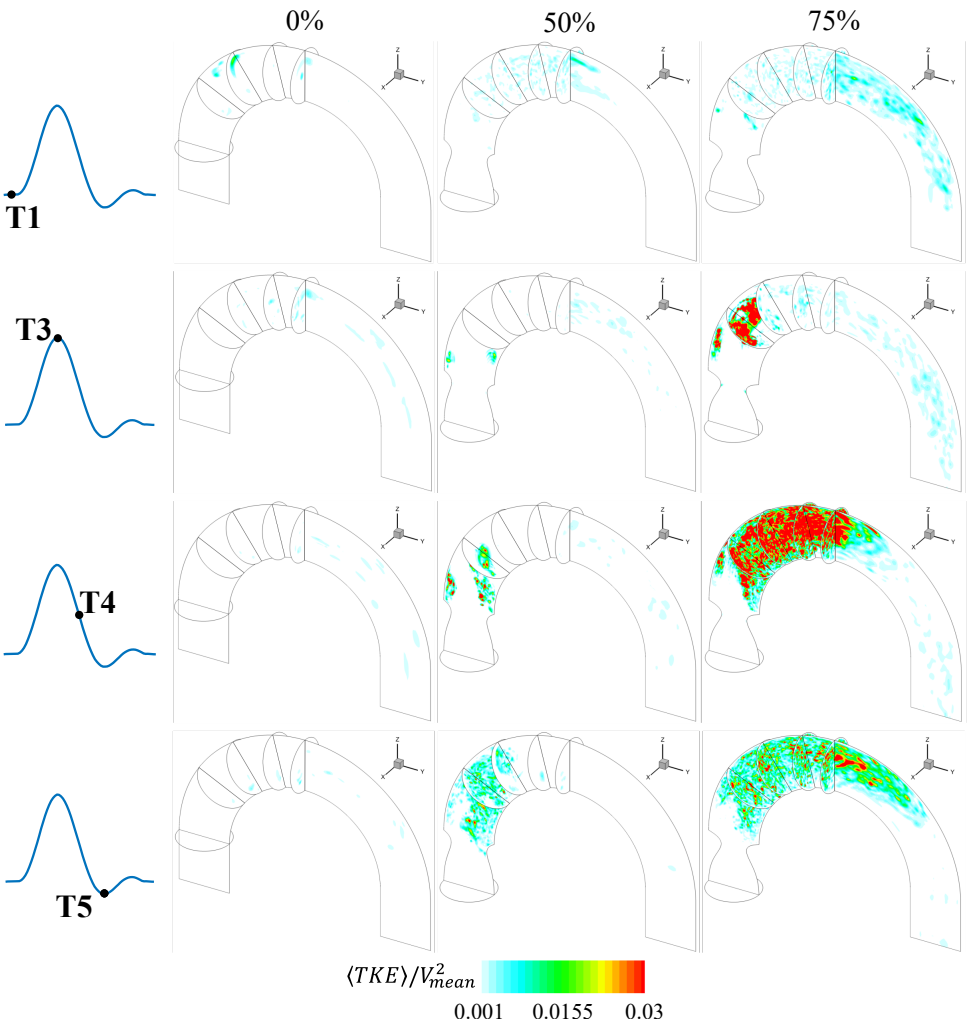

Figure 4.7: Non-dimensionalized ensemble-averaged turbulent kinetic energy on the frontal plane and at $\theta = 35°, 55°, 75°, 90°$ planes.

4.2.3 Wall Pressure Analysis

As discussed in Chapter 3, wall pressure fluctuations are a crucial factor in the generation of heart murmurs, making them an essential part of hemoacoustic analyses. Therefore, this section focuses on presenting and discussing the pressure values and their fluctuations on the anterior surface of the aortic arch.

Figure 4.8 shows the non-dimensionalized ensemble-averaged pressure on the anterior surface at the peak flow instant. The effect of stenosis severity on the pressure change across the aortic arch can clearly be seen in the figure, since the 0% case experiences a slight change in pressure and the other two cases exhibit higher changes in pressure. The pressure difference in the 0% case is solely due to major losses, which are observed to be negligible compared to the pressure variation resulted by the presence of a stenosis. It is also seen from the figure that the pressure change across the aortic arch in the 75% case is approximately double the change of the 50% case, and these two cases exhibit a fluctuation in pressure unlike the unstenosed case. The lowest pressure occurred near $\theta = 10^{\circ}$ in the 50% case and near $\theta = 35^{\circ}$ in the 75% case. Notably, the 50% case closely resembles the unstenosed case after $\theta = 30^{\circ}$, whereas the 75% solution remains close to the unstenosed case after $\theta = 100^{\circ}$, once again implying a wider region affected by the severe stenosis.

Wall pressure fluctuations were found to be the key factor in generation of heart murmurs in Chapter 3, therefore they are shown in more detail in Figures 4.9 to 4.11. Figure 4.9 illustrates non-dimensionalized wall pressure fluctuations on the anterior surface for all three solutions as a function of both space and time. The double prime notation is utilized in the figure, therefore the figure focuses on turbulent fluctuations rather than fluctuations associated with the pulsatility of the flow. It is seen that as stenosis severity increases, the level of fluctuations also increases as expected. In the unstenosed case, low-magnitude fluctuations are present and are observed around $\theta = 140^{\circ}$ between T2 and T3 instants. After this point, the level of fluctuations decreases, indicating that the diastole phase experiences fewer fluctuations. Unlike the other two cases, in the 0% case, fluctuations are observed further downstream, as there is no stenosis at the start of the aortic arch, and fluctuations arise from secondary flow effects, which are minimal compared to the effects of stenoses. In both

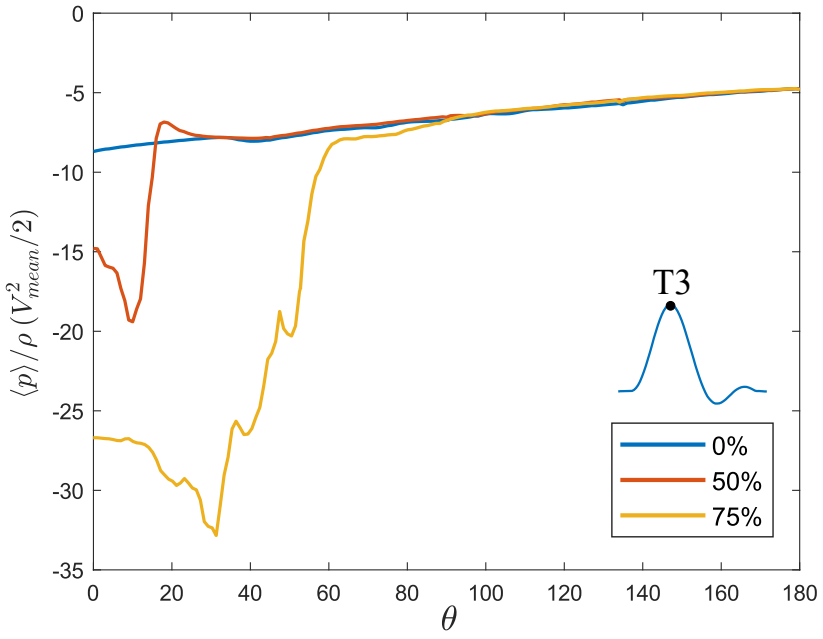

Figure 4.8: Non-dimensionalized ensemble-averaged wall pressure at the anterior surface at the peak flow instant.

the 50 and 75% cases, fluctuations occur after the peak systolic instant and most of the significant fluctuations are observed at the decelerating flow phase between the T3 and T5 instants. The maximum value of wall pressure fluctuations in the 75% case is approximately four times larger than the 50% case, and these fluctuations are observed at a much wider region in the 75% case. The peak points in the surface plots are determined and it is seen that the maximum occurs at $\theta = 65°$ and at $t/T = 0.47$ for the 75% case. The 50% case reaches its maximum at $\theta = 25°$ and at $t/T = 0.56$. It can be inferred from the figure that the presence of a mild stenosis affects only a particular area and at a short period of the cardiac cycle. Conversely, the 75% case demonstrates that severe stenosis significantly affects the post-stenotic flow field throughout the cardiac cycle. The areas with low pressure fluctuations in the 50 and 75% cases are similar in magnitude and patterns compared to the unstenosed case, indicating that these regions are dominated by secondary flows and the effects of the stenosis are not considerable.

In order to better understand the plots in Figure 4.9, the pressure fluctuations on the anterior surface are depicted at T3 and T4 instants in Figure 4.10. Note that the

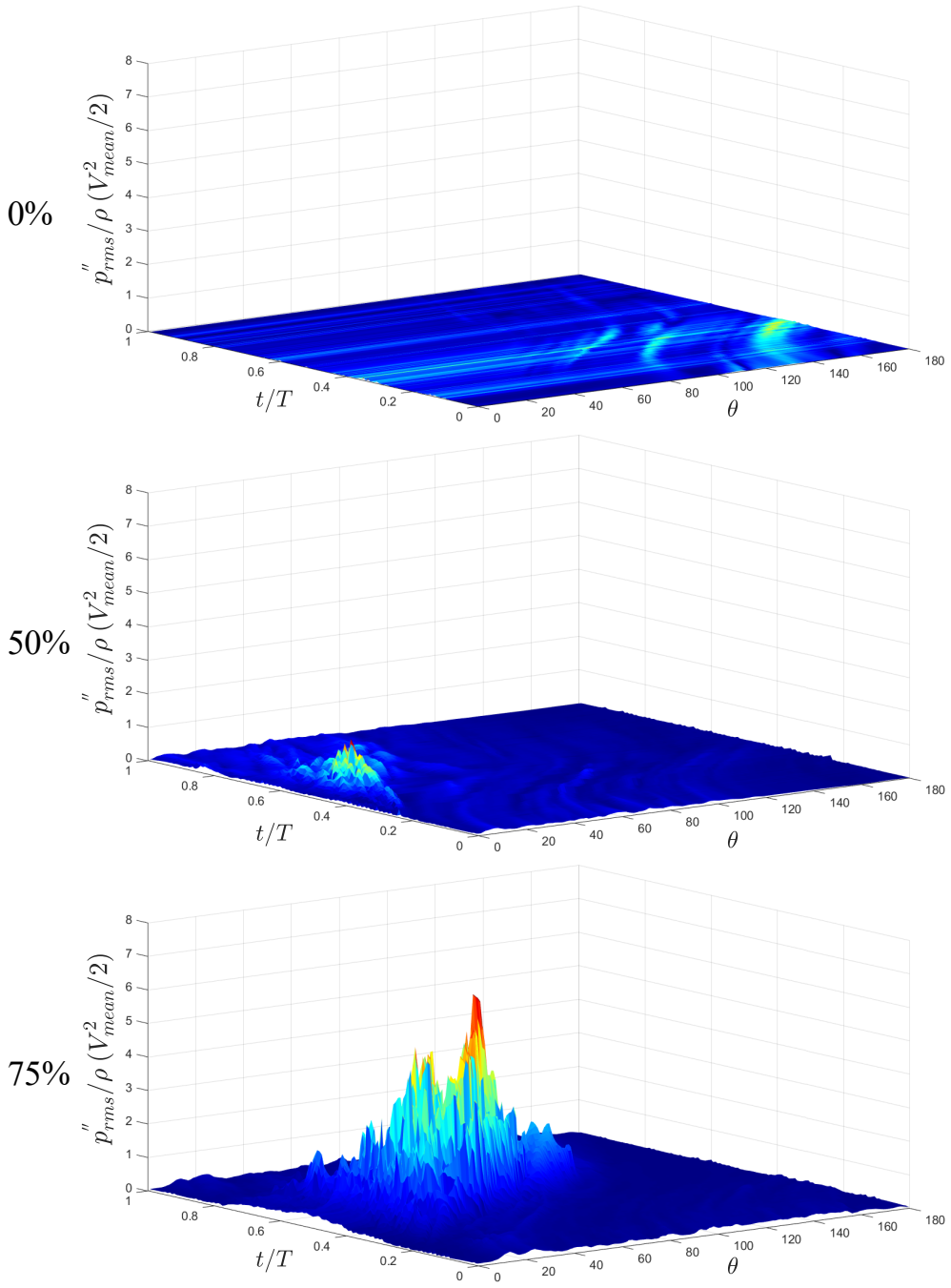

Figure 4.9: Non-dimensionalized wall pressure fluctuations at the anterior surface.

plots in Figure 4.10 are cross-sections of the surface plots in Figure 4.9. The 0% line is almost invisible in both T3 and T4 instants since there are no considerable fluctuations. At the T3 instant, high-magnitude fluctuations are observed in the 75% case, however, the flow is still quiet and only low-magnitude fluctuations are observed in the 50% case. The effect of the 50% stenosis becomes more evident in the T4

instant as it was also observed in Figures 4.6 and 4.7. It is observed that the maximum fluctuation point in the 75% case is near $\theta = 55°$ at the T3 instant and near $\theta = 80°$ at the T4 instant. It is also known from Figure 4.9 that the maximum occurs slightly earlier than the T4 instant and at $\theta = 65°$, indicating that the location associated with the generation of murmurs is highly time-dependent and rapidly changes throughout the cardiac cycle. The location of maximum pressure fluctuations on the anterior surface was found to be near $\theta = 60°$ in the steady flow analysis in Chapter 3. This finding is close to the results of the pulsatile study, implying that the pulsatility of the flow does not significantly affect the source location of the murmurs.

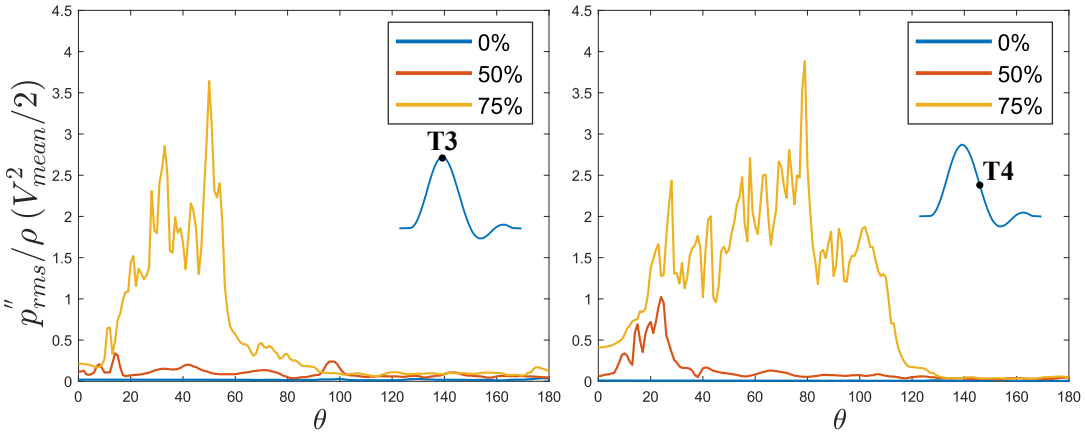

Figure 4.10: Non-dimensionalized wall pressure fluctuations at the anterior surface at flow instants T3 and T4.

The temporal variation of wall pressure fluctuations at $\theta = 35°$ on the anterior surface is shown in Figure 4.11. This location is in the region where vortex shedding occurs and high magnitude fluctuations occur in both the 50 and 75% cases. The figure clearly demonstrates that the pressure fluctuations of the 75% case reach their maximum around $t/T = 0.45$, which corresponds to the decelerating flow phase close to the T4 instant. The 50% case, however, shows higher fluctuation levels toward the end of the cycle, around $t/T = 0.65$. The unstenosed case shows almost no fluctuations in the entire cycle.

Figure 4.12 shows the time history of wall pressure at $\theta = 35°$ of the 75% case. This data is converted into sound by the `soundsc` command in MATLAB, together with several other locations of all three solutions. The generated sounds are similar to what is heard by clinical auscultation methods, however in real life applications, these

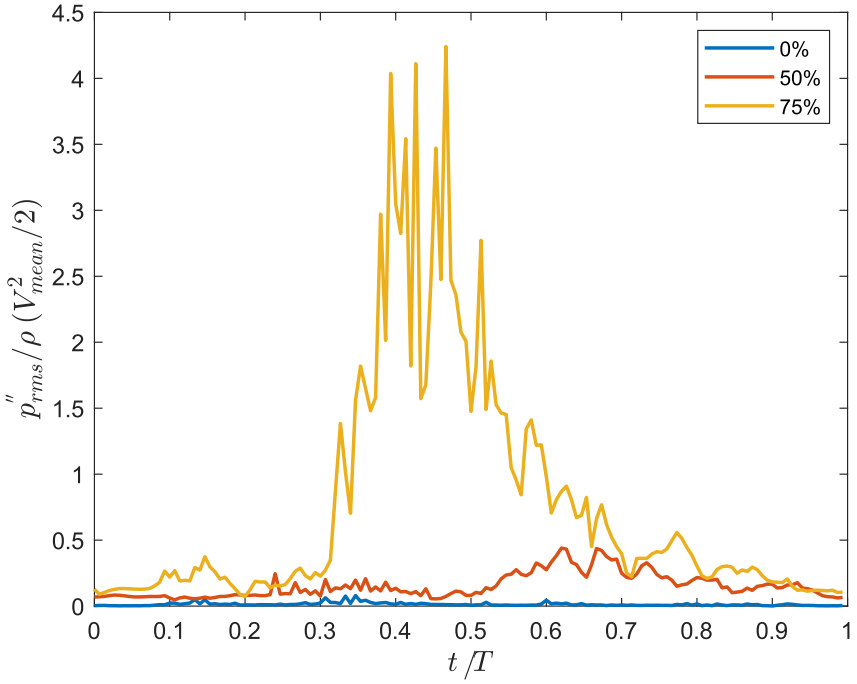

Figure 4.11: Non-dimensionalized wall pressure fluctuations at the anterior surface at $\theta = 35°$.

sounds are weakened since they are transmitted through human tissue before reaching the auscultation device. CFD generated sounds can still be useful for electronic auscultation devices mentioned in Section 1.3.7. These devices determine stenosis severity from the sound obtained from patients. The principle used in these devices is a machine learning algorithm that needs to be trained by sound data from different stenoses. CFD is an important tool for developing such auscultation-based diagnosis devices since different geometric models and stenosis severities can be employed to generate sound data for the training of these devices.

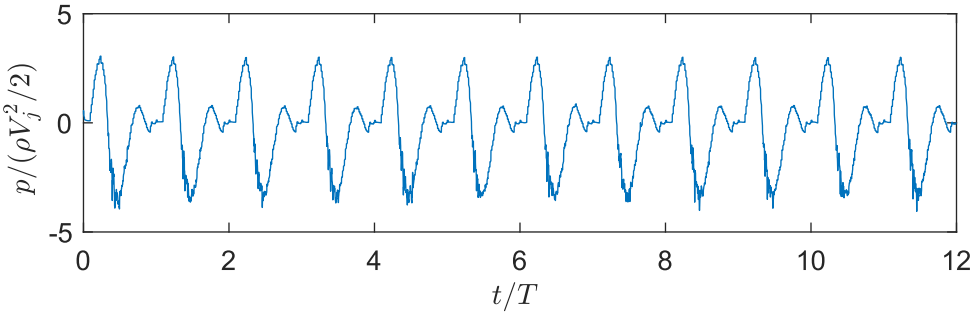

Figure 4.12: Non-dimensionalized wall pressure at the anterior surface at $\theta = 35°$ in the 75% case.

4.2.4 Break Frequency Analysis

As mentioned earlier, one of the main motivations of this study is to determine the break frequencies, which correspond to the distinct frequency at which the energy of pressure fluctuations turns into noise [148]. With this purpose, the spectra of pressure fluctuations plotted at selected θ planes on the centerline are plotted in Figures 4.13 - 4.15. The spectrum of pressure fluctuations (E_p) is defined as $\langle p^{''} \rangle / (\rho V_{mean}^2)/2$ and the Strouhal number of pulsating flow (St_p) is non-dimensionalized by the inlet diameter and mean inlet velocity as fD/V_{mean}. Figure 4.13 shows energy spectrum of the 0% case at $\theta = 35^{\circ}$. This location is chosen since it was found to be associated with the periodic vortex shedding in Chapter 3. It is observed that the fluctuations are approximately on the same level at all frequencies, indicating that the transition to turbulence has not occurred in this location. Although not shown in the figure, the spectrum at other locations are also investigated in the aortic arch, but none of the locations demonstrated signs of turbulence and a slope change. Therefore, the break frequency cannot be evaluated for the 0% case. This finding can also be supported by examining Figure 4.7 since there is no turbulent activity in the 0% solution. The absence of a break frequency for the unstenosed model makes sense since the stenoses are known to produce murmurs at distinct frequencies, therefore healthy and stenotic patients can be differentiated by means of auscultation based diagnosis methods.

Figure 4.14 shows the spectrum of pressure fluctuations for the 50% case at $\theta = 20^{\circ}$. This location is chosen by evaluating several locations and picking the plot with the most obvious slope change. The maximum wall pressure fluctuations were also observed near $\theta = 20^{\circ}$ in Figure 4.9, therefore detecting the maximum slope change in this location is not a coincidence. It can be seen from Figure 4.14 that a slope change occurs near St_p = 7.3, identified as the break frequency of the mild stenosis. In order to determine the slope change, piecewise least-squares-based linear curve fitting is performed and the intersection of the two linear regression lines gives the Strouhal number associated with the break frequency of the flow. The magnitude of the spectrum at the break frequency is near 3×10^{-3}, which was around 3×10^{-4} in the unstenosed case, meaning that much stronger murmurs are heard at the break frequency. This way, the presence of a stenosis can be identified by auscultation

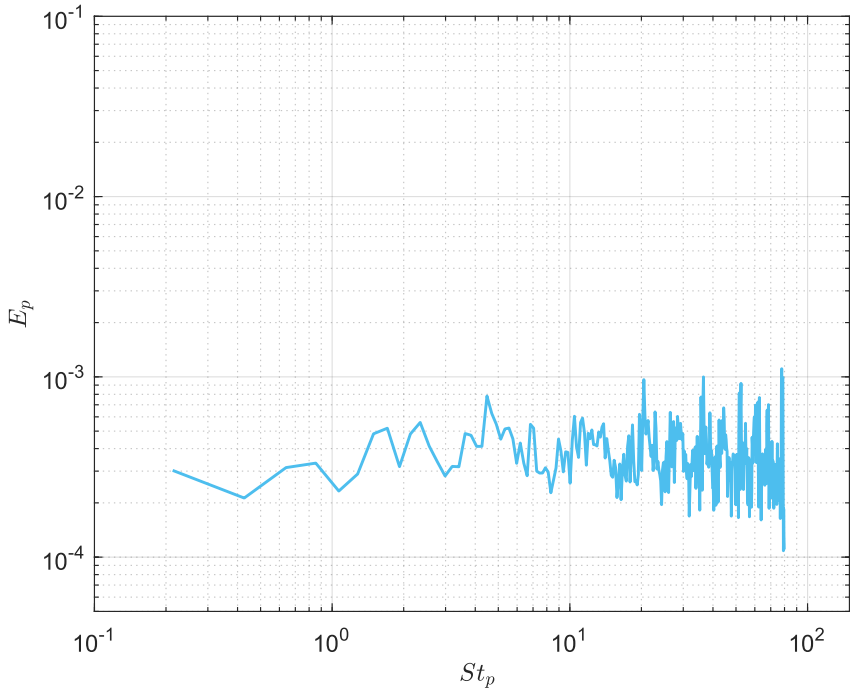

Figure 4.13: Spectra of pressure fluctuation of the 0% stenosis model plotted at $\theta = 30^{\circ}$ at the centerline.

methods.

Figure 4.15 shows the spectrum of pressure fluctuations for the 75% case. The break frequency is evaluated at St_p = 10.3 and the change in slope is sharper compared to the 50% case. The level of of the spectrum at the break frequency is near 10^{-2}, markedly higher than the mild and unstenosed cases, indicating that the intensity of the sound emitted from the severe stenosis has higher amplitude and more detectable signals. Comparing the 50 and 75% cases, it is seen that the Strouhal number at the break frequency is higher in the 75% case. The increase in break frequency with increasing stenosis severity is also reported in previous studies [145, 149, 150].

The break frequency is an important metric in auscultation based diagnosis methods since it helps determine patients' stenosis severities. However, the evaluated break frequency by using CFD can be affected by the parameters that are used in the numerical solution. Therefore, the effects of several simulation parameters are investigated using the 75% stenosis model and the results are shown in Table 4.1. Solution 1 is the 75% case explained in this chapter, and it can be considered as a datum for

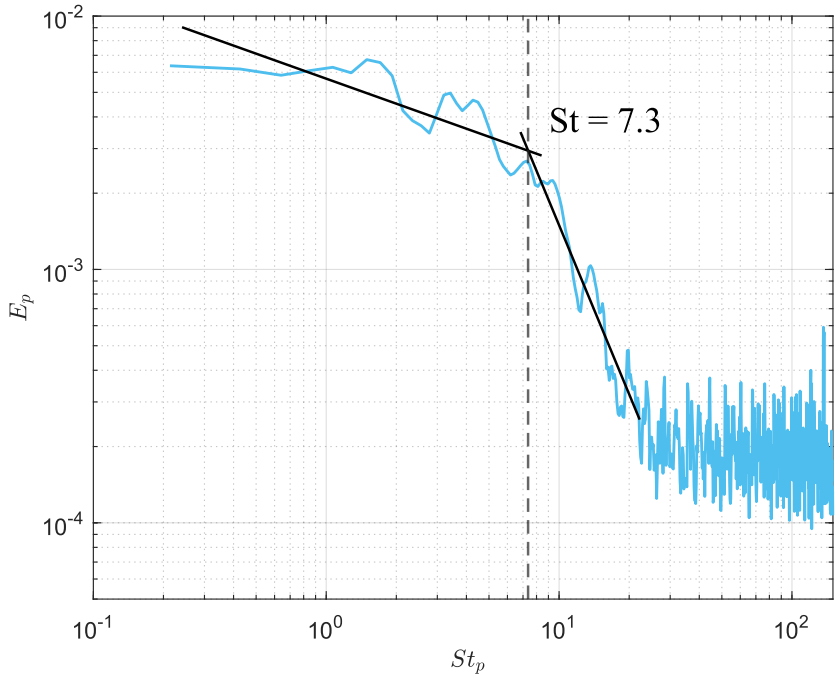

Figure 4.14: Spectra of pressure fluctuation of the 50% stenosis model plotted at $\theta = 20°$ at the centerline.

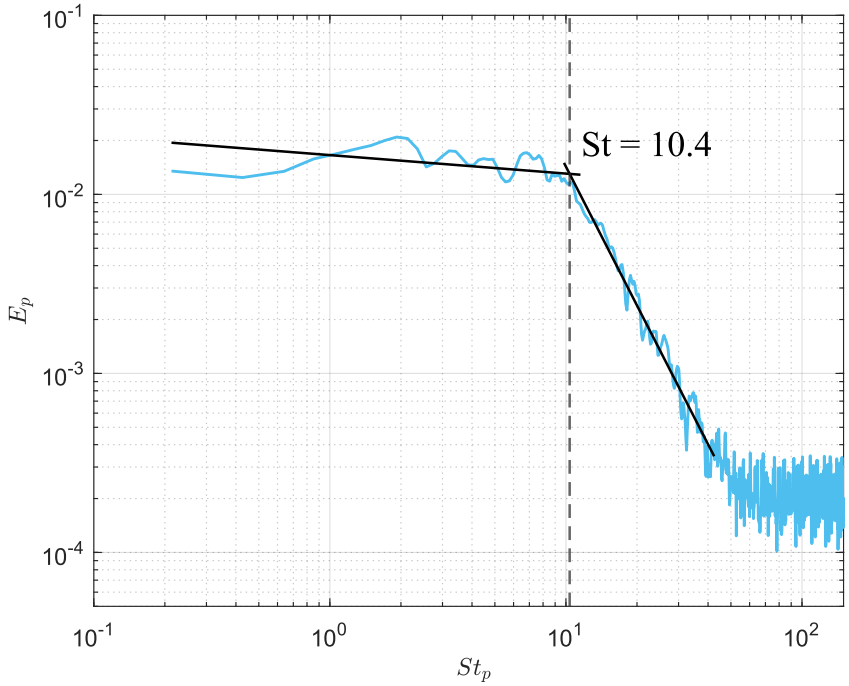

Figure 4.15: Spectra of pressure fluctuation of the 75% stenosis model plotted at $\theta = 30°$ at the centerline.

comparison of CFD parameters. Solution 2 utilizes Grid 2 (see Section 3.2) to see how the break frequency is affected by the computational grid. Solution 3 uses a CFL number of 0.5 to understand the effects of the time step size used in the analysis. Solution 4 imposes a simple sinusoidally pulsating velocity waveform mapped into a parabolic profile to check the effects of inlet velocity waveform. Finally, Solution 5 is the analysis explained in Chapter 3 using constant flat velocity profile, added to this comparison to examine the effect of flow pulsatility on the break frequency.

Table 4.1: Effect of simulation parameters on the break frequency (75% case).

Solution	Inlet Waveform	Number of Cells	CFL Number	Break Frequency
1	Physiological	3300780	1	65 Hz
2	Physiological	1450416	1	48 Hz
3	Physiological	3300780	0.5	65 Hz
4	Sinusoidal	3300780	1	60 Hz
5	Steady	3300780	1	50 Hz

Comparing Solutions 1 and 2, it is seen that a break frequency of 48 Hz is obtained with the coarse grid, corresponding to a difference of 26% with the base solution (Solution 1). By using a coarse grid, computational expenses are lowered but the break frequency is evaluated with an error that is not acceptable. Therefore, using coarse grids is not recommended for break frequency analyses.

Solutions 1 and 3 are examined together to see if the threshold of CFL = 1 is enough for hemoacoustic analyses and it is seen that the two solutions produced exactly the same break frequency. Therefore, using a CFL number of 1 is suitable for such simulations and it is not worth the effort to use more computational resources to use a lower CFL number. However, it is worth mentioning that higher frequencies and lower magnitude fluctuations can be captured in Solution 3. If one is interested in lower levels of the pressure spectrum, decreasing the CFL number is proved to be useful.

In many clinical CFD studies, the availability of actual velocity data may be lacking. To test such a case, Solution 4 uses a simple sinusoidal waveform mapped into a parabolic velocity profile to examine the differences originating from the inlet velocity waveform. The used sinusoidal profile has the same mean Reynolds number of 2000 as in Solution 1, and the maximum Reynolds number is 4500. It is seen that the

break frequency is predicted with a 7.7% difference compared to Solution 1, suggesting that a simple sinusoidally pulsating waveform can also be useful if real flowrate values are absent.

Lastly, Solutions 1 and 5 provide a comparison of realistic and contant inlet velocity boundary conditions. The realistic condition in Solution 1 is the physiologically pulsating waveform with a parabolic velocity profile, and the simple condition in Solution 5 is the constant flowrate with flat velocity profile. It is seen from Table 4.1 that the break frequencies evaluated by these two solutions and a 23% difference is observed. Although using simple conditions proved useful to capture the source location of murmurs, wall pressure fluctuations and turbulence in the post-stenotic flow field, the break frequency cannot be correctly predicted. This observation implies that the pulsatility of the flow has an impact on the break frequency and should be included in the CFD simulations if enough computational resources are available.

4.2.5 Acoustic Pressure

The sound generated at the vessel walls are evaluated in terms of acoustic pressure in this section. The pressure data collected along the aortic arch on the anterior surface is post-processed by performing Fast Fourier Transform with Hanning window filtering to obtain the plots in Figure 4.16. The pressure data used is collected at 2000 Hz after the simulations reached steady periodic conditions. The sampling frequency is determined based on several trial and errors, and it is seen the most acoustical activity is happening within the frequency range of 0 - 300 Hz. The used sampling frequency of 2000 Hz enables to capture a frequency level up to 1000 Hz, therefore considered adequate. The pressure values are converted to acoustic pressure values as:

$$p\,(\text{dB}) = 20 \log_{10} \left(\frac{p\,(\text{dB})}{p_{ref}\,(\text{Pa})} \right) \tag{4.3}$$

where p (Pa) is the pressure value obtained in the simulations, p (dB) is the acoustic pressure, and p (Ref) is the reference pressure, which is taken as 2×10^{-5} Pa, since this value is the human ear hearing threshold.

Figure 4.16 shows the variation of acoustic pressure along the aortic arch on the an-

terior surface together with the frequency content. There are several dense acoustic pressure regions seen as horizontal lines. These horizontal lines are almost the same for all three cases, therefore they are associated with the pulsatility of the flow and the secondary flow effects. In this study, the acoustic pressure content resulting from the turbulent fluctuations due to the presence of a stenosis has higher importance. In the 0% case, no acoustic pressure due to turbulent fluctuations is observed, since there is no stenosis and the flow remains mostly laminar. The 50% case has low magnitude acoustic pressure content around $\theta = 20°$, but they are mostly dominated by the horizontal lines. The contours are similar to the unstenosed case, indicating that the sound emitted from the mild stenosis has low intensity and therefore might be hard to detect by auscultation. The acoustic pressure content due to the effects of the stenosis is most clearly seen in the 75% case. The acoustic activity is observed approximately between $\theta = 15°$ and $\theta = 80°$, and the maximum intensity is found near $\theta = 65°$. This result is in line with the pressure fluctuations observed in Figure 4.9.

4.3 Conclusion

The stenosis severity is a clinically important parameter since it is used for both diagnosis and treatment. Specifically, the auscultation based diagnosis methods aim to determine the severity based on sound signals. Therefore, this section was devoted to investigate the effects of stenosis severity on the flow field and the sound emitted from the stenosed vessel. 0% (unstenosed), 50% (mild), and 75% (severe) stenosis models are used for the simulations with physiologically pulsating inlet velocity conditions. The analyses of vorticity and turbulent kinetic energy revealed that the unstenosed case did not experience transition to turbulence and the flow is mostly laminar throughout the domain, with only small disturbances due to secondary flow effects. The 50% case showed a clear difference compared to the unstenosed case and transition to turbulence is observed in the post stenotic region. The turbulence effects did not propagate further than the mid aortic arch region. The 75% case showed the highest turbulent activity in the aortic arch and significantly deviated from the 50% case in terms of flow fields. Similarly, wall pressure analyses resulted in almost no pressure fluctuations for the 0% case, low magnitude fluctuations for the 50% case,

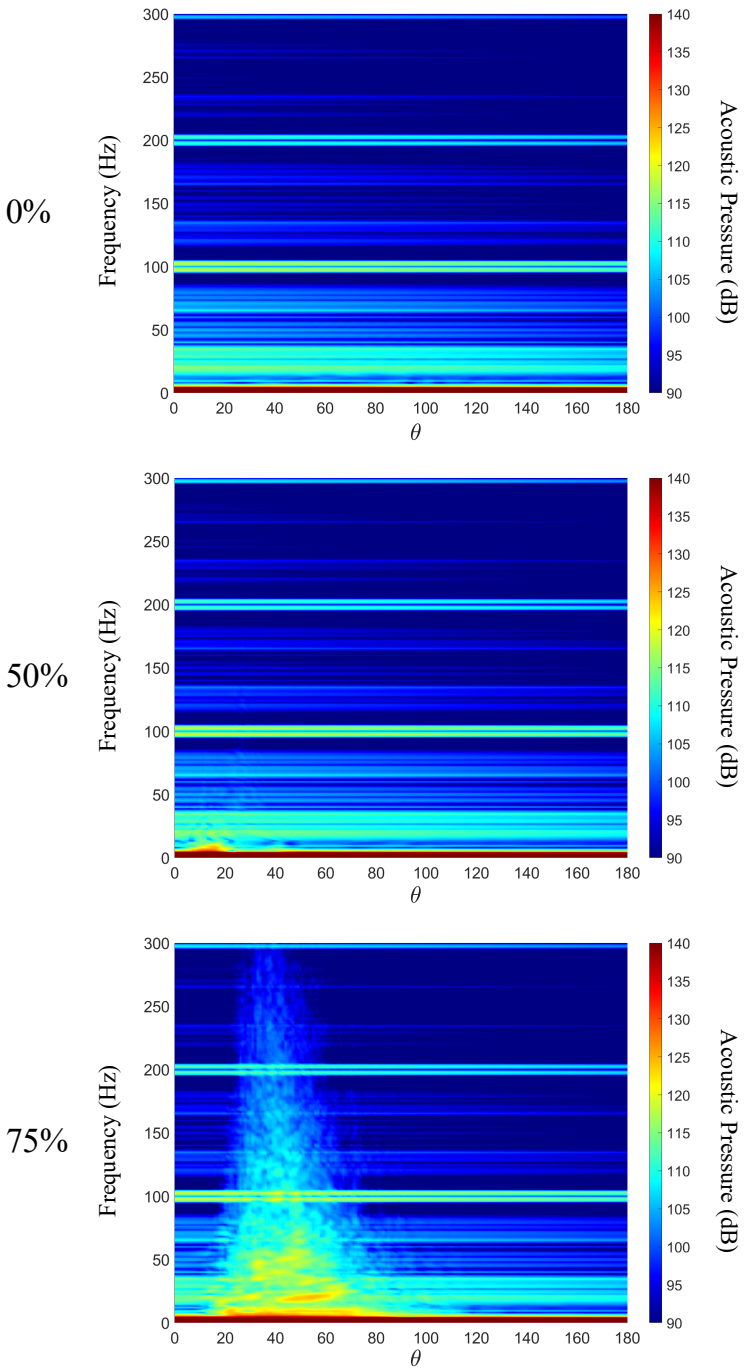

Figure 4.16: Acoustic pressure content on the anterior surface along the aortic arch.

and high magnitude fluctuations for the 75% case. For all three cases, the break frequencies are also evaluated and a break frequency could not be obtained for the 0% case. Break frequencies of 50 and 75% cases are found as 7.3 and 10.3, respectively. The intensity of the sound emitted from the vessel is also found to be positively cor-

related with stenosis severity. Finally, several numerical analyses are performed to test the effects of simulation parameters on the evaluated break frequency. It is seen that using a CFL number of 1 yields similar results as using a CFL number of 0.5. Furthermore, it is found that using a simple sinusoidal velocity waveform generates comparable results with a more realistic physiologically pulsating velovity waveform. Using a steady inlet condition, however, leads to deviated break frequency values from the realistic boundary condition case.

CHAPTER 5

CONCLUSION AND FUTURE WORK

In this chapter, the study is summarized and conclusions are explained together with the limitations of the study. The aspects in which the current study can be further extended are also discussed.

5.1 Conclusion

Aortic stenosis is a valvular disease that can lead to serious consequences if not treated. There are several methods for the diagnosis of aortic stenosis, but most of them are invasive methods. One of the non-invasive methods is auscultation, where the heart murmurs are listened by means of a stethoscope or an electronic device. Auscultation-based electronic devices correlate the sounds emitted from the vessel with the severity of the stenosis, and these devices are trained using the sound data obtained from different patients. CFD is a promising tool for generating sound signals from computer models to train such diagnosis devices. In this thesis, it is aimed to investigate the sounds emitted from different stenosis models and to evaluate several simulation methods to obtain the best results with reasonable computational resources.

In the current study, large eddy simulations with the WALE subgrid scale model are utilized to investigate the flow fields of aortic stenosis models. Chapter 3 is devoted to prove the suitability of this method for aortic hemodynamics analyses. For this purpose, the DNS study of Mittal et al. [16] is considered as a reference solution and the problem is solved by using LES. Firstly, 4 different grids are employed to evaluate the suitability of the computational mesh. A grid with 3300780 cells is chosen to be

the best alternative among the four grids. The chosen grid has an LES_IQ value of 0.89 and the ratio of cell size to Kolmogorov length scale is 24. Using this grid, the results are compared with the reference study and a good agreement between the LES and DNS solutions is observed in all flow fields. Two important outcomes of the DNS study were the location of the maximum surface pressure fluctuations and the break frequency of the sound emitted from the vessel. These parameters are predicted by the LES solution with errors of 9% and 6%, respectively. Considering that the DNS solution requires more than 5 times the computational resources of the LES study, the differences are deemed tolerable and it is concluded that LES can be a useful tool in hemodynamic CFD simulations.

In Chapter 4, stenosis severities of 0% (unstenosed), 50% (mild stenosis), and 75% (severe stenosis) are investigated under physiologically pulsating conditions. It is found that the flow in the unstenosed model is predominantly laminar throughout the domain and the only disturbances occur due to the effects of the secondary flows. The 50% case showed some turbulent activity at the post-stenotic region, but the effects are limited to a certain region of the flow field (up to $\theta = 50^{\circ}$) and a certain period in the flow cycle (between T3 and T4 instants). The turbulent activity observed in the 75% case is the highest among all three cases as expected since it is the severest constriction. The effects of the stenosis are observed in almost everywhere in the aortic arch region, and the flow disturbances were present throughout the full flow cycle. Similar to the turbulence effects, the intensity of the sound emitted from the vessels is also found to be increasing with increasing stenosis severity. The pressure spectra showed that the sound intensity of the 50% case is approximately 10 times larger than the unstenosed case, and the intensity in the 75% case is around 30 times larger compared to the unstenosed case. The break frequencies of the three cases are also evaluated and it is seen that no break frequency can be observed for the 0% case since there is no stenosis in the domain. The break frequencies of 50 and 75% cases are found to be 7.3 and 10.4, respectively. Finally, several simulations are run to see the effects solution parameters on the evaluation of the break frequency. It is concluded that using a coarse mesh or steady inflow conditions result in an error of around 25% compared to a solution with a fine grid and physiologically pulsating inlet conditions. The effect of time step size is also examined and it is found that

using a CFL number of 1 is adequate.

This thesis is written with the hope of contributing the development of ausculation-based diagnosis devices and examining the CFD parameters used in the simulations to help others obtain the most accurate results. In addition, the capabilities of LES and the WALE subgrid scale model are shown for hemodynamic analyses.

5.2 Limitations

The problem solved in this thesis involve several simplifications. The first one is the used geometric model, which is highly simplified compared to a real aorta model. However, the geometry of the aorta is highly dependent on the patient, therefore using a simplified model might be helpful for evaluating general outcomes. The exclusion of the upper branches is also a significant assumption, but this assumption is used in the literature when the patient-specific geometry is not available [47, 61, 16]. Another assumption is the rigid wall boundary condition, which is widely used in the literature as explained in Section 1.3.5. Finally, the opening and closing of the valve leaflets are not included in the study and the aortic valve is treated to be stationary throughout the cardiac cycle. This simplification is firstly utilized due to the difficulties in simulating the movement of the valve leaflets, and secondly, the valve leaflets are stiffened in aortic stenosis patients and their movement is constricted. Although the used model is stationary and cannot account for the valve leaflet movements, it represents aortic atherosclerosis and supravalvular aortic stenosis geometries, a condition in which the narrowing occurs right above the aortic valve.

5.3 Future Work

There are two major aspects that the current work can be developed. The first one is modeling the damping of the sound waves due to the surrounding tissues. The obtained sound data is directly collected from the vessel walls, where in real life, the sound waves travel through human tissue before reaching the auscultation device. This way, more realistic sound data can be generated to be used in the training of

diagnosis devices. Secondly, the simulations can be run on patient-specific models. This way, more realistic sound waves can be obtained. Additionally, more clinically useful simulations can be utilized using patient-specific models, such as virtual aortic valve replacement operations, in which the aortic valve is replaced virtually on the gemoetric model and the outcomes are examined by means of CFD simulations. This method gives an idea to medical professionals on the selection of the treatment procedure before the operation is actually performed on the patient.

REFERENCES

[1] L. S. Lilly, *Braunwald's Heart Disease Review and Assessment E-Book*. Elsevier Health Sciences, 2012.

[2] S. A. Khonsary, "Guyton and hall: textbook of medical physiology," *Surgical neurology international*, vol. 8, 2017.

[3] J. W. Hurst and V. Fuster, *Hurst's the heart, arteries and veins*, vol. 1. McGraw-Hill Companies, 1998.

[4] "Aortic valve." `https://en.wikipedia.org/wiki/Aortic_valve`. Accessed: 2022-01-15.

[5] G. J. Tortora, *Principles of human anatomy*, pp. 341, 367, 369. Harper Collins College, seventh ed., 1995.

[6] H. Boudoulas and C. Stefanadis, *The aorta: structure, function, dysfunction and diseases*. Informa Healthcare, 2009.

[7] A. Wolak, H. Gransar, L. E. Thomson, J. D. Friedman, R. Hachamovitch, A. Gutstein, L. J. Shaw, D. Polk, N. D. Wong, R. Saouaf, *et al.*, "Aortic size assessment by noncontrast cardiac computed tomography: normal limits by age, gender, and body surface area," *JACC: Cardiovascular Imaging*, vol. 1, no. 2, pp. 200–209, 2008.

[8] R. Drake, A. W. Vogl, and A. W. Mitchell, *Gray's anatomy for students E-book*. Elsevier Health Sciences, 2009.

[9] "Ascending aorta." `https://en.wikipedia.org/wiki/Ascending_aorta`. Accessed: 2022-01-15.

[10] M. J. Czarny and J. R. Resar, "Diagnosis and management of valvular aortic stenosis," *Clinical Medicine Insights: Cardiology*, vol. 8, pp. CMC–S15716, 2014.

[11] R. A. Nishimura, "Aortic valve disease," *Circulation*, vol. 106, no. 7, pp. 770–772, 2002.

[12] H. Baumgartner, J. Hung, J. Bermejo, J. B. Chambers, A. Evangelista, B. P. Griffin, B. Iung, C. M. Otto, P. A. Pellikka, and M. Quiñones, "Echocardiographic assessment of valve stenosis: EAE/ASE recommendations for clinical practice," *Journal of the American Society of Echocardiography*, vol. 22, no. 1, pp. 1–23, 2009.

[13] K. S. Cunningham and A. I. Gotlieb, "The role of shear stress in the pathogenesis of atherosclerosis," *Laboratory investigation*, vol. 85, no. 1, pp. 9–23, 2005.

[14] E. Saliba, Y. Sia, A. Dore, and I. El Hamamsy, "The ascending aortic aneurysm: When to intervene?," *IJC Heart & Vasculature*, vol. 6, pp. 91–100, 2015.

[15] J. K. Frogel, W. J. Vernick, J. T. Gutsche, and J. S. Savino, "Aortic valve anatomy and embryology," in *Perioperative Transesophageal Echocardiography*, pp. 125–143, Elsevier, 2014.

[16] C. Zhu, J.-H. Seo, and R. Mittal, "Computational modelling and analysis of haemodynamics in a simple model of aortic stenosis," *Journal of Fluid Mechanics*, vol. 851, pp. 23–49, 2018.

[17] L. S. Lilly, *Pathophysiology of heart disease: a collaborative project of medical students and faculty*, p. 74. Lippincott Williams & Wilkins, sixth ed., 2016.

[18] J. Cleve and M. L. McCulloch, "Conducting a cardiac ultrasound examination," in *Echocardiography*, pp. 33–42, Springer, 2018.

[19] E. Płońska-Gościniak, B. Lichodziejewska, A. Szyszka, T. Kukulski, J. D. Kasprzak, O. Dzikowska-Diduch, A. Gackowski, P. Gościniak, P. Pysz, and Z. Gąsior, "Echocardiography in adults," *Journal of Ultrasonography*, vol. 19, no. 76, p. 54, 2019.

[20] E. D. Agabegi and S. S. Agabegi, "Chap. 1: diseases of the cardiovascular system/section: valvular heart disease," *Step-Up to Medicine, Step-Up Series; Lippincott Williams & Wilkins: Philadelphia, PA, USA*, 2008.

[21] F. J. Rogers, "Aortic stenosis: new thoughts on a cardiac disease of older people," *Journal of Osteopathic Medicine*, vol. 113, no. 11, pp. 820–828, 2013.

[22] H.-J. Schäfers, *Current treatment of aortic regurgitation*. UNI-MED Science, 2013.

[23] C. Harris, B. Croce, and C. Cao, "Tissue and mechanical heart valves," *Annals of cardiothoracic surgery*, vol. 4, no. 4, p. 399, 2015.

[24] D. R. Johnston, E. G. Soltesz, N. Vakil, J. Rajeswaran, E. E. Roselli, J. F. Sabik III, N. G. Smedira, L. G. Svensson, B. W. Lytle, and E. H. Blackstone, "Long-term durability of bioprosthetic aortic valves: implications from 12,569 implants," *The Annals of thoracic surgery*, vol. 99, no. 4, pp. 1239–1247, 2015.

[25] R. A. Siemieniuk, T. Agoritsas, V. Manja, T. Devji, Y. Chang, M. M. Bala, L. Thabane, and G. H. Guyatt, "Transcatheter versus surgical aortic valve replacement in patients with severe aortic stenosis at low and intermediate risk: systematic review and meta-analysis," *bmj*, vol. 354, 2016.

[26] P. O. Vandvik, C. M. Otto, R. A. Siemieniuk, R. Bagur, G. H. Guyatt, L. Lytvyn, R. Whitlock, T. Vartdal, D. Brieger, B. Aertgeerts, *et al.*, "Transcatheter or surgical aortic valve replacement for patients with severe, symptomatic, aortic stenosis at low to intermediate surgical risk: a clinical practice guideline," *Bmj*, vol. 354, 2016.

[27] E. J. Dijkema, T. Leiner, and H. B. Grotenhuis, "Diagnosis, imaging and clinical management of aortic coarctation," *Heart*, vol. 103, no. 15, pp. 1148–1155, 2017.

[28] J. F. Bentzon, F. Otsuka, R. Virmani, and E. Falk, "Mechanisms of plaque formation and rupture," *Circulation research*, vol. 114, no. 12, pp. 1852–1866, 2014.

[29] C. Gopalan and E. Kirk, *Biology of Cardiovascular and Metabolic Diseases*. Academic Press, 2022.

[30] O. Reynolds, "IV. on the dynamical theory of incompressible viscous fluids and the determination of the criterion," *Philosophical transactions of the royal society of london.(a.)*, no. 186, pp. 123–164, 1895.

[31] W. M. DeCampli, I. R. Argueta-Morales, E. Divo, and A. J. Kassab, "Computational fluid dynamics in congenital heart disease," *Cardiology in the Young*, vol. 22, no. 6, pp. 800–808, 2012.

[32] S. Nordmeyer, F. Hellmeier, P. Yevtushenko, M. Kelm, C.-B. Lee, D. Lehmann, S. Kropf, F. Berger, V. Falk, C. Knosalla, *et al.*, "Abnormal aortic flow profiles persist after aortic valve replacement in the majority of patients with aortic valve disease: how model-based personalized therapy planning could improve results. a pilot study approach," *European Journal of Cardio-Thoracic Surgery*, vol. 57, no. 1, pp. 133–141, 2020.

[33] F. Hellmeier, S. Nordmeyer, P. Yevtushenko, J. Bruening, F. Berger, T. Kuehne, L. Goubergrits, and M. Kelm, "Hemodynamic evaluation of a biological and mechanical aortic valve prosthesis using patient-specific MRI-based CFD," *Artificial organs*, vol. 42, no. 1, pp. 49–57, 2018.

[34] M. Kelm, L. Goubergrits, J. Bruening, P. Yevtushenko, J. Fernandes, S. Sündermann, F. Berger, V. Falk, T. Kuehne, and S. Nordmeyer, "Model-based therapy planning allows prediction of haemodynamic outcome after aortic valve replacement," *Scientific Reports*, vol. 7, no. 1, pp. 1–12, 2017.

[35] Y. Hohri, K. Itatani, S. Yamazaki, and H. Yaku, "Computerized virtual surgery based on computational fluid dynamics simulation for planning coronary revascularization with aortic root replacement in adult congenital heart disease: a case report," *General Thoracic and Cardiovascular Surgery*, vol. 69, no. 4, pp. 722–726, 2021.

[36] P. D. Morris, A. Narracott, H. von Tengg-Kobligk, D. A. S. Soto, S. Hsiao, A. Lungu, P. Evans, N. W. Bressloff, P. V. Lawford, D. R. Hose, *et al.*, "Computational fluid dynamics modelling in cardiovascular medicine," *Heart*, vol. 102, no. 1, pp. 18–28, 2016.

[37] R. Nerem, W. Seed, and N. Wood, "An experimental study of the velocity distribution and transition to turbulence in the aorta," *Journal of Fluid Mechanics*, vol. 52, no. 1, pp. 137–160, 1972.

[38] H. L. Falsetti, K. M. Kiser, G. P. Francis, and E. R. Belmore, "Sequential velocity development in the ascending and descending aorta of the dog," *Circulation Research*, vol. 31, no. 3, pp. 328–338, 1972.

[39] T. Yearwood, G. Misbach, and K. Chandran, "Experimental fluid dynamics of aortic stenosis in a model of the human aorta," *Clinical Physics and Physiological Measurement*, vol. 10, no. 1, p. 11, 1989.

[40] Y. Agrawal, L. Talbot, and K. Gong, "Laser anemometer study of flow development in curved circular pipes," *Journal of Fluid Mechanics*, vol. 85, no. 3, pp. 497–518, 1978.

[41] U. S. Choi, L. Talbot, and I. Cornet, "Experimental study of wall shear rates in the entry region of a curved tube," *Journal of Fluid Mechanics*, vol. 93, no. 3, pp. 465–489, 1979.

[42] K. Chandran and T. Yearwood, "Experimental study of physiological pulsatile flow in a curved tube," *Journal of fluid mechanics*, vol. 111, pp. 59–85, 1981.

[43] N. Saikrishnan, C.-H. Yap, N. C. Milligan, N. V. Vasilyev, and A. P. Yoganathan, "In vitro characterization of bicuspid aortic valve hemodynamics using particle image velocimetry," *Annals of biomedical engineering*, vol. 40, pp. 1760–1775, 2012.

[44] Z. Keshavarz-Motamed, J. Garcia, E. Gaillard, N. Maftoon, G. Di Labbio, G. Cloutier, and L. Kadem, "Effect of coarctation of the aorta and bicuspid aortic valve on flow dynamics and turbulence in the aorta using particle image velocimetry," *Experiments in fluids*, vol. 55, pp. 1–16, 2014.

[45] M. Barakat, D. Dvir, and A. N. Azadani, "Fluid dynamic characterization of transcatheter aortic valves using particle image velocimetry," *Artificial organs*, vol. 42, no. 11, pp. E357–E368, 2018.

[46] K. M. Tse, R. Chang, H. P. Lee, S. P. Lim, S. K. Venkatesh, and P. Ho, "A computational fluid dynamics study on geometrical influence of the aorta

on haemodynamics," *European Journal of Cardio-Thoracic Surgery*, vol. 43, no. 4, pp. 829–838, 2013.

[47] L. Morris, P. Delassus, A. Callanan, M. Walsh, F. Wallis, P. Grace, and T. McGloughlin, "3-D numerical simulation of blood flow through models of the human aorta," *Journal of biomechanical engineering*, vol. 127, no. 5, pp. 767–775, 2005.

[48] Y. Zhu, R. Chen, Y.-H. Juan, H. Li, J. Wang, Z. Yu, and H. Liu, "Clinical validation and assessment of aortic hemodynamics using computational fluid dynamics simulations from computed tomography angiography," *Biomedical engineering online*, vol. 17, no. 1, pp. 1–12, 2018.

[49] J. Casacuberta Puig, E. Soudah Prieto, P. J. Gámez Montero, G. A. Raush Alviach, R. Castilla López, and J. S. Pérez Ronda, *Hemodynamics in the Thoracic Aorta using OpenFOAM: 4D PCMRI versus CFD*. 2015.

[50] D. Gallo, U. Gülan, A. Di Stefano, R. Ponzini, B. Lüthi, M. Holzner, and U. Morbiducci, "Analysis of thoracic aorta hemodynamics using 3D particle tracking velocimetry and computational fluid dynamics," *Journal of biomechanics*, vol. 47, no. 12, pp. 3149–3155, 2014.

[51] S. Laín and A. D. Caballero, "Simulation of unsteady blood flow dynamics in the thoracic aorta [simulación transitoria de la dinámica del flujo sanguíneo en la aorta torácica]," tech. rep., 2017.

[52] M. S. Zakaria, F. Ismail, M. Tamagawa, A. F. A. Azi, S. Wiriadidjaya, A. A. Basri, and K. A. Ahmad, "Computational fluid dynamics study of blood flow in aorta using OpenFOAM," *Journal of Advanced Research in Fluid Mechanics and Thermal Sciences*, vol. 43, no. 1, pp. 81–89, 2018.

[53] D. Kumar, R. Vinoth, R. Adhikari, and V. Shankar, "Non-newtonian and newtonian blood flow in human aorta: A transient analysis.," *Biomedical Research (0970-938X)*, vol. 28, no. 7, 2017.

[54] S. Karimi, M. Dabagh, P. Vasava, M. Dadvar, B. Dabir, and P. Jalali, "Effect of rheological models on the hemodynamics within human aorta: CFD study

on CT image-based geometry," *Journal of Non-Newtonian Fluid Mechanics*, vol. 207, pp. 42–52, 2014.

[55] D. Elad and S. Einav, "Physical and flow properties of blood," *Standard handbook of biomedical engineering and design*, pp. 3–1, 2003.

[56] E. L. Manchester, S. Pirola, M. Y. Salmasi, D. P. O'Regan, T. Athanasiou, and X. Y. Xu, "Analysis of turbulence effects in a patient-specific aorta with aortic valve stenosis," *Cardiovascular engineering and technology*, vol. 12, no. 4, pp. 438–453, 2021.

[57] P. Youssefi, A. Gomez, T. He, L. Anderson, N. Bunce, R. Sharma, C. A. Figueroa, and M. Jahangiri, "Patient-specific computational fluid dynamics—assessment of aortic hemodynamics in a spectrum of aortic valve pathologies," *The Journal of thoracic and cardiovascular surgery*, vol. 153, no. 1, pp. 8–20, 2017.

[58] M. Dabagh, P. Vasava, and P. Jalali, "Effects of severity and location of stenosis on the hemodynamics in human aorta and its branches," *Medical & biological engineering & computing*, vol. 53, no. 5, pp. 463–476, 2015.

[59] F. von Knobelsdorff-Brenkenhoff, R. F. Trauzeddel, A. J. Barker, H. Gruettner, M. Markl, and J. Schulz-Menger, "Blood flow characteristics in the ascending aorta after aortic valve replacement—a pilot study using 4D-flow MRI," *International journal of cardiology*, vol. 170, no. 3, pp. 426–433, 2014.

[60] J. Hu, J. Liu, Q. Jiang, Y. Zhu, W. Zhang, W. Dong, and H. Zhang, "Influence of surgical methods on hemodynamics in supravalvular aortic stenosis: A computational hemodynamic analysis," *Pediatric Cardiology*, vol. 42, no. 8, pp. 1730–1739, 2021.

[61] C.-S. Jhun, R. Newswanger, J. P. Cysyk, S. Ponnaluri, B. Good, K. B. Manning, and G. Rosenberg, "Dynamics of blood flows in aortic stenosis: mild, moderate, and severe," *ASAIO Journal*, vol. 67, no. 6, pp. 666–674, 2021.

[62] S. Bailoor, J.-H. Seo, S. Schena, and R. Mittal, "Detecting aortic valve anomaly from induced murmurs: Insights from computational hemodynamic models," *Frontiers in physiology*, p. 1696, 2021.

[63] L. Goubergrits, E. Riesenkampff, P. Yevtushenko, J. Schaller, U. Kertzscher, F. Berger, and T. Kuehne, "Is MRI-based CFD able to improve clinical treatment of coarctations of aorta?," *Annals of biomedical engineering*, vol. 43, no. 1, pp. 168–176, 2015.

[64] B. Melka, W. Adamczyk, M. Rojczyk, A. J. Nowak, A. Golda, and Z. Ostrowski, "Virtual therapy simulation for patient with coarctation of aorta using CFD blood flow modelling," in *Innovations in Biomedical Engineering*, pp. 153–160, Springer, 2017.

[65] R. Sadeghi, S. Khodaei, J. Ganame, and Z. Keshavarz-Motamed, "Towards non-invasive computational-mechanics and imaging-based diagnostic framework for personalized cardiology for coarctation," *Scientific Reports*, vol. 10, no. 1, pp. 1–19, 2020.

[66] Q. Lu, W. Lin, R. Zhang, R. Chen, X. Wei, T. Li, Z. Du, Z. Xie, Z. Yu, X. Xie, *et al.*, "Validation and diagnostic performance of a CFD-based non-invasive method for the diagnosis of aortic coarctation," *Frontiers in neuroinformatics*, p. 59, 2020.

[67] S. Aslan, P. Mass, Y.-H. Loke, L. Warburton, X. Liu, N. Hibino, L. Olivieri, and A. Krieger, "Non-invasive prediction of peak systolic pressure drop across coarctation of aorta using computational fluid dynamics," in *2020 42nd Annual International Conference of the IEEE Engineering in Medicine & Biology Society (EMBC)*, pp. 2295–2298, IEEE, 2020.

[68] J. Peacock, T. Jones, C. Tock, and R. Lutz, "The onset of turbulence in physiological pulsatile flow in a straight tube," *Experiments in fluids*, vol. 24, no. 1, pp. 1–9, 1998.

[69] A. F. Stalder, A. Frydrychowicz, M. F. Russe, J. G. Korvink, J. Hennig, K. Li, and M. Markl, "Assessment of flow instabilities in the healthy aorta using flow-sensitive MRI," *Journal of Magnetic Resonance Imaging*, vol. 33, no. 4, pp. 839–846, 2011.

[70] H. Kamada, H. Ota, M. Nakamura, Y. Imai, S. Ishida, W. Sun, K. Sakatsume, I. Yoshioka, Y. Saiki, and K. Takase, "Perioperative hemodynamic changes in

the thoracic aorta in patients with aortic valve stenosis: A prospective serial 4D-flow MRI study," in *Seminars in Thoracic and Cardiovascular Surgery*, vol. 32, pp. 25–34, Elsevier, 2020.

[71] N. Johari, N. Wood, Z. Cheng, R. Torii, M. Oishi, M. Oshima, and X. Xu, "Disturbed flow in a stenosed carotid artery bifurcation: Comparison of RANS-based transitional model and LES with experimental measurements," *International Journal of Applied Mechanics*, vol. 11, no. 04, p. 1950032, 2019.

[72] J. Lantz, T. Ebbers, J. Engvall, and M. Karlsson, "Numerical and experimental assessment of turbulent kinetic energy in an aortic coarctation," *Journal of biomechanics*, vol. 46, no. 11, pp. 1851–1858, 2013.

[73] J. Lantz, R. Gårdhagen, and M. Karlsson, "Quantifying turbulent wall shear stress in a subject specific human aorta using large eddy simulation," *Medical engineering & physics*, vol. 34, no. 8, pp. 1139–1148, 2012.

[74] L. Xu, T. Yang, L. Yin, Y. Kong, Y. Vassilevski, and F. Liang, "Numerical simulation of blood flow in aorta with dilation: a comparison between laminar and LES modeling methods," *Comput. Model. Eng. Sci.*, vol. 124, pp. 509–526, 2020.

[75] S. Miyazaki, K. Itatani, T. Furusawa, T. Nishino, M. Sugiyama, Y. Takehara, and S. Yasukochi, "Validation of numerical simulation methods in aortic arch using 4D flow MRI," *Heart and vessels*, vol. 32, no. 8, pp. 1032–1044, 2017.

[76] N. Shahcheraghi, H. Dwyer, A. Cheer, A. Barakat, and T. Rutaganira, "Unsteady and three-dimensional simulation of blood flow in the human aortic arch," *J. Biomech. Eng.*, vol. 124, no. 4, pp. 378–387, 2002.

[77] R. M. NEREM, J. A. RUMBERGER JR, D. R. GROSS, W. W. MUIR, and G. L. GEIGER, "Hot film coronary artery velocity measurements in horses," *Cardiovascular Research*, vol. 10, no. 3, pp. 301–313, 1976.

[78] W. Seed and N. Wood, "Velocity patterns in the aorta," *Cardiovascular research*, vol. 5, no. 3, pp. 319–330, 1971.

[79] U. Morbiducci, R. Ponzini, D. Gallo, C. Bignardi, and G. Rizzo, "Inflow boundary conditions for image-based computational hemodynamics: impact

of idealized versus measured velocity profiles in the human aorta," *Journal of biomechanics*, vol. 46, no. 1, pp. 102–109, 2013.

[80] L. Goubergrits, R. Mevert, P. Yevtushenko, J. Schaller, U. Kertzscher, S. Meier, S. Schubert, E. Riesenkampff, and T. Kuehne, "The impact of MRI-based inflow for the hemodynamic evaluation of aortic coarctation," *Annals of biomedical engineering*, vol. 41, no. 12, pp. 2575–2587, 2013.

[81] S. Pirola, O. Jarral, D. O'Regan, G. Asimakopoulos, J. Anderson, J. Pepper, T. Athanasiou, and X. Xu, "Computational study of aortic hemodynamics for patients with an abnormal aortic valve: The importance of secondary flow at the ascending aorta inlet," *APL bioengineering*, vol. 2, no. 2, p. 026101, 2018.

[82] P. Youssefi, A. Gomez, C. Arthurs, R. Sharma, M. Jahangiri, and C. Alberto Figueroa, "Impact of patient-specific inflow velocity profile on hemodynamics of the thoracic aorta," *Journal of biomechanical engineering*, vol. 140, no. 1, 2018.

[83] N. Westerhof, J.-W. Lankhaar, and B. E. Westerhof, "The arterial windkessel," *Medical & biological engineering & computing*, vol. 47, no. 2, pp. 131–141, 2009.

[84] A. G. Brown, Y. Shi, A. Marzo, C. Staicu, I. Valverde, P. Beerbaum, P. V. Lawford, and D. R. Hose, "Accuracy vs. computational time: translating aortic simulations to the clinic," *Journal of biomechanics*, vol. 45, no. 3, pp. 516–523, 2012.

[85] M. Simão, J. M. Ferreira, A. C. Tomás, J. Fragata, and H. M. Ramos, "Aorta ascending aneurysm analysis using CFD models towards possible anomalies," *Fluids*, vol. 2, no. 2, p. 31, 2017.

[86] I. E. Vignon and C. A. Taylor, "Outflow boundary conditions for one-dimensional finite element modeling of blood flow and pressure waves in arteries," *Wave Motion*, vol. 39, no. 4, pp. 361–374, 2004.

[87] I. E. Vignon-Clementel, C. A. Figueroa, K. E. Jansen, and C. A. Taylor, "Outflow boundary conditions for three-dimensional finite element modeling of

blood flow and pressure in arteries," *Computer methods in applied mechanics and engineering*, vol. 195, no. 29-32, pp. 3776–3796, 2006.

[88] S. Pirola, Z. Cheng, O. Jarral, D. O'Regan, J. Pepper, T. Athanasiou, and X. Xu, "On the choice of outlet boundary conditions for patient-specific analysis of aortic flow using computational fluid dynamics," *Journal of biomechanics*, vol. 60, pp. 15–21, 2017.

[89] M. Hoeijmakers, W. Huberts, M. Rutten, and F. van de Vosse, "The impact of shape uncertainty on aortic-valve pressure-drop computations," *International Journal for Numerical Methods in Biomedical Engineering*, vol. 37, no. 10, p. e3518, 2021.

[90] S. J. Lighthill, *Mathematical biofluiddynamics*. SIAM, 1975.

[91] M. Singh, P. Sinha, and M. Aggarwal, "Flow in the entrance of the aorta," *Journal of Fluid Mechanics*, vol. 87, no. 1, pp. 97–120, 1978.

[92] R. Rieu, A. Friggi, and R. Pelissier, "Velocity distribution along an elastic model of human arterial tree," *Journal of biomechanics*, vol. 18, no. 9, pp. 703–715, 1985.

[93] S. Jin, J. Oshinski, and D. P. Giddens, "Effects of wall motion and compliance on flow patterns in the ascending aorta," *J. Biomech. Eng.*, vol. 125, no. 3, pp. 347–354, 2003.

[94] J. Lantz, J. Renner, and M. Karlsson, "Wall shear stress in a subject specific human aorta—influence of fluid-structure interaction," *International Journal of Applied Mechanics*, vol. 3, no. 04, pp. 759–778, 2011.

[95] O. Plunde and M. Bäck, "Arterial stiffness in aortic stenosis and the impact of aortic valve replacement," *Vascular Health and Risk Management*, vol. 18, p. 117, 2022.

[96] J. C. Kohn, M. C. Lampi, and C. A. Reinhart-King, "Age-related vascular stiffening: causes and consequences," *Frontiers in genetics*, vol. 6, p. 112, 2015.

[97] J. Renner, *Towards Subject Specific Aortic Wall Shear Stress: A Combined*

CFD and MRI Approach. PhD thesis, Linköping University Electronic Press, 2011.

[98] A. Miller, R. Lees, J. Kistler, and W. Abbott, "Spectral analysis of arterial bruits (phonoangiography): experimental validation.," *Circulation*, vol. 61, no. 3, pp. 515–520, 1980.

[99] C. Zhu, J.-H. Seo, and R. Mittal, "Computational modeling and analysis of murmurs generated by modeled aortic stenoses," *Journal of Biomechanical Engineering*, vol. 141, no. 4, 2019.

[100] R. S. Lees and C. F. Dewey, "Phonoangiography: a new noninvasive diagnostic method for studying arterial disease," *Proceedings of the National Academy of Sciences*, vol. 67, no. 2, pp. 935–942, 1970.

[101] J. Kistler, R. Lees, J. Friedman, M. Pressin, J. Mohr, G. Roberson, and R. Ojemann, "The bruit of carotid stenosis versus radiated basal heart murmurs. differentiation by phonoangiography.," *Circulation*, vol. 57, no. 5, pp. 975–981, 1978.

[102] S. A. Jones and A. Fronek, "Analysis of break frequencies downstream of a constriction in a cylindrical tube," *Journal of biomechanics*, vol. 20, no. 3, pp. 319–327, 1987.

[103] A. Borisyuk, "Modeling of noise generation by a vascular stenosis," *International Journal of Fluid Mechanics Research*, vol. 29, no. 1, 2002.

[104] A. Borisyuk, "Experimental study of wall pressure fluctuations in a pipe behind a cylindrical insertion with eccentricity," *International Journal of Fluid Mechanics Research*, vol. 31, no. 2, 2004.

[105] A. Borisyuk, "Study of the flow and acoustic fields in a rigid-walled channel of circular cross-section with a local axisymmetric narrowing: A theory," *International Journal of Fluid Mechanics Research*, vol. 34, no. 2, 2007.

[106] Y. Yazicioglu, T. J. Royston, T. Spohnholtz, B. Martin, F. Loth, and H. S. Bassiouny, "Acoustic radiation from a fluid-filled, subsurface vascular tube with internal turbulent flow due to a constriction," *The Journal of the Acoustical Society of America*, vol. 118, no. 2, pp. 1193–1209, 2005.

[107] J. H. Seo and R. Mittal, "A coupled flow-acoustic computational study of bruits from a modeled stenosed artery," *Medical & biological engineering & computing*, vol. 50, no. 10, pp. 1025–1035, 2012.

[108] K. Ozden, C. Sert, and Y. Yazicioglu, "Numerical investigation of wall pressure fluctuations downstream of concentric and eccentric blunt stenosis models," *Proceedings of the Institution of Mechanical Engineers, Part H: Journal of Engineering in Medicine*, vol. 234, no. 1, pp. 48–60, 2020.

[109] K. Ozden, C. Sert, and Y. Yazicioglu, "Effect of stenosis shape on the sound emitted from a constricted blood vessel," *Medical & biological engineering & computing*, vol. 58, pp. 643–658, 2020.

[110] K. Ozden, Y. Yazicioglu, and C. Sert, "Simulation of turbulence induced sound generation inside stenosed femoral artery models with different severities and eccentricities," *Computer Methods and Programs in Biomedicine*, vol. 208, p. 106253, 2021.

[111] A. N. Makaryus, J. N. Makaryus, A. Figgatt, D. Mulholland, H. Kushner, J. L. Semmlow, J. Mieres, and A. J. Taylor, "Utility of an advanced digital electronic stethoscope in the diagnosis of coronary artery disease compared with coronary computed tomographic angiography," *The American Journal of Cardiology*, vol. 111, no. 6, pp. 786–792, 2013.

[112] F. Azimpour, E. Caldwell, P. Tawfik, S. Duval, and R. F. Wilson, "Audible coronary artery stenosis," *The American journal of medicine*, vol. 129, no. 5, pp. 515–521, 2016.

[113] S. Winther, S. E. Schmidt, N. R. Holm, E. Toft, J. J. Struijk, H. E. Bøtker, and M. Bøttcher, "Diagnosing coronary artery disease by sound analysis from coronary stenosis induced turbulent blood flow: diagnostic performance in patients with stable angina pectoris," *The international journal of cardiovascular imaging*, vol. 32, no. 2, pp. 235–245, 2016.

[114] E. J. Benjamin, S. S. Virani, C. W. Callaway, A. M. Chamberlain, A. R. Chang, S. Cheng, S. E. Chiuve, M. Cushman, F. N. Delling, R. Deo, *et al.*, "Heart

disease and stroke statistics—2018 update: a report from the american heart association," *Circulation*, vol. 137, no. 12, pp. e67–e492, 2018.

[115] A. Hager, H. Kaemmerer, U. Rapp-Bernhardt, S. Blücher, K. Rapp, T. M. Bernhardt, M. Galanski, and J. Hess, "Diameters of the thoracic aorta throughout life as measured with helical computed tomography," *The Journal of thoracic and cardiovascular surgery*, vol. 123, no. 6, pp. 1060–1066, 2002.

[116] Y. I. Cho and K. R. Kensey, "Effects of the non-newtonian viscosity of blood on flows in a diseased arterial vessel. part 1: Steady flows," *Biorheology*, vol. 28, no. 3-4, pp. 241–262, 1991.

[117] W. Siauw, E. Ng, and J. Mazumdar, "Unsteady stenosis flow prediction: a comparative study of non-newtonian models with operator splitting scheme," *Medical engineering & physics*, vol. 22, no. 4, pp. 265–277, 2000.

[118] S. S. Shibeshi and W. E. Collins, "The rheology of blood flow in a branched arterial system," *Applied Rheology*, vol. 15, no. 6, pp. 398–405, 2005.

[119] A. Razavi, E. Shirani, and M. Sadeghi, "Numerical simulation of blood pulsatile flow in a stenosed carotid artery using different rheological models," *Journal of biomechanics*, vol. 44, no. 11, pp. 2021–2030, 2011.

[120] J. Boyd, J. M. Buick, and S. Green, "Analysis of the casson and carreau-yasuda non-newtonian blood models in steady and oscillatory flows using the lattice boltzmann method," *Physics of Fluids*, vol. 19, no. 9, p. 093103, 2007.

[121] U. Morbiducci, D. Gallo, D. Massai, R. Ponzini, M. A. Deriu, L. Antiga, A. Redaelli, and F. M. Montevecchi, "On the importance of blood rheology for bulk flow in hemodynamic models of the carotid bifurcation," *Journal of biomechanics*, vol. 44, no. 13, pp. 2427–2438, 2011.

[122] A. Popel and G. Enden, "An analytical solution for steady flow of a quemada fluid in a circular tube," *Rheologica acta*, vol. 32, pp. 422–426, 1993.

[123] R. K. Banerjee, Y. I. Cho, and K. Kensey, "Effect of the non-newtonian viscosity of blood on steady and pulsatile flow in stenosed arteries," *Adv Bioeng*, vol. 20, pp. 103–106, 1991.

[124] J. Smagorinsky, "General circulation experiments with the primitive equations: I. the basic experiment," *Monthly weather review*, vol. 91, no. 3, pp. 99–164, 1963.

[125] Y. Zhiyin, "Large-eddy simulation: Past, present and the future," *Chinese journal of Aeronautics*, vol. 28, no. 1, pp. 11–24, 2015.

[126] A. Leonard, "Energy cascade in large-eddy simulations of turbulent fluid flows," in *Advances in geophysics*, vol. 18, pp. 237–248, Elsevier, 1975.

[127] I. Celik, M. Klein, and J. Janicka, "Assessment measures for engineering LES applications," *Journal of fluids engineering*, vol. 131, no. 3, 2009.

[128] C.-H. Moeng and P. P. Sullivan, "Large-eddy simulation," *Encyclopedia of Atmospheric Sciences*, vol. 2, pp. 232–240, 2015.

[129] J. Boussinesq, *Essai sur la théorie des eaux courantes*. Imprimerie nationale, 1877.

[130] F. G. Schmitt, "About boussinesq's turbulent viscosity hypothesis: historical remarks and a direct evaluation of its validity," *Comptes Rendus Mécanique*, vol. 335, no. 9-10, pp. 617–627, 2007.

[131] M. Germano, U. Piomelli, P. Moin, and W. H. Cabot, "A dynamic subgrid-scale eddy viscosity model," *Physics of Fluids A: Fluid Dynamics*, vol. 3, no. 7, pp. 1760–1765, 1991.

[132] T. Kajishima and T. Nomachi, "One-equation subgrid scale model using dynamic procedure for the energy production," *Journal of Applied Mechanics*, vol. 73, no. 3, 2006.

[133] I. Veloudis, Z. Yang, and J. McGuirk, "LES of wall-bounded flows using a new subgrid scale model based on energy spectrum dissipation," *Journal of Applied Mechanics*, vol. 75, no. 2, 2008.

[134] B. Chaouat and R. Schiestel, "A new partially integrated transport model for subgrid-scale stresses and dissipation rate for turbulent developing flows," *Physics of Fluids*, vol. 17, no. 6, p. 065106, 2005.

[135] F. Nicoud and F. Ducros, "Subgrid-scale stress modelling based on the square of the velocity gradient tensor," *Flow, turbulence and Combustion*, vol. 62, no. 3, pp. 183–200, 1999.

[136] N. Tobin, B. C. Good, J. D. Plasencia, M. A. Fogel, W. J. Weiss, and K. B. Manning, "Computational investigation of anastomosis options of a right-heart pump to patient specific pulmonary arteries," *Annals of Biomedical Engineering*, vol. 50, no. 8, pp. 929–940, 2022.

[137] E. L. Manchester, S. Pirola, M. Y. Salmasi, D. P. O'Regan, T. Athanasiou, and X. Y. Xu, "Evaluation of computational methodologies for accurate prediction of wall shear stress and turbulence parameters in a patient-specific aorta," *Frontiers in Bioengineering and Biotechnology*, vol. 10, 2022.

[138] T. Yamamoto, T. Ichihashi, S. Ishida, E. Nomura, M. I. Kori, and K. Osman, "Pulsatile flow interaction between aorta and pulmonary artery,"

[139] T. Mukha and M. Liefvendahl, "Large-eddy simulation of turbulent channel flow," tech. rep., Technical Report, 2015.

[140] S. S. Varghese, S. H. Frankel, and P. F. Fischer, "Direct numerical simulation of stenotic flows. part 2. pulsatile flow," *Journal of Fluid Mechanics*, vol. 582, pp. 281–318, 2007.

[141] B. B. Lieber and D. P. Giddens, "Apparent stresses in disturbed pulsatile flows," *Journal of biomechanics*, vol. 21, no. 4, pp. 287–298, 1988.

[142] R. Mittal, H. Dong, M. Bozkurttas, F. Najjar, A. Vargas, and A. Von Loebbecke, "A versatile sharp interface immersed boundary method for incompressible flows with complex boundaries," *Journal of computational physics*, vol. 227, no. 10, pp. 4825–4852, 2008.

[143] V. Paruchuri, K. F. Salhab, G. Kuzmik, G. Gubernikoff, H. Fang, J. A. Rizzo, B. A. Ziganshin, and J. A. Elefteriades, "Aortic size distribution in the general population: explaining the size paradox in aortic dissection," *Cardiology*, vol. 131, no. 4, pp. 265–272, 2015.

[144] I. Celik, Z. Cehreli, and I. Yavuz, "Index of resolution quality for large eddy simulations," 2005.

[145] G. W. Duncan, J. O. Gruber, C. F. Dewey Jr, G. S. Myers, and R. S. Lees, "Evaluation of carotid stenosis by phonoangiography," *New England Journal of Medicine*, vol. 293, no. 22, pp. 1124–1128, 1975.

[146] R. Mittal, S. Simmons, and F. Najjar, "Numerical study of pulsatile flow in a constricted channel," *Journal of Fluid Mechanics*, vol. 485, pp. 337–378, 2003.

[147] S. J. Sherwin and H. M. Blackburn, "Three-dimensional instabilities and transition of steady and pulsatile axisymmetric stenotic flows," *Journal of Fluid Mechanics*, vol. 533, pp. 297–327, 2005.

[148] M. Paul and M. M. Molla, "Investigation of physiological pulsatile flow in a model arterial stenosis using large-eddy and direct numerical simulations," *Applied Mathematical Modelling*, vol. 36, no. 9, pp. 4393–4413, 2012.

[149] R. J. Tobin and I.-D. Chang, "Wall pressure spectra scaling downstream of stenoses in steady tube flow," *Journal of Biomechanics*, vol. 9, no. 10, pp. 633–640, 1976.

[150] P. Lu, D. Gross, and N. Hwang, "Intravascular pressure and velocity fluctuations in pulmonic arterial stenosis," *Journal of Biomechanics*, vol. 13, no. 3, pp. 291–300, 1980.

APPENDIX A

OPENFOAM FILES

A.1 Boundary Conditions

A.1.1 "epsilon" File

```
/*--------------------------*- C++ -*----------------------------*\
  =========                 |
  \\      /  F ield         | OpenFOAM: Open Source CFD Toolbox
   \\    /   O peration     | Website:  https://openfoam.org
    \\  /    A nd           | Version:  8
     \\/     M anipulation  |
\*---------------------------------------------------------------*/
FoamFile
{
    version     2.0;
    format      ascii;
    class       volScalarField;
    location    "0";
    object      epsilon;
}

dimensions      [0 2 -3 0 0 0 0];

internalField   uniform 1e-3;

boundaryField
{
    INLET
    {
        type            fixedValue;
        value           uniform 1e-3;
    }
    OUTLET
    {
        type            zeroGradient;
    }
    WALLS
```

```
    {
        type            epsilonWallFunction;
        value           uniform 1e-3;
    }
}
```

A.1.2 "k" File

```
/*--------------------------*- C++ -*----------------------------*\
  =========                 |
  \\      /  F ield         | OpenFOAM: Open Source CFD Toolbox
   \\    /   O peration     | Website:  https://openfoam.org
    \\  /    A nd           | Version:  8
     \\/     M anipulation  |
\*---------------------------------------------------------------*/
FoamFile
{
    version     2.0;
    format      ascii;
    class       volScalarField;
    object      k;
}

dimensions      [0 2 -2 0 0 0 0];

internalField   uniform 1.597e-4;

boundaryField
{
    INLET
    {
        type            fixedValue;
        value           uniform 1.597e-4;
    }

    OUTLET
    {
        type            zeroGradient;
    }

   WALLS
    {
        type            kqRWallFunction;
        value           uniform 0;
    }
}
```

A.1.3 "nut" File

```
/*--------------------------*- C++ -*----------------------------*\
  =========                 |
  \\      /  F ield         | OpenFOAM: Open Source CFD Toolbox
   \\    /   O peration     | Website:  https://openfoam.org
    \\  /    A nd           | Version:  8
     \\/     M anipulation  |
\*-------------------------------------------------------------*/
FoamFile
{
    version     2.0;
    format      ascii;
    class       volScalarField;
    object      nut;
}

dimensions      [0 2 -1 0 0 0 0];

internalField   uniform 0;

boundaryField
{
    INLET
    {
        type            calculated;
        value                 uniform 0;
    }

    OUTLET
    {
        type            calculated;
        value                 uniform 0;
    }

   WALLS
    {
        type            nutkWallFunction;
        value                uniform 0;
    }
}
```

A.1.4 "nuTilda" File

```
/*--------------------------*- C++ -*----------------------------*\
  =========                 |
  \\      /  F ield         | OpenFOAM: Open Source CFD Toolbox
```

```
    \\    /   O peration     | Website:  https://openfoam.org
     \\  /    A nd           | Version:  8
      \\/     M anipulation  |
\*---------------------------------------------------------------------------*/
FoamFile
{
    version     2.0;
    format      ascii;
    class       volScalarField;
    object      nuTilda;
}

dimensions      [0 2 -1 0 0 0 0];

internalField   uniform 0;

boundaryField
{
    INLET
    {
        type            fixedValue;
        value           uniform 0;
    }

    OUTLET
    {
        type                zeroGradient;
        // type            inletOutlet;
        // inletValue      uniform 0;
        // value           uniform 0;
    }

    WALLS
    {
        type            fixedValue;
        value           uniform 0;
    }
}
```

A.1.5 "p" File

```
/*--------------------------*- C++ -*----------------------------*\
  =========                 |
  \\      /  F ield         | OpenFOAM: Open Source CFD Toolbox
   \\    /   O peration     | Website:  https://openfoam.org
    \\  /    A nd           | Version:  8
     \\/     M anipulation  |
\*---------------------------------------------------------------------------*/
```

```
FoamFile
{
    version     2.0;
    format      ascii;
    class       volScalarField;
    object      p;
}

dimensions      [0 2 -2 0 0 0 0];

internalField   uniform 0;

boundaryField
{
    INLET
    {
        type            zeroGradient;
    }

    OUTLET
    {
        type            fixedValue;
        value           uniform 0;
    }

    WALLS
    {
        type            zeroGradient;
    }
}
```

A.1.6 "U" File

```
/*--------------------------*- C++ -*----------------------------*\
  =========                 |
  \\      /  F ield         | OpenFOAM: Open Source CFD Toolbox
   \\    /   O peration     | Website:  https://openfoam.org
    \\  /    A nd           | Version:  8
     \\/     M anipulation  |
\*---------------------------------------------------------------*/
FoamFile
{
    version     2.0;
    format      ascii;
    class       volVectorField;
    object      U;
}

```

```
dimensions      [0 1 -1 0 0 0 0];

internalField   uniform (0 0 0);

boundaryField
{

    INLET
    {
        type            timeVaryingMappedFixedValue;
        offset          (0 0 0);
        setAverage      off;
        perturb                 0;
    }

    OUTLET
    {
        type           zeroGradient;
    }

    WALLS
    {
        type            noSlip;
    }
}
```

A.2 Solution Parameters

A.2.1 "controlDict" File

```
/*--------------------------*- C++ -*----------------------------*\
  =========                 |
  \\      /  F ield         | OpenFOAM: Open Source CFD Toolbox
   \\    /   O peration     | Website:  https://openfoam.org
    \\  /    A nd           | Version:  8
     \\/     M anipulation  |
\*---------------------------------------------------------------*/
FoamFile
{
    version     2.0;
    format      ascii;
    class       dictionary;
    location    "system";
    object      controlDict;
}

application     pimpleFoam;
```

```
startFrom       latestTime;
startTime       0;
stopAt          endTime;
endTime         9;
deltaT          0.0000005;
writeControl    adjustableRunTime;
writeInterval   0.04;
purgeWrite      0;
writeFormat     ascii;
writePrecision  10;
writeCompression off;
timeFormat      general;
timePrecision   10;
runTimeModifiable true;
adjustTimeStep        yes;
maxCo                 1;

functions
{
        vorticity1
        {
            // Mandatory entries (unmodifiable)
            type        vorticity;
            libs        ("libfieldFunctionObjects.so");
            // Optional (inherited) entries
            // field           <inpField>;
            // result          <fieldResult>;
            // region          region0;
            enabled         true;
            log             true;
            // timeStart       0;
            // timeEnd         1000;
            executeControl  timeStep;
            executeInterval 1;
            writeControl    outputTime;
            // writeInterval   0.001;
        }

////////////////////////////////////////////////

        writeCellVolumes1
        {
            type                writeCellVolumes;
            libs                ("libfieldFunctionObjects.so");
            enabled                true;
            writeControl        outputTime;
            // writeInterval        0.001;
        }

```

```
67 ////////////////////////////////////////////////
68
69         turbulenceFields1
70         {
71             type                    turbulenceFields;
72             functionObjectLibs("libutilityFunctionObjects.so");
73             enabled                 true;
74             writeControl            outputTime;
75             // writeInterval           0.001;
76             executeControl  timeStep;
77             executeInterval 1;
78             fields
79             (
80                 k
81                 epsilon
82                 nuEff
83             );
84         }
85
86 ////////////////////////////////////////////////
87
88         wallShearStress1
89         {
90             // Mandatory entries (unmodifiable)
91             type            wallShearStress;
92             libs            ("libfieldFunctionObjects.so");
93             writePrecision  10;
94             writeToFile     true;
95             useUserTime     true;
96             region          region0;
97             enabled         true;
98             log             true;
99             // timeStart       0;
100            // timeEnd         1000;
101            executeControl  timeStep;
102            executeInterval 1;
103            writeControl    outputTime;
104            // writeInterval   0.001;
105        }
106
107
108 ////////////////////////////////////////////////
109
110        probes1
111        {
112            type                probes;
113            libs               ("libsampling.so");
114            enabled                true;
115            executeControl  timeStep;
```

```
116             executeInterval 1;
117             writeControl        runTime;
118             writeInterval        0.0005;
119             interpolationScheme cellPatchConstrained;
120             fields
121             (
122                     p
123                     U
124                     k
125             );
126             probeLocations
127 (
128 (         0         0         0.064         )
129 (         0         0.00097230381         0.07511348337         )
130 (         0         0.00218074712         0.08056441889         )
131 (         0         0.00385967227         0.08588928917         )
132 (         0         0.00599630163         0.09104756875         )
133 (         0         0.00857437416         0.09600000000         )
134 (         0         0.01157426917         0.10070889193         )
135 (         0         0.01497315564         0.10513840702         )
136 (         0         0.01874516600         0.10925483400         )
137 (         0         0.02286159298         0.11302684436         )
138 (         0         0.02729110807         0.11642573083         )
139 (         0         0.03200000000         0.11942562584         )
140 (         0         0.03695243125         0.12200369837         )
141 (         0         0.04211071083         0.12414032773         )
142 (         0         0.04744         0.12582         )
143 (         0         0.064         0.128         )
144 (         0         0.096         0.11942562584         )
145 (         0         0.11942562584         0.096         )
146 (         0         0.128         0.064         )
147 (         0.015999         0         0.064         )
148 (         0.015998         0.00097230381         0.07511348337
149 (         0.015998         0.00218074712         0.08056441889
150 (         0.015998         0.00385967227         0.08588928917
151 (         0.015998         0.00599630163         0.09104756875
152 (         0.015998         0.00857437416         0.09600000000
153 (         0.015998         0.01157426917         0.10070889193
154 (         0.015998         0.01497315564         0.10513840702
155 (         0.015998         0.01874516600         0.10925483400
156 (         0.015998         0.02286159298         0.11302684436
157 (         0.015998         0.02729110807         0.11642573083
158 (         0.015998         0.03200000000         0.11942562584
159 (         0.015998         0.03695243125         0.12200369837
160 (         0.015998         0.04211071083         0.12414032773
161 (         0.015999         0.04744         0.12582         )
162 (         0.015998         0.064         0.128         )
163 (         0.015998         0.096         0.11942562584         )
164 (         0.015998         0.11942562584         0.096         )
```

```
(         0.015998         0.128         0.064         )
(         0         0         0)

            );
        }

////////////////////////////////////////////////
}
```

A.2.2 "fvSchemes" File

```
/*--------------------------*- C++ -*----------------------------*\
  =========                 |
  \\      /  F ield         | OpenFOAM: Open Source CFD Toolbox
   \\    /   O peration     | Website:  https://openfoam.org
    \\  /    A nd           | Version:  8
     \\/     M anipulation  |
\*---------------------------------------------------------------*/
FoamFile
{
    version     2.0;
    format      ascii;
    class       dictionary;
    location    "system";
    object      fvSchemes;
}

ddtSchemes
{
    default         backward;
}

gradSchemes
{
    default         Gauss linear;
}

divSchemes
{
    default         none;
    div(phi,U)      Gauss linear;
    div(phi,k)      Gauss limitedLinear 1;
    div(phi,nuTilda)        Gauss limitedLinear 1;
    div((nuEff*dev2(T(grad(U))))) Gauss linear;
}

laplacianSchemes
{
```

```
    default         Gauss linear corrected;
}

interpolationSchemes
{
    default         linear;
}

snGradSchemes
{
    default         corrected;
}
```

A.2.3 "fvSolution" File

```
/*--------------------------*- C++ -*----------------------------*\
  =========                 |
  \\      /  F ield         | OpenFOAM: Open Source CFD Toolbox
   \\    /   O peration     | Website:  https://openfoam.org
    \\  /    A nd           | Version:  8
     \\/     M anipulation  |
\*-------------------------------------------------------------*/
FoamFile
{
    version     2.0;
    format      ascii;
    class       dictionary;
    location    "system";
    object      fvSolution;
}
solvers
{
    p
    {
        solver          GAMG;
        tolerance       1e-06;
        relTol          0.1;
        smoother        GaussSeidel;
    }

    pFinal
    {
        $p;
        smoother        DICGaussSeidel;
        tolerance       1e-06;
        relTol          0;
    }

```

```
    "(U|k|nuTilda)"
    {
        solver          smoothSolver;
        smoother        GaussSeidel;
        tolerance       1e-05;
        relTol          0.1;
    }

    "(U|k|nuTilda)Final"
    {
        $U;
        tolerance       1e-05;
        relTol          0;
    }

}

PIMPLE
{
    nOuterCorrectors               2;
    nCorrectors                    3;
    nNonOrthogonalCorrectors        1;
}
```

A.2.4 "momentumTransport" File

```
/*--------------------------*- C++ -*----------------------------*\
  =========                 |
  \\      /  F ield         | OpenFOAM: Open Source CFD Toolbox
   \\    /   O peration     | Website:  https://openfoam.org
    \\  /    A nd           | Version:  8
     \\/     M anipulation  |
\*---------------------------------------------------------------*/
FoamFile
{
    version     2.0;
    format      ascii;
    class       dictionary;
    location    "constant";
    object      momentumTransport;
}

simulationType LES;

LES
{
    model           WALE;

```

```
23      turbulence      on;
24
25      printCoeffs     on;
26
27      delta           cubeRootVol;
28
29      cubeRootVolCoeffs
30      {
31          deltaCoeff      1;
32      }
33
34      PrandtlCoeffs
35      {
36          delta           cubeRootVol;
37          cubeRootVolCoeffs
38          {
39              deltaCoeff      1;
40          }
41
42          smoothCoeffs
43          {
44              delta           cubeRootVol;
45              cubeRootVolCoeffs
46              {
47                  deltaCoeff      1;
48              }
49
50              maxDeltaRatio   1.1;
51          }
52
53          Cdelta          0.158;
54      }
55
56      vanDriestCoeffs
57      {
58          delta           cubeRootVol;
59          cubeRootVolCoeffs
60          {
61              deltaCoeff      1;
62          }
63
64          smoothCoeffs
65          {
66              delta           cubeRootVol;
67              cubeRootVolCoeffs
68              {
69                  deltaCoeff      1;
70              }
71
```

```
            maxDeltaRatio   1.1;
        }

        Aplus           26;
        Cdelta          0.158;
    }

    smoothCoeffs
    {
        delta           cubeRootVol;
        cubeRootVolCoeffs
        {
            deltaCoeff      1;
        }

        maxDeltaRatio   1.1;
    }
}
```

A.2.5 "transportProperties" File

```
/*--------------------------*- C++ -*----------------------------*\
  =========                 |
  \\      /  F ield         | OpenFOAM: Open Source CFD Toolbox
   \\    /   O peration     | Website:  https://openfoam.org
    \\  /    A nd           | Version:  8
     \\/     M anipulation  |
\*-------------------------------------------------------------*/
FoamFile
{
    version     2.0;
    format      ascii;
    class       dictionary;
    location    "constant";
    object      transportProperties;
}

transportModel BirdCarreau;

BirdCarreauCoeffs
{
    nu0     nu0 [ 0 2 -1 0 0 0 0 ] 5.283e-05;
    nuInf   nuInf [ 0 2 -1 0 0 0 0 ] 3.2e-06;
    k       k [ 0 0  1 0 0 0 0 ] 3.313005;
    n       n [ 0 0  0 0 0 0 0 ] 0.3568;
}
```

APPENDIX B

MATLAB CODES

B.1 Generating OpenFOAM Files for Inlet Velocity Boundary Condition

```
% This code generates the inlet boundary condition files
% to be used in OpenFOAM simulations.
% Parabolic velocity profile is used.

clear all;
close all;
clc;

% input parameters

D = 0.032;                  % Inlet diameter [m]
rho = 1050;                 % Density of working fluid [kg/m^3]
nu = 3.2e-6;                % Kinematic viscosity [m^2/s]
T = 0.75;                   % Period of the waveform [s]
Re_mean = 2000;             % Mean Reynolds number
nCycles = 12;               % the number of cycles
boundaryName = "INLET";     % the name of the boundary patch

% take waveform input
f = dlmread('dabagh.txt');
t_input = f(:,1);     % time vector of the input file
Q_input = f(:,2);     % flowrates of the input file

% resample data at 100 Hz
desiredFs = 100;
[U, t] = resample(Q_input,t_input,desiredFs);
U(1) = 0;
U(end) = 0;

% modify the profile to have desired Reynolds number
U = 0.375*U;
U = U + 0.108;
Re = U*D/nu;
fprintf("The average Reynolds number is %i \n\n", mean(Re));
fprintf("The maximum Reynolds number is %i \n\n", max(Re));
```

```
fprintf("Mean velocity of the cycle is %3.2f \n\n", mean(U));

figure
plot(t,U, "linewidth", 1.5)
xlabel("$$ t $$", "interpreter", "latex")
ylabel("$$ V $$", "interpreter", "latex")
grid on

figure
plot(t/T,U/mean(U), "linewidth", 5)
xlabel("$$ t/T $$", "interpreter", "latex")
ylabel("$$ V/V_{mean} $$", "interpreter", "latex")
grid on

% map the velocity values into polynomial profile
U_all = zeros(101,length(t));   % velocities (col:time row:location)
R = D/2;                        % radius of the inlet [m]

figure
for j = 1:length(t)
    x = linspace(-D/2,D/2,101);
    for i = 1:101
        U_all(i,j) = (-(3/2)*U(j)/(R^2))*x(i)^2 + 3*U(j)/2;
    end
    plot(U_all(:,j),x)
    hold on
end
title("parabolic velocity profiles at all time steps")

% generate 3D velocity profile from 2D
u_2D = U_all(51:101,:);

mkdir(boundaryName)     % make directory
cd(boundaryName)        % change directory

nSpatial = size(u_2D,1);
% nSpatial is the number of rows in u_2D, which is the
% spatial step size. In other words, the radius is
% divided into segments and expressed with size(u_2D,1) points.

nTime = size(u_2D,2); % number of time steps in 1 period

% time instants corresponding to the velocities
time = linspace(0,T,nTime);

radius = linspace(R,0,nSpatial); % radius vector
% delete the last element of 'radius', which is r = 0, so
% that the same point is not written more than once
radius(end) = [];
```

```
85
86  nPointsOnCircle = 100;   % number of points on each circle
87
88  theta = linspace(0,2*pi*(1-1/nPointsOnCircle),nPointsOnCircle);
89  % theta stores the angle every line makes with the z-axis
90
91  pointCoords = zeros((nSpatial-1)*nPointsOnCircle,2);
92  % stores the coordinates of all points on the patch surface
93
94  U = zeros(length(pointCoords),nTime);
95  % stores the velocity values of each point in pointCoords
96
97  % generate 3D velocity values by using the 2D velocity data,
98  % for each time step
99
100 column = 1;
101
102 for t = time
103
104     row = 0;
105     index = nSpatial;
106
107     for r = radius
108
109         y = r*sin(theta);
110         z = r*cos(theta);
111
112         for i = 1:nPointsOnCircle
113
114             row = row + 1;
115             pointCoords(row,1) = y(i);
116             pointCoords(row,2) = z(i);
117             U(row,column) = u_2D(index,column);
118
119         end
120
121         index = index - 1;
122
123     end
124
125     mkdir(num2str(t))   % create time step folder
126     cd(num2str(t))
127
128     % COMMENT or UNCOMMENT according to the flow direction
129     % formatSpec = '( \t %10.9f \t 0 \t 0 \t ) \n'; % x-dir
130     % formatSpec = '( \t 0 \t %10.9f \t 0 \t ) \n'; % y-dir
131     formatSpec = '( \t 0 \t 0 \t %10.9f \t ) \n'; z-dir
132
133     fileID = fopen( 'U', 'w');
```

```
134     fprintf(fileID, '// Data on points \n%.0f \n\n(\n\n', ...
135     length(pointCoords)+1);
136     fprintf(fileID,formatSpec,U(:,column));
137     % fprintf(fileID, '( \t %10.9f \t 0 \t 0 \t ) \n', ...
138     u_2D(1,column)); % x-dir
139     % fprintf(fileID, '( \t 0 \t %10.9f \t 0 \t ) \n', ...
140     u_2D(1,column)); % y-dir
141     fprintf(fileID, '( \t 0 \t 0 \t %10.9f \t ) \n', ...
142     u_2D(1,column)); % z-dir
143     fprintf(fileID, '\n)');
144     fclose(fileID);
145
146     column = column + 1;
147
148     cd ..
149
150 end
151
152 % write the 'points' file
153 pointsWrite = [];
154
155 for i = 1:length(pointCoords)
156
157     pointsWrite = [pointsWrite pointCoords(i,1)];
158     pointsWrite = [pointsWrite pointCoords(i,2)];
159
160 end
161
162 % COMMENT or UNCOMMENT according to the flow direction
163 % formatSpec = '( \t 0 \t %10.9f \t %10.9f \t ) \n'; % x-dir
164 % formatSpec = '( \t %10.9f \t 0 \t %10.9f \t ) \n'; % y-dir
165 formatSpec = '( \t %10.9f \t %10.9f \t 0 \t ) \n'; % z-dir
166
167 fileID = fopen( 'points', 'w');
168 fprintf(fileID, '// Points \n%.0f \n\n(\n\n', length(pointCoords)+1);
169 fprintf(fileID,formatSpec,pointsWrite);
170 fprintf(fileID, '( \t 0 \t 0 \t 0 \t ) \n'); % center point
171 fprintf(fileID, '\n)');
172 fclose(fileID);
173
174 % create time step folders for the whole simulation
175 for i = 1:nCycles-1
176
177     for t = time
178
179         copyfile( num2str(t), num2str(i*T+t , 7) );
180
181     end
182
```

```
end
cd ..
% end of the code.
```

B.2 Wall Pressure Fluctuations in Steady Flow

```
clc
clear all
close all

format longg

V_j = 0.8; % [m/s] jet velocity

% read the pPrime2Mean file
A = dlmread('anteriorProbes_pPrime2Mean.xy');

p_prime2mean = A(:,4);
p_rms = sqrt(p_prime2mean);
p_rms_nondim = p_rms / (V_j^2 * 0.5);

% plot data
theta = 0:180;
plot(theta, p_rms_nondim, 'linewidth', 1.5)
xlabel('$$ \theta $$', 'Interpreter','Latex')
ylabel('$$ P_{rms} / \left( \rho V_j^2 / 2 \right) $$', ...
'Interpreter','Latex')
```

B.3 Wall Pressure Fluctuations in Pulsatile Flow

```
clear all
close all
clc

format longg

V_mean = 0.2; % [m/s] mean inlet velocity
T = 0.75; % [s] period
totalCycles = 12;
discardedCycles = 2;
usedCycles = totalCycles - discardedCycles;

% there are 181 probes along the anterior surface.
% there is an additional probe at the outlet.
```

```
15
16 % Ensemble average is used to discard the effects of pulsating
17 % flow and focus on turbulence fluctuations. Therefore,
18 % double-prime figures show the turbulent fluctuations.
19
20 %% take input
21 p_probe = readmatrix('p', 'NumHeaderLines', 183, 'FileType', 'text');
22
23 % add an artificial cycle to the end (to discard the end
24 % effects of resampling)
25 p_probe = [p_probe ; p_probe(16496:end,:)];
26 p_probe(17997:end,1) = p_probe(17997:end,1) + 0.75;
27
28 % create time vector
29 t_probe = p_probe(:,1);
30
31 % resample data
32 desiredFs = 2000; % [Hz]
33 [P, t] = resample(p_probe,t_probe,desiredFs);
34
35 % discard the artifical cycle
36 P = P(1:T*desiredFs*totalCycles,:);
37 t = t(1:T*desiredFs*totalCycles,:);
38
39 % remove the first column of P since it is the time column
40 P(:,1) = [];
41
42 % ensemble average
43 % there are 181 probes along the anterior surface
44 p_total = zeros(T*desiredFs,181);
45 for i = discardedCycles+1:totalCycles
46     p_local = P((i-1)*T*desiredFs+1:i*T*desiredFs,1:181);
47     p_total = p_total + p_local;
48 end
49 P_ens = p_total/usedCycles;
50 t_ens = t(1:T*desiredFs);
51
52 % calculate double-prime (dp)
53 P_dp = zeros(T*desiredFs*usedCycles,181);
54 for i = discardedCycles+1:totalCycles
55     P_dp((i-1-discardedCycles)*T*desiredFs+1: ...
56     (i-discardedCycles)*T*desiredFs,:) = ...
57     P((i-1)*T*desiredFs+1:i*T*desiredFs,1:181) - P_ens;
58 end
59 t_dp = t(1:T*desiredFs*usedCycles);
60
61 % calculate rms
62 p_dp_total = zeros(size(P_ens));
63 for i = 1:usedCycles
```

```
    p_dp_local = P_dp((i-1)*T*desiredFs+1:i*T*desiredFs,:).^2;
    p_dp_total = p_dp_total + p_dp_local;
end
P_dp_squared_ens = p_dp_total/usedCycles;
P_dp_rms = sqrt(P_dp_squared_ens);

theta = [0:180];

% plot 3D graph (t - theta - p''_rms)
[X,Y] = meshgrid(theta,t_ens/T);
Z = P_dp_rms/(V_mean^2/2);
figure
surf(X,Y,Z, "EdgeColor", "none", "lineWidth", 0.001)
title("anterior surface")
xlabel("$$ \theta $$", "Interpreter", "latex")
ylabel("$$ t/T $$", "Interpreter", "latex")
zlabel("$$ p^{''}_{rms} / V_{mean}^2/2 $$", ...
"Interpreter", "latex")
xlim([0 180])
ylim([0 1])
```

B.4 Fast Fourier Transform for Spectral Analysis

```
clear all
close all
clc

V_j = 0.8; % [m/s]
D_j = 0.016; % [m]

format longg

p_probe = readmatrix('p', 'NumHeaderLines', 21, ...
'FileType', 'text');
t_irreg = p_probe(:,1);

% The process is only shown for theta = 0.
% Other theta values are similar.

p_theta0_centr = p_probe(:,18);
pMean_theta0_centr = mean(p_theta0_centr);
pPrime_theta0_centr = p_theta0_centr - pMean_theta0_centr;
pPrime_nondim_theta0_centr = pPrime_theta0_centr./(V_j^2/2);

% define signal (time domain)
s_0 = pPrime_nondim_theta0_centr;

```

```
% define FFT parameters
f_s = 2000;                 % sampling frequency
d = 0.5;                    % duration of the signal
N = f_s*d;                  % total number of samples
t = 0:d/N:d;                % time vector

% define frequency vector
f_left = f_s*(0:N/2-1)/N;

% define Strouhal number
St = f_left*(D_j/V_j);

% resample data at 2000 Hz
desiredFs = 2000;
[s_0_resampled, t_reg] = resample(s_0,t_irreg,desiredFs);

% discard initial transients (up to t = 2 s)
s_0_resampled = s_0_resampled(4001:13001);
t_reg_resampled = t_reg(4001:13001);

plot(t_irreg, s_0)
hold on
plot(t_reg_resampled, s_0_resampled)
legend("original", "resampled")

% divide the timeline into 17 sections of 0.5 seconds each
% section 1: t = 2 s to t = 2.5 s
% section 2: t = 2.25 s to t = 2.75 s
% section 3: t = 2.5 s to t = 3 s
% and so on ...
s_0_all = [];
for i = 1:17
    s_0_all = [s_0_all s_0_resampled( 500*(i-1)+1 : 500*(i+1) )];
end

% Hanning Window for removing discontinuities in the data
w=window(@hann,f_s*d);
w=w/(sum(w)/length(w));
% w=w';

% apply Hanning Window
for i = 1:17
    s_0_all(:,i) = s_0_all(:,i).*w;
end

% perform FFT
S_0_all = fft(s_0_all);

% use single sided spectrum
```

```
S_0_all_oneSide = [];
for i = 1:17
    S_0_all_oneSide(:,i) = S_0_all((1:N/2),i);
end

% change the scale of the y-axis
S_0_all_oneSide_sc = [];
for i = 1:17
    S_0_all_oneSide_sc(:,i) = abs(S_0_all_oneSide(:,i))/(N/2);
end

% take the average of the 17 time sections
S_0 = mean(S_0_all_oneSide_sc,2);

% linear fit to obtain break frequency
S_0_left = S_0(2:35);
S_0_right = S_0(20:100);

St_left = St(2:35);
St_right = St(20:100);

p_right = polyfit(log(St_right), log(S_0_right),1);
f_right = polyval(p_right,log(St_right));

p_left = polyfit(log(St_left), log(S_0_left),1);
f1_left = polyval(p_left,log(St_left));

% plot data
figure
loglog(St,S_0, '--', 'color', '#0072BD', 'linewidth', 1.25)
hold on
loglog(St_right, exp(f_right), 'color', 'k')
hold on
loglog(St_left, exp(f1_left), 'color', 'k')
xlabel('$St$','Interpreter','Latex');
ylabel('$E_p$','Interpreter','Latex');
axis([0.01 10 1e-8 1e-1])
grid on
```

B.5 Acoustic Pressure Figures

```
clc
clear all
close all

format longg

```

```
V_mean = 0.2; % [m/s] mean inlet velocity
T = 0.75; % [s] period
rho = 1060; % [kg/m^3] density

totalCycles = 12;
discardedCycles = 2;
usedCycles = totalCycles - discardedCycles;

% there are 181 probes along the anterior surface.
% there is an additional probe at the outlet.

%% take input
p_probe = readmatrix('p', 'NumHeaderLines', 183, ...
'FileType', 'text');

% add an artificial cycle to the end (to discard the
% end effects of resampling)
p_probe = [p_probe ; p_probe(16496:end,:)];
p_probe(17997:end,1) = p_probe(17997:end,1) + 0.75;

% create time vector
t_probe = p_probe(:,1);

% resample data
desiredFs = 2000; % [Hz]
[P, t] = resample(p_probe,t_probe,desiredFs);

% discard the artifical cycle
P = P(1:T*desiredFs*totalCycles,:);
t = t(1:T*desiredFs*totalCycles,:);

% check resampling to see if there is any problem
figure
plot(t_probe/T,p_probe(:,56))
hold on
plot(t/T,P(:,56))
legend("probe", "resampled")

% remove the first column of P since it is the time column
P(:,1) = [];
% remove the last column of P (it is the probe at the outlet)
P(:,end) = [];

% discard the initial cycles
P = P(discardedCycles*T*desiredFs+1:totalCycles*T*desiredFs,:);

% P values in OpenFOAM are actually p/rho, therefore multiply P
% with rho to get the actual P values
P = P*rho;
```

```
56
57  % divide P by P_ref to get acoustic pressure
58  P_ref = 2e-5; % [Pa]
59  P = P/P_ref;
60
61  % define FFT parameters
62  f_s = desiredFs;            % sampling frequency
63  d = 0.75;                   % duration of the signal
64  N = f_s*d;                  % total number of samples
65  t = 0:d/N:d;                % time vector
66
67  % define frequency vector
68  f_left = f_s*(0:N/2-1)/N;
69
70  % Hanning Window for removing discontinuities in the data
71  w = window(@hann,f_s*d);
72  w = w/(sum(w)/length(w));
73  % w = w';
74
75  % perform FFT for all probes
76  P_fft = [];
77
78  for probe = 1:181
79
80      % divide the cycles
81      s_all = [];
82      for i = 1:usedCycles
83          s_all = [s_all P( (i-1)*T*desiredFs+1 : ...
84          i*T*desiredFs , probe )];
85      end
86
87      % apply Hanning Window
88      for i = 1:usedCycles
89          s_all(:,i) = s_all(:,i).*w;
90      end
91
92      % perform FFT
93      S_all = fft(s_all);
94
95      % use single sided spectrum
96      S_all_oneSide = [];
97      for i = 1:usedCycles
98          S_all_oneSide(:,i) = S_all((1:N/2),i);
99      end
100
101     % change the scale of the y-axis
102     S_all_oneSide_sc = [];
103     for i = 1:usedCycles
104         S_all_oneSide_sc(:,i) = abs(S_all_oneSide(:,i))/(N/2);
```

```
105     end
106
107     % take the average of the used cycles
108     S = mean(S_all_oneSide_sc,2);
109
110     P_fft = [P_fft S];
111
112 end
113
114 % Convert the wall pressure amplitudes to logarithmic decibel
115 P_dB = 20*log10(P_fft);   % (P_fft is P/P_ref in freq. domain)
116
117 % define theta vector
118 theta = [0:180];
119
120 % plot frequency content of wall pressure fluctuations
121 % in logarithmic decibel scale
122 f = figure;
123 surf(f_left, theta, transpose(P_dB),'LineStyle','none');
124 shading interp;
125 % title("75% anterior surface")
126 % xlabel('Frequency (Hz)')
127 % ylabel('theta')
128 view([-270 -90]);
129 colormap jet;
130 caxis([90 140]);
131 set(gca,'FontSize',20)
132 a = colorbar;
133 % a.Label.String = 'Acoustic Pressure (dB)';
134 hColorbar.Label.Position(1) = 10;
135 xlim([0 300])
136 ylim([0 180])
137 f.Position = [100 0 1080 800];
```